Fakultät für Maschinenwesen

Lehrstuhl für Aerodynamik und Strömungsmechanik

Efficient Numerical Methods for Solving Multi-species Reactive Euler Equations

Jianhang Wang

Vollständiger Abdruck der von der Fakultät für Maschinenwesen der Technischen Universität München zur Erlangung des akademischen Grades eines

Doktor-Ingenieurs

genehmigten Dissertation.

Vorsitzender: Prof. Wolfgang Polifke, Ph.D.

Prüfer der Dissertation:

1. Priv.-Doz. Dr.-Ing. habil. Xiangyu Hu
2. Priv.-Doz. Dr. habil. Chaouki Habchi
3. Prof. Dr. Julija Zavadlav

Die Dissertation wurde am 08.11.2019 bei der Technischen Universität München eingereicht und durch die Fakultät für Maschinenwesen am 14.04.2020 angenommen.

Declaration of Authorship

I hereby declare that except where specific reference is made to the work of others, the contents of this dissertation are original and have not been submitted in whole or in part for consideration for any other degree or qualification in this, or any other university. This dissertation is my own work and contains nothing which is the outcome of work done in collaboration with others, except as specified in the text and Acknowledgements.

Jianhang Wang
June 12, 2020

jianhang.wang@tum.de

Released June 12, 2020
Typesetting LaTeX

纵横昆山片玉寒，繁华桂林一枝香

王建航於二〇〇七年

Abstract

This cumulative thesis is devoted to the efficient simulation of compressible chemically reactive flows with multiple species and reactions being involved. In addition, the mass-fraction based reactive Euler equations with multiple species can be used to describe two-phase flows with multiple 'components' (corresponding to 'species') in a diffuse-interface manner, with suitable equations of state or thermodynamical models being employed. Three numerical methods towards computational high-efficiency solution of the above equation system are proposed:

1. A new operator splitting method is proposed for capturing stiff and nonstiff detonation waves, balancing numerical accuracy and computational efficiency.

2. For the computationally expensive temporal integration of ordinary differential equation (ODE) system of chemical kinetics with detailed mechanisms, a species-clustered operator-splitting scheme is developed by using the idea of optimal partitioning.

3. The remaining flow convective terms are considered by using a partial characteristic decomposition scheme to overcome the numerical challenge of quadratically increasing dimensionality of the convective flux eigensystem as the number of species grows in the classical high-order finite difference (FD) framework.

To solve the multi-species Euler equations with chemical reaction source terms, lots of efforts have been placed upon using less grid points and larger timesteps to achieve higher efficiency with little loss of accuracy, which usually works well for non-reactive flow simulations. For chemically reactive flows, however, especially when the chemical kinetics is stiff compared with the fluid dynamics, under-resolution in both space and time would lead to the spurious propagating speed of reacting fronts. This well-known numerical phenomenon arises for classical shock-capturing schemes either in the FD or finite volume (FV) framework, and can be ascribed into the inevitable introduction of numerical dissipation or viscosity. In the first part of this thesis, we are trying to make correct use of the inherent numerical dissipation by (i) appealing to the idea of random activation or deactivation of reaction source terms in combination with (ii) operator splitting upon chemical reaction channels/pathways. As a result, we develop a split random time-stepping method for chemically reacting flows with general nonequilibrium chemistry in a unified manner, regardless of stiff or nonstiff

source terms and under- or well-resolved conditions in space and time. Extensive numerical experiments demonstrate the effectiveness and robustness of our method. For nonstiff problems, the proposed random method recovers the accuracy of general operator splitting methods by adding a drift term.

Considering the form of reactive Euler equations, operator splitting is usually used to decouple flow convection from the chemical reaction process, with each part being solved separately and step by step. The computational cost of solving the ODE system of chemical kinetics often exceeds a lot that of calculating the cell-face or half-point convective fluxes, and the former overwhelmingly dominates the overall CPU time in general situations. The CPU time for solving these ODEs will drastically grow as the number of species in the kinetic mechanism increases. In particular, when the popular implicit ODE solver such as the variable-coefficient ODE solver (VODE) is used, its CPU time scales with the number of species as $\mathcal{O}(N^2)$ to $\mathcal{O}(N^3)$ with extensive dense matrix operations. As the second part of work in this thesis, a species-clustered integrator based on operator splitting is thus proposed to improve the computational efficiency. The ODE system of large-scale chemical kinetics is split into clusters of species by using graph partition methods. Definition of the weight (similarity) matrix in graph partition methods is application-dependent and follows from chemical kinetics. Each species cluster is integrated by VODE. The theoretically expected speedup in computational efficiency is reproduced by numerical experiments on three zero-dimensional (0D) auto-ignition problems at varying scales from 53 species with 325 reactions of methane to 2115 species with 8157 reactions of n-hexadecane.

For the calculation of the remaining convective terms, FD schemes outperform FV schemes from the aspect of high-order spatial accuracy such that many high-order low-dissipation FD schemes employing characteristic decomposition are widely used. A challenge for the computational efficiency of such schemes is the quadratically increasing dimensionality of the convective flux eigensystem as the number of species increases. In the third part of this thesis, we present a remedy by splitting the eigensystem into two parts. One is the gas mixture part, which is subjected to the established characteristic decomposition schemes for single-fluid Euler equations. The other part corresponds to the species partial mass equations, which can be solved directly in the physical space as the decoupled sub-eigensystem for the species part is composed of two diagonal identity matrices. This property relies on the fact that species are advected with the same convective velocity. In this way, only the gas mixture part requires a characteristic decomposition, resulting in a much higher efficiency for the convective-flux calculation. Besides, to cure the inconsistency due to splitting, a consistent update of species mass fractions is proposed. Non-reactive and reactive test cases demonstrate that the proposed scheme, without deteriorating

high-order accuracy, successes in reducing the computational cost.

Acknowledgements

First and foremost, I would like to express my deep and sincere gratitude to Prof. Nikolaus A. Adams and PD Dr. Xiangyu Hu for their concurrent supervision and consistent encouragement during my PhD study. Xiangyu is always available to appeal to once I have questions. I am very grateful to his advising this work thoroughly, inspiring me with new ideas and encouraging me when I was frustrated. I am glad that our discussions on a broad range of research topics finally lead to some scientific publications. I greatly appreciate Prof. Adams for providing feedback to any research progress through weekly group meetings and email exchanges, for carefully revising my papers and allowing me to conduct researches fulfilling my personal interests. Their great visions over various disciplines, in-depth understanding of fluid mechanics & physics, strong passions into scientific research benefit me in this work I have done and surely the future career I will embark on. I also would like to thank Prof. Oskar J. Haidn for taking over the chair of my doctoral examination, and Dr. Chaouki Habchi from IFPEN for advising and reviewing my work as a thesis committee member.

It is always a pleasure to work with my collaborators in the Chair of Aerodynamics & Fluid Mechanics (AER), Department of Mechanical Engineering, Technical University of Munich (TUM), including Luhui Han, Shucheng Pan, Chi Zhang, Fu Lin, Xiuxiu Lyu, Zhe Ji, and also Dr. Stefan Adami and the outstanding "Nanoshock" group members (Jakob Kaiser, Aleksandr Lunkov, Vladimir Bogdanov, Nils Hoppe, etc). My research vision has been greatly broadened and friendship among us has been built up tightly through all the collaboration.

In addition, I truly enjoyed my time as a PhD candidate in AER, interacting with talented and friendly colleagues here. I wish to extend my gratitude to other members of our chair for their helpful discussions on the research and accompany during the study: Yujie Zhu, Zheng Fang, Zhaoguang Wang, Dr.Bian Xin, Dr. Rongzhong Huang, and many others. Particularly, I would like to thank the previous and current staff members in this chair, Amely Schwörer, Li Su, Angela Grygier, Dr. Christian Stemmer, Liu Hua and many others, for providing necessary equipments, maintaining computer systems, managing documents, and other services.

I feel deeply indebted to the European Union Marie Skłodowska-Curie Innovative Training Networks (ITN-ETN) project for the financial support of my research in TUM. Getting involved in extensive international exchanges and meetings with other IPPAD project members, my knowledge was refreshed from many automobile industry partners, concerning the development of next-generation Diesel engines, and my understandings into experimental fluid mechanics and computational fluid dynamics are also deepened. A lot of thanks should go to our coordinator Prof. Manolis Gavaises, School of Mathematics, CITY University of London, and the project manager Nikolas Chatziarsenis, for their inspiration, consideration and assistance all the way to date. Colleagues in the IPPAD project such as Aaron Rowane in Afton Chemical, Vikrant Mahesh in FAU, Carlos Rodriguez in CITY, Songzhi Yang in IFPEN and Xinda Zhu in Lund University and many others are also acknowledged.

My gratitude also goes to many other friends in Europe and China. I would like to give special mention to Deyu Huang, an interesting and nice friend from Taiwan and majoring in Opera and Vocal Performance in Italy, Louis Zhao and Jerry Zhang, two true friends and also TUM PhD candidates at different departments, and Yuanze Chen who obtained his master degree in TUM but is digging data & gold back in China. Dr. Jilin Hu, one of my earlier graduate schoolmates in SJTU and lifted his doctorate title in Denmark early this year, came to see me in the first Easter of my residence in Germany to relieve my initial homesickness, and he is currently working in the mid-east. Dr. Yang Li, one of my best high-school-mates, sharing with me his struggles as well as happiness in Shanghai and HUAWEI, continuously cares about my overseas life and career prospects. All the best to all of them.

An extremely special love is stressed here upon my precious girlfriend, Menglu Li (Laura Lee). From the very beginning of my flying to Munich from Shanghai via Doha where we met each other in the airport to this very moment of organizing my countless thanks, she is the unique one by my side daily and nightly. I cannot wait having a converging happy life together with her in the upcoming future.

Last but not the least, I am writing down my unreserved and complete gratitude to my parents, to whom I dedicate this dissertation. Without their endless love, priceless supports and great expectation throughout my growing-up and study, this thesis would never have been accomplished. 最后要毫无保留地谢谢我的父母，此文也正是献给他们。没有他们一如既往的爱、支持和期待，本文无法完成如此。

Contents

Dedicated to my parents & Menglu Li...
献给我的父母和李梦露...

Chapter 1

Introduction

1.1 Multi-component flow system

Flows in internal combustion engines, air-breathing propulsion systems and even rocket engines, as shown in Fig. 1.1, inevitably involve multiple components or species, considering the injection, mixing and reacting processes in which oxidizers like air or pure oxygen interact with fuels such as the considerably complex diesel or gasoline, much simpler ethylene or methane, and the simplest hydrogen. Even the simplest case of hydrogen/oxygen (H_2/O_2) combustion would produce several intermediate species such as OH, O, H and H_2O, etc., leading to the number of species $N_s > 2$. To accurately account for the above physical and chemical processes, all the species produced and consumed dynamically need to be considered in computational fluid dynamics (CFD) analyses of such flow scenarios, with appropriate multi-component models.

1.2 Previous numerical methods

A wide range of numerical methods have been proposed to model multi-component flow systems, especially aiming at the gaseous chemically reacting flows and vapor-liquid two-phase flows. One consistent computational model is expressed utilizing the mass fraction of each component or species, as long as the sum of all the mass fractions equals unity such that their total mass conservation can be guaranteed. The evolution of each component or species has a corresponding partial mass equation in terms of the mass fraction. Physically, all the species are mixed up, constituting the fluid mixture in a discrete local space, and advected at the same velocity. In combination with the momentum equation of the fluid mixture as well as an energy equation, the system of equations has a dimensionality of $N_s + N_d + 1$, where N_d represents the spatial dimension number of the flow in consideration. Therefore, we have the hyperbolic conservation laws of multi-species Euler equations with chemical reaction source terms, neglecting the flow viscosity for simplicity.

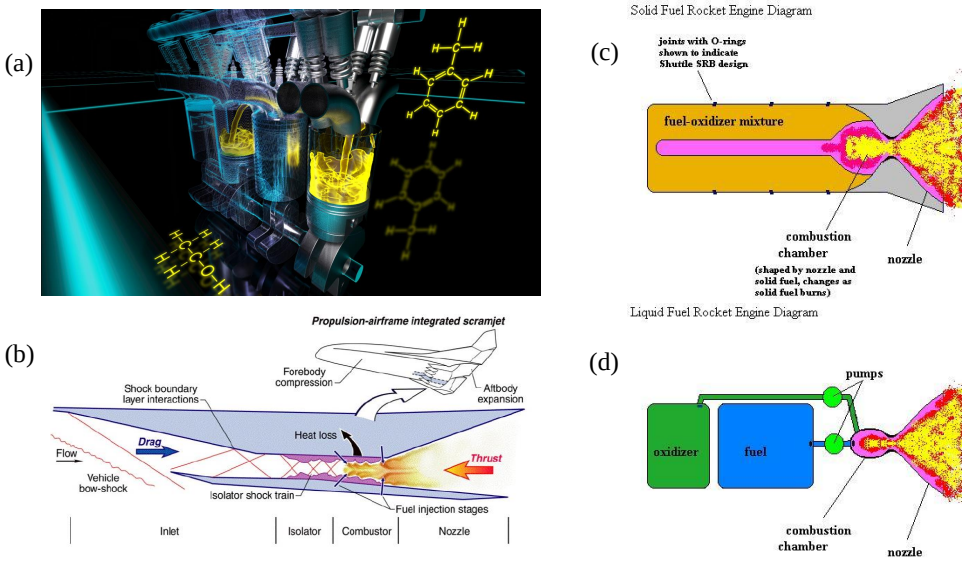

FIGURE 1.1: Schematics and examples of (a) internal combustion engines [1], (b) air-breathing propulsion systems [2] and (c) (d) rocket engines [3].

1.2.1 Numerical methods for spatial discretization

Finite volume formulation

Finite volume (FV) formulation is popularly used to approximate the convective fluxes at each cell face using both the left and right side states in a computational domain of discrete finite-volume cells. Owing to the body-fitted feature and easiness to implement for complex geometric configurations, the shock-capturing FV methods are usually very robust, together with a variety of upwind flux reconstruction schemes and slope limiters [4, 5, 6, 7, 8, 9]. Relatively low computational cost is also one big advantage of FV methods. The major disadvantage, however, lies in that without special treatment of improving the integral precision by setting additional Gauss points, the accuracy of FV methods is merely second order, resulting in the poor capability of capturing discontinuities and other interesting small flow structures unless very fine grids are employed.

Finite difference formulation

Unlike the FV formulation, finite difference (FD) methods are inherently extensible to be of high-order accuracy, with multi-point stencil based high-order interpolation schemes [10, 11, 12]. Before the costly multiple interpolation procedures, an approximate decoupling step (quasi-linearizion) is usually required to transform the coupled elements in the original vector space of conserved variables (or the physical space) to their characteristic space so as to avoid unnecessary numerical oscillations by direct interpolating coupled variables. The calculated flux vector in the characteristic space after interpolation will then be projected back onto the physical space

to form the desired physical flux at each mid-point of the grid. Several time operations of matrix-vector multiplication are involved, adding to the considerably high computational costs of FD methods. However, in contrast with FV methods using the same grid, the spatial resolution of FD methods upon discontinuities and other interesting small flow structures is much higher, due to the high-order low-dissipation shock-capturing nature.

1.2.2 Solvers for ordinary differential equations of chemical kinetics

Upon operator split from the spatial convection terms, the remaining source terms of the multi-species reactive Euler equations lead to a system of ordinary differential equations (ODEs) of chemical kinetics to solve. Temporal integrator for such an ODE system can be generally categorized into two types: explicit solvers and implicit solvers. **Explicit solvers** are usually Jacobian-free and thus relatively computational efficient, such as CHEMEQ/CHEMEQ2 [13, 14], MTS/HMTS [15], and ERENA [16], etc. However, they often encounter the severe challenge of numerical stiffness due to the large difference in multiple timescales of chemical reactions and the fact that the minimum characteristic time might be significantly smaller than the timestep sizes in CFD analysis. **Implicit solvers** such as VODE [17], DASAC [18], DASPK [19] and RADAU5 [20], etc., are specifically developed to treat numerical stiffness and therefore widely used, since they allow for the robust use of reasonably large timesteps. However, Jacobian evaluation and factorization in implicit solvers make them tend to be computationally very costly, compared with the explicit solvers, especially when the number of species N_s involved in the kinetic mechanism increases.

1.3 Objectives

The fundamental objective of the present work is to address some issues of the combined high computational costs of FD schemes and implicit ODE solvers for multi-species chemically reacting flow simulation, without loss of high-order accuracy. In particular, two recently developed methods are focused on improving the computational efficiency from two aspects: i) calculating the multi-species convective flux in the high-order FD formulation, and ii) integrating the ODE system resulted from detailed kinetic mechanisms with a new operator-splitting scheme, respectively.

Before the two methods are presented, the first part of work is towards the cure to a well-known spurious numerical problem [21, 22, 23, 24, 25, 26, 27], i.e. the incorrect propagation of the stiff detonation wave using modern shock-capturing schemes in under-resolved conditions of space and time. It comes to one's mind naturally that the most efficient simulation is based on possibly coarse grids and large timesteps with

tremendously reduced computational workloads, if acceptable accuracy of prediction can be guaranteed. This work is detailed in **Paper I**,

- JH Wang, S Pan, XY Hu, NA Adams, A split random time-stepping method for stiff and nonstiff detonation capturing, *Combustion and Flame*, **204**, 397–413, 2019,

which has been attached in Section B.1.

In **Paper II**, attached in Section B.2,

- JH Wang, S Pan, XY Hu, NA Adams, A species-clustered splitting scheme for the integration of large-scale chemical kinetics using detailed mechanisms, *Combustion and Flame*, **205**, 41-54, 2019,

we propose a species-clustered integrator for chemical kinetics with large-scale detailed mechanisms based on operator-splitting. Optimal clustering weighing both prediction accuracy and computational efficiency is determined, considering the typical detailed hydrocarbon/air combustion mechanisms at varying scales, from 53 species with 325 reactions of methane to 2115 species with 8157 reactions of n-hexadecane.

Paper III, see in Section B.3,

- JH Wang, S Pan, XY Hu, NA Adams, Partial characteristic decomposition for multi-species Euler equations, *Computers and Fluids*, **181**, 364–382, 2019,

presents a partial characteristic decomposition based FD scheme for the convection part of multi-species Euler equations. The computational efficiency of previous FD methods is limited by the quadratically increasing dimensionality of the convective flux eigensystem as the number of species increases, while for our proposed scheme the CPU time of calculating the convective flux can be reduced to linearly depend on the number of species N_s.

1.4 Outline

This thesis is structured as follows. In Chapter 2, the author outlines the concerned multi-species Euler equations with chemical reaction source terms, and introduces some existing numerical methods used for solving different parts of the equation system in a fractional step manner in the following Chapter 3. The main work of this thesis is still focused on improving the computational efficiency of corresponding parts step by step, with minimized sacrifice of high accuracy. As detailed in Chapter 4, an extensively studied spurious numerical phenomenon of stiff detonation capturing is dealt with using a new split random time-stepping method [28], a species-clustered integrator [29] for chemical kinetics with large-scale detailed mechanisms based on operator-splitting is aimed at solving the ODE system efficiently and accurately, and a

partial characteristic decomposition [30] for multi-species convective flux terms is developed to further reduce the CPU time of classical FD methods, with the presumed high-order accuracy being preserved. Finally, in Chapter 5 the state of proposed methods is concluded and potential applications in the future are discussed.

Chapter 2

Governing Equations

2.1 Multi-species reactive Euler equations

Consider the 3D multi-species (or multi-component) Euler equations with chemical reaction source terms, i.e.

$$U_t + F(U)_x + G(U)_y + H(U)_z = S(U), \tag{2.1}$$

where

$$\begin{aligned}
U &= \left(\rho, \rho u, \rho v, \rho w, \rho e_t, \rho y_1, \rho y_2, \cdots, \rho y_{N_s-1}\right)^T, \\
F(U) &= \left(\rho u, \rho u^2 + p, \rho vu, \rho wu, (\rho e_t + p)u, \rho y_1 u, \rho y_2 u, \cdots, \rho y_{N_s-1} u\right)^T, \\
G(U) &= \left(\rho v, \rho uv, \rho v^2 + p, \rho wv, (\rho e_t + p)v, \rho y_1 v, \rho y_2 v, \cdots, \rho y_{N_s-1} v\right)^T, \\
H(U) &= \left(\rho w, \rho uw, \rho vw, \rho w^2 + p, (\rho e_t + p)w, \rho y_1 w, \rho y_2 w, \cdots, \rho y_{N_s-1} w\right)^T, \\
S(U) &= \left(0, 0, 0, 0, 0, \dot{\omega_1}, \dot{\omega_2}, \cdots, \dot{\omega_{N_s-1}}\right)^T
\end{aligned} \tag{2.2}$$

are vectors of the conserved variables, convective flux in the x, y or z direction and source terms, respectively, with $\dot{\omega_i}$ representing rate of change of the i^{th} species concentration in the reactive gas mixture due to chemical kinetics consisting of N_s species. When the flow is inert without activating chemical reactions, source terms are replaced by a zero vector. The specific total energy including the specific internal energy e is $e_t = e + \frac{1}{2}(u^2 + v^2 + w^2)$.

To close the system, an equation of state (EoS) of the form

$$p = \rho \sum_{i=1}^{N_s} y_i \frac{R_u}{W_i} T \tag{2.3}$$

is used for the gas mixture, with y_i and W_i denoting the mass fraction and molecular weight of the i^{th} species, respectively, and R_u being the universal gas constant and p being the pressure. It is worthy of noting that the simple EoS can be also

replaced by any thermodynamical model to account for other fluids of different material properties, e.g. a vapor-liquid equilibrium (VLE) model [31, 32] which describes the vapor-liquid two-phase flow in the thermodynamical and mechanical equilibrium state in a diffuse-interface manner. We focus our attention on the gaseous reactive flow with the simple EoS here and afterwards.

The above conservation laws of mass, momentums and energy with source terms are usually solved by operator splitting. The first step is flow convection

$$S_c: \quad U_t + F(U)_x + G(U)_y + H(U)_z = 0, \tag{2.4}$$

assuming no chemical reactions and passive transport of all species.

The second step solves the system of ODEs of chemical kinetics

$$S_r: \quad \frac{\mathrm{d}y_i}{\mathrm{d}t} = \frac{\dot{\omega}_i}{\rho}, \quad i = 1, \ldots, N_s, \tag{2.5}$$

under adiabatic and constant-volume conditions with fixed total density ρ and constant specific internal energy e.

The first-order accurate Lie-Trotter splitting scheme [33] or the second-order Strang splitting [34] can be employed to approximate the solution from the discrete time level n to $n+1$ with a timestep Δt, i.e.

$$U^{n+1} = S_r^{(\Delta t)} \circ S_c^{(\Delta t)} U^n \quad \text{or} \quad U^{n+1} = S_c^{(\frac{\Delta t}{2})} \circ S_r^{(\Delta t)} \circ S_c^{(\frac{\Delta t}{2})} U^n, \tag{2.6}$$

with symbol '$\circ$' to separate each operator and to indicate that an operator is applied to the following arguments.

For the convection operator S_c, shock-capturing schemes are usually employed based on either finite volume (FV) or finite difference (FD) formulation for spatial discretization, in which high-order shock-capturing accuracy as well as high computational efficiency are desired. Low-order FV schemes approximate the cell-face flux function by upwind reconstruction using primitive or conserved variables, together with MUSCL interpolation schemes [35, 4] plus slope limiters and achieve generally second-order accuracy. High-order shock-capturing schemes are realized by characteristic-decomposition flux splitting (also referred as characteristic-wise flux splitting) to assemble the half-point convective flux using high-order interpolation schemes in FD methods.

For the reaction step S_r, an ODE solver such as VODE [17], CHEMEQ2 [14] and MTS/HMTS [36] can be used with or without adaptive error control.

Chapter 3

Numerical Methodology

In this chapter, the multi-species reactive Euler equations with source terms are managed with the state-of-the-art numerical methods in parts.

3.1 Convection operator – calculation of flux terms

Low-dissipation, high-order shock-capturing schemes designed for discretizing convection terms in the reactive Euler equations are crucial for accurate CFD analysis. The shock-capturing scheme should be capable of preserving sharp discontinuities without introducing spurious oscillations. For this purpose, a variety of high-order interpolation schemes can be used in the characteristic decomposition based FD methods, together with a flux-splitting scheme, to approximate the upwind convective flux.

In the characteristic-wise flux-splitting schemes, the Jacobian of convective flux in Eq. (2.4) is considered such as

$$A = \frac{\partial F}{\partial U} = L\Lambda R. \tag{3.1}$$

For a general formulation of the flux functions, F, G and H can be written as

$$\tilde{F}(U) = \begin{pmatrix} \rho M \\ \rho u M + p n_1 \\ \rho v M + p n_2 \\ \rho w M + p n_3 \\ (\rho e_t + p) M \\ \rho y_1 M \\ \rho y_2 M \\ \cdots \\ \rho y_{N_s-1} M \end{pmatrix}, \tag{3.2}$$

with the unit normal vector $\underline{n} = \{n_1, n_2, n_3\}$ and the velocity $M = n_1 u + n_2 v + n_3 w$. Thus, F is abbreviated for $\underline{n} = \{1, 0, 0\}$ and G is abbreviated for $\underline{n} = \{0, 1, 0\}$. H

corresponds to $\underline{n} = \{0, 0, 1\}$. The eigensystem of left and right matrices is

$$\tilde{L} = \tilde{R}^{-1} = \begin{pmatrix} \tilde{l}_1 \\ \tilde{l}_2 \\ \tilde{l}_3 \\ \tilde{l}_4 \\ \tilde{l}_5 \\ \tilde{l}_6 \\ \vdots \\ \tilde{l}_{N_s+4} \end{pmatrix} = \begin{pmatrix} \frac{b_2+M/c+b_3}{2} & \frac{-b_1u-n_1/c}{2} & \frac{-b_1v-n_2/c}{2} & \frac{-b_1w-n_3/c}{2} & \frac{b_1}{2} & \frac{-b_1z_1}{2} & \cdots & \frac{-b_1z_{N_s-1}}{2} \\ 1-b_2-b_3 & b_1u & b_1v & b_1w & -b_1 & b_1z_1 & \cdots & b_1z_{N_s-1} \\ \frac{Mn_2-v}{n_1} & -n_2 & \frac{1-n_2^2}{n_1} & \frac{-n_2n_3}{n_1} & 0 & 0 & \cdots & 0 \\ \frac{Mn_3-w}{n_1} & -n_3 & \frac{-n_2n_3}{n_1} & \frac{1-n_3^2}{n_1} & 0 & 0 & \cdots & 0 \\ \frac{b_2-M/c+b_3}{2} & \frac{-b_1u+n_1/c}{2} & \frac{-b_1v+n_2/c}{2} & \frac{-b_1w+n_3/c}{2} & \frac{b_1}{2} & \frac{-b_1z_1}{2} & \cdots & \frac{-b_1z_{N_s-1}}{2} \\ -y_1 & 0 & 0 & 0 & 0 & 1 & \cdots & 0 \\ \vdots & \vdots & \vdots & \vdots & \vdots & \vdots & \ddots & \vdots \\ -y_{N_s-1} & 0 & 0 & 0 & 0 & 0 & \cdots & 1 \end{pmatrix}, \tag{3.3}$$

and

$$\begin{aligned} \tilde{R} &= \left(\tilde{r}_1, \tilde{r}_2, \tilde{r}_3, \tilde{r}_4, \tilde{r}_5, \tilde{r}_6, \cdots, \tilde{r}_{N_s+4}\right) \\ &= \begin{pmatrix} 1 & 1 & 0 & 0 & 1 & 0 & \cdots & 0 \\ u-cn_1 & u & -n_2 & -n_3 & u+cn_1 & 0 & \cdots & 0 \\ v-cn_2 & v & n_1 & 0 & v+cn_2 & 0 & \cdots & 0 \\ w-cn_3 & w & 0 & n_1 & w+cn_3 & 0 & \cdots & 0 \\ H-cM & H-\frac{1}{b_1} & vn_1-un_2 & wn_1-un_3 & H+cM & z_1 & \cdots & z_{N_s-1} \\ y_1 & y_1 & 0 & 0 & y_1 & 1 & \cdots & 0 \\ \vdots & \vdots & \vdots & \vdots & \vdots & \vdots & \ddots & \vdots \\ y_{N_s-1} & y_{N_s-1} & 0 & 0 & y_{N_s-1} & 0 & \cdots & 1 \end{pmatrix}, \end{aligned} \tag{3.4}$$

where c represents the speed of sound and

$$\begin{aligned} H &= e + \frac{p}{\rho} + \frac{1}{2}Q, \\ z_i &= -\rho \frac{\partial p}{\partial \rho y_i} \Big/ \frac{\partial p}{\partial e}, \quad i = 1, 2, \cdots, N_s - 1, \\ b_1 &= \frac{1}{\rho c^2} \frac{\partial p}{\partial e}, \\ b_2 &= 1 + b_1 Q - b_1 H, \\ b_3 &= b_1 \sum_{i=1}^{N_s-1} y_i z_i, \end{aligned} \tag{3.5}$$

by defining $Q = u^2 + v^2 + w^2$. The pressure derivatives, $\frac{\partial p}{\partial e}$, $\frac{\partial p}{\partial \rho y_i}$ and $\frac{\partial p}{\partial \rho}$, are obtained by fixing other variables in the transformed EoS

$$p = p\left(\rho, e, \rho y_1, \cdots, \rho y_{N_s-1}\right).$$

If $n_1 = 0$, which is the case for calculation of flux function $G(U)$ or $H(U)$, l_3 and l_4 in Eq. (3.3) are invalid and can be replaced by

$$\begin{aligned} l_3^* &= \begin{pmatrix} \frac{Mn_1-u}{n_2} & \frac{1-n_1^2}{n_2} & -n_1 & \frac{-n_1n_3}{n_2} & 0 & 0 & \cdots & 0 \end{pmatrix}, \\ l_4^* &= \begin{pmatrix} \frac{Mn_3-w}{n_2} & \frac{-n_1n_3}{n_2} & -n_3 & \frac{1-n_3^2}{n_2} & 0 & 0 & \cdots & 0 \end{pmatrix}, \end{aligned} \tag{3.6}$$

if $n_2 \neq 0$. Correspondingly, r_3 and r_4 in Eq. (3.4) should be replaced by

$$\begin{aligned} r_3^* &= \begin{pmatrix} 0 & n_2 & -n_1 & 0 & un_2 - vn_1 & 0 & \cdots & 0 \end{pmatrix}^T, \\ r_4^* &= \begin{pmatrix} 0 & 0 & -n_3 & n_2 & wn_2 - vn_3 & 0 & \cdots & 0 \end{pmatrix}^T. \end{aligned} \tag{3.7}$$

If $n_2 = 0$ and $n_3 \neq 0$, $l_{3,4}$ and $r_{3,4}$ can be further replaced by

$$\begin{aligned} l_3^{**} &= \begin{pmatrix} \frac{Mn_1-u}{n_3} & \frac{1-n_1^2}{n_3} & \frac{-n_1n_2}{n_3} & -n_1 & 0 & 0 & \cdots & 0 \end{pmatrix}, \\ l_4^{**} &= \begin{pmatrix} \frac{Mn_2-v}{n_3} & \frac{-n_1n_2}{n_3} & \frac{1-n_2^2}{n_3} & -n_2 & 0 & 0 & \cdots & 0 \end{pmatrix}, \end{aligned} \tag{3.8}$$

and

$$\begin{aligned} r_3^{**} &= \begin{pmatrix} 0 & n_3 & 0 & -n_1 & un_3 - wn_1 & 0 & \cdots & 0 \end{pmatrix}^T, \\ r_4^{**} &= \begin{pmatrix} 0 & 0 & n_3 & -n_2 & vn_3 - wn_2 & 0 & \cdots & 0 \end{pmatrix}^T. \end{aligned} \tag{3.9}$$

Finally, eigenvalues in the diagonal characteristic matrix Λ in Eq. (3.1) are

$$M - c, M, M, M, M + c, M, \cdots, M. \tag{3.10}$$

Given the analytical expressions of left and right eigenvector as above, it is important to note that both eigenvectors and eigenvalues are locally defined at half points or cell faces such as $F_{i+\frac{1}{2},j,k}$ or $G_{i,j+\frac{1}{2},k}$. Therefore, it is required to obtain proper averaged state between two adjacent states U_L and U_R at grid points or neighboring cell centers. Following the Roe average [37, 38, 39] for ideal gas and its extension to multi-component non-equilibrium reactive flows [40], the U-property accounting for the jump conditions of two adjacent states can be satisfied by Roe-average the following variables

$$\begin{aligned} &\tilde{\rho} = \sqrt{\rho_L \rho_R}, \\ &\tilde{f} = \mu(f) = \frac{\sqrt{\rho_L} f_L + \sqrt{\rho_R} f_R}{\sqrt{\rho_L} + \sqrt{\rho_R}}, \quad f = u, v, w, H, e, y_1, \cdots, y_{N_s-1}. \end{aligned} \tag{3.11}$$

Left to be satisfied is the pressure jump condition

$$\Delta p = \widetilde{\left(\frac{\partial p}{\partial \rho}\right)} \Delta\rho + \widetilde{\left(\frac{\partial p}{\partial e}\right)} \Delta e + \sum_{i=1}^{N_s-1} \widetilde{\left(\frac{\partial p}{\partial \rho y_i}\right)} \Delta\left(\rho y_i\right), \tag{3.12}$$

where $\Delta(\cdot) = (\cdot)_R - (\cdot)_L$. Note that definitions for the averaged pressure derivatives are not unique, and Eq. (3.12) defines a hyperplane as

$$\alpha x + \beta y + \sum_{i=1}^{N_s-1} \gamma_i z_i = 1 \tag{3.13}$$

with

$$\begin{aligned} &\alpha \equiv \frac{\Delta\rho}{\Delta p}\phi, \quad \beta \equiv \frac{\Delta e}{\Delta p}\psi, \quad \gamma_i \equiv \frac{\Delta(\rho y_i)}{\Delta p}\eta_i, \\ &x \equiv \widetilde{\left(\frac{\partial p}{\partial \rho}\right)}/\phi, \quad y \equiv \widetilde{\left(\frac{\partial p}{\partial e}\right)}/\psi, \quad z_i \equiv \widetilde{\left(\frac{\partial p}{\partial \rho y_i}\right)}/\eta_i, \end{aligned} \tag{3.14}$$

where ϕ, ψ, η_i are the scaling factors [40].

Given all partial derivatives of pressure at the left and right states, we can first introduce Roe-averaged derivatives of pressure by imposing $\tilde{f} = \mu(f)$ in Eq. (3.11), i.e.

$$\begin{aligned} \overline{\left(\frac{\partial p}{\partial \rho}\right)} &= \mu\left(\frac{\partial p}{\partial \rho}\right), \\ \overline{\left(\frac{\partial p}{\partial e}\right)} &= \mu\left(\frac{\partial p}{\partial e}\right), \\ \overline{\left(\frac{\partial p}{\partial \rho y_i}\right)} &= \mu\left(\frac{\partial p}{\partial \rho y_i}\right), \quad i = 1, \cdots, N_s - 1. \end{aligned} \tag{3.15}$$

Then starting from point S

$$(x_s, y_s, z_{1s}, \cdots, z_{N_s-1_s}) = \left(\overline{\left(\frac{\partial p}{\partial \rho}\right)}/\phi, \overline{\left(\frac{\partial p}{\partial e}\right)}/\psi, \overline{\left(\frac{\partial p}{\partial \rho y_1}\right)}/\eta_1, \cdots, \overline{\left(\frac{\partial p}{\partial \rho y_{N_s-1}}\right)}/\eta_{N_s-1}\right),$$

its projection P

$$\left(x_p, y_p, z_{1p}, \cdots, z_{N_s-1_p}\right) = \left(\widetilde{\left(\frac{\partial p}{\partial \rho}\right)}/\phi, \widetilde{\left(\frac{\partial p}{\partial e}\right)}/\psi, \widetilde{\left(\frac{\partial p}{\partial \rho y_1}\right)}/\eta_1, \cdots, \widetilde{\left(\frac{\partial p}{\partial \rho y_{N_s-1}}\right)}/\eta_{N_s-1}\right)$$

onto the hyperplane defined by Eqs. (3.13)(3.14) can be determined by

$$\begin{aligned} x_p &= x_s + \alpha\Omega, \\ y_p &= y_s + \beta\Omega, \\ z_{ip} &= z_{is} + \gamma_i\Omega, \quad i = 1, \cdots, N_s - 1, \end{aligned} \tag{3.16}$$

where

$$\Omega = \frac{1 - \alpha x_s - \beta y_s - \sum_{i=1}^{N_s-1} \gamma_i z_{is}}{\alpha^2 + \beta^2 + \sum_{i=1}^{N_s-1} \gamma_i^2}. \tag{3.17}$$

State P on the plane naturally satisfies the pressure jump condition and might give a suitable set of derivatives which will be further employed in calculating averaged cell-face eigenvalues and eigenvectors in Eqs. (3.3) (3.4) and (3.10), together with

simple Roe-averaged values in Eq. (3.11). The consistent averaged speed of sound should be a positive real number and can be obtained by

$$\tilde{c}^2 = \widetilde{\left(\frac{\partial p}{\partial \rho}\right)} + \frac{\tilde{p}}{\tilde{\rho}^2}\widetilde{\left(\frac{\partial p}{\partial e}\right)} + \sum_{i=1}^{N_s-1} \tilde{y}_i \widetilde{\left(\frac{\partial p}{\partial \rho y_i}\right)} \tag{3.18}$$

with

$$\tilde{p} = \tilde{\rho}\left(\tilde{H} - \tilde{e} - \frac{\tilde{u}^2 + \tilde{v}^2 + \tilde{w}^2}{2}\right), \tag{3.19}$$

as in [38].

We now have obtained the approximate eigensystem located at the cell face between two cell-centered adjacent states. Decomposition of the multi-species Euler equations in the physical space can be done by projecting them onto the characteristic space with the left matrix $\tilde{L}$, where high-order interpolation schemes, e.g. WENO5 [41], can be used in combination with local Lax-Friedrich splitting for example. Finally, physical flux vectors are obtained by inverse transform of the system onto physical space with matrix $\tilde{R}$. E.g. for a cell face at $\{i+\frac{1}{2}, j, k\}$, stencils of six points/states are needed next to the cell face, i.e. $\{i', j, k\}$ with $i' = i-2, \cdots, i+3$, such that we have

$$\begin{aligned}
f_{i'} &= \tilde{L}_{i+\frac{1}{2}} F_{i'}, \\
q_{i'} &= \tilde{L}_{i+\frac{1}{2}} U_{i'}, \\
f^{\pm}_{i'} &= \frac{1}{2}\left(f \pm \lambda q\right)_{i'}, \\
\tilde{f}^{+}_{i+\frac{1}{2}} &= \mathrm{WENO5}\{f^{+}_{i'}, i' = i-2, \cdots, i+3\}, \\
\tilde{f}^{-}_{i+\frac{1}{2}} &= \mathrm{WENO5}\{f^{-}_{i''}, i'' = i+3, \cdots, i-2\}, \\
\tilde{F}_{i+\frac{1}{2}} &= \tilde{R}_{i+\frac{1}{2}}\left(\tilde{f}^{+}_{i+\frac{1}{2}} + \tilde{f}^{-}_{i+\frac{1}{2}}\right)
\end{aligned} \tag{3.20}$$

and $\tilde{F}_{i+\frac{1}{2}}$ is the expected convective flux in the physical space. Note that each λ is the maximum eigenvalue in Eq. (3.10) over stencils, and left and right matrices with tilde are defined in Eqs. from (3.3) to (3.9).

Several matrix multiplications with vectors have to be performed in the above process of calculating a cell-face flux such as $\tilde{L}_{i+\frac{1}{2}} F_{i'}$, $\tilde{L}_{i+\frac{1}{2}} U_{i'}$ and $\tilde{R}_{i+\frac{1}{2}} \tilde{f}^{\pm}_{i+\frac{1}{2}}$. In addition to the element-by-element interpolation by WENO5, operations upon matrix products are computationally very expensive. As the number of species increases, dimensionality of the eigensystem, $N_s + 4$, increases quadratically, such that the computational cost for these operations will be dramatically raised.

3.2 Reaction operator – temporal integration of chemical ODE system

For common nonequilibrium chemical kinetics, chemical production rates in Eq. (2.5) are derived from a reaction mechanism that consists of N_s species and N_r reactions

$$\sum_{i=1}^{N_s} \nu_{ji}^f X_i \Longleftrightarrow \sum_{i=1}^{N_s} \nu_{ji}^b X_i, \quad j = 1, \ldots, N_r, \tag{3.21}$$

where ν_{ji}^f and ν_{ji}^b are the stoichiometric coefficients of species i with description X_i appearing as a reactant and as a product in reaction j. The total production rate of species i in Eqs. (2.2) and (2.5) is the sum of the production rate from each single elementary reaction as

$$\dot{\omega}_i = W_i \sum_{j=1}^{N_r} (\nu_{ji}^b - \nu_{ji}^f) \left[k_j^f \prod_{l=1}^{N_s} \left[\frac{\rho_l}{W_l} \right]^{\nu_{jl}^f} - k_j^b \prod_{l=1}^{N_s} \left[\frac{\rho_l}{W_l} \right]^{\nu_{jl}^b} \right], \tag{3.22}$$

with k_j^f and k_j^b denoting the forward and backward reaction rates of each chemical reaction, and $\rho_l = y_l \rho$.

The temperature-dependent reaction rates are practically calculated using the Arrhenius law

$$k_r = A T^B \exp(-T_{ign}/T), \tag{3.23}$$

where the subscript r is f for forward reactions or b for backward reactions and T is the temperature. Parameters A, B and T_{ign} for the forward rate of each reaction are often given in the mechanism. Backward rates often need to be calculated from the equilibrium constant K_{eq} and k_f by assuming the corresponding reaction to be in chemical equilibrium, i.e. $K_{eq} = k_f / k_b$ [42]. The third-body effect is accounted for by the summation of third-body collision efficiencies times the corresponding molar densities of species. Pressure-dependent reaction rates are also possible, referring to [43].

For the reaction step S_r, any ODE solver, explicit or implicit, can be adopted to integrate the state vector $\{y_1, \ldots, y_{N_s}\}$ from time t_n to t_{n+1}, so that the complete thermodynamical state is determined. We need to update the latest temperature T implicitly using the thermodynamic relation

$$h(y_1, \ldots, y_{N_s}, T) - e = \frac{p(y_1, \ldots, y_{N_s}, T)}{\rho}, \tag{3.24}$$

where the mixture enthalpy h is iteratively calculated using the empirical polynomial approximations [44] and pressure p can be substituted by the EoS of ideal gas mixtures in Eq. 2.3, with the internal energy e fixed to be constant during the timestep interval.

3.2.1 A species-clustered splitting scheme with the implicit solver VODE

To overcome severe numerical stiffness due to the large difference in multiple timescales of chemical reactions, implicit solvers such as VODE are usually preferred, due to its allowing for the robust use of reasonably large timesteps.

Operator splitting by species

The solution vector $\Phi = \{y_1, \cdots, y_{N_s}\}^T$ at time level n is integrated through the above ODE system for one timestep of Δt with the implicit solver VODE [17] to obtain

$$\Phi^{n+1} = R_{\Delta t}(\Phi^n). \tag{3.25}$$

The operator R represents the time integration by VODE. Upon operator splitting by species, we obtain

$$\Phi^{n+1} = R_{\Delta t}(\Phi_1^n) \circ R_{\Delta t}(\Phi_2^n) \cdots \circ R_{\Delta t}(\Phi_N^n), \tag{3.26}$$

corresponding to the Lie-Trotter splitting scheme [33], where Φ_k denotes the mass fractions of the species clustered in subset S_k out of N subsets in total. Clustering of species in each subset obeys

$$\begin{aligned} &\Phi = \{\Phi_1, \cdots, \Phi_N\}^T, \\ &S = \cup_{k=1}^{N} S_k,\ S_i \cap S_j = \emptyset \text{ if } i \neq j. \end{aligned} \tag{3.27}$$

Each subset of species cluster should have no overlap with others, and an almost equal number of species in each subset is assumed varying by at most one species, which requests a balanced partition/clustering algorithm [45]. The extension to higher-order splitting of Strang [34] is straightforward but inevitably more time consuming. Recalling that the scaling of computational cost to the number of species or the size of the kinetic mechanism involved using an implicit solver such as VODE is [46]

$$t_{\mathrm{CPU}} \sim \mathcal{O}\left(N_s^2\right) \text{ to } \mathcal{O}\left(N_s^3\right), \tag{3.28}$$

the total cost after species splitting can be reduced to

$$t'_{\mathrm{CPU}} \sim \mathcal{O}\left(\frac{N_s^2}{N}\right) \text{ to } \mathcal{O}\left(\frac{N_s^3}{N^2}\right), \tag{3.29}$$

assuming equal computational consumption for each subsystem after species-splitting. A large mechanism consisting of ten thousand species, e.g., split the system into ten

clusters with the Lie-Trotter scheme, results in a computational speedup of ten to a hundred times, without the need for additional sparse matrix techniques [47, 48, 49].

The essence of operator splitting by species for chemical kinetics lies in clustering species into subsets, each corresponding to a sub-ODE-system to be integrated by VODE or other implicit solvers. The merits of operator splitting by species are improved speedup of computational efficiency without changing the implicit solver, fast convergence and numerical stability [50].

Graph-based species clustering

A chemical reaction system with multiple species and reactions can be translated to a bi-partite graph [51], in which two sets of nodes represent the chemical species and reactions. Herein, we simply consider a finite graph consisting of the chemical species only and the non-linear coupling between pairs of species through reactions is abstracted as undirected edges linking every two nodes of species. For the sake of illustration, we consider $N_s = 6$ six species, $\{A, B, C, D, E, F\}$, and six first-order one-way reactions, i.e.

$$\begin{aligned} A \xrightarrow{k_1} C,\ B \xrightarrow{k_2} C,\ C \xrightarrow{k_3} B, \\ D \xrightarrow{k_4} C,\ E \xrightarrow{k_5} D,\ F \xrightarrow{k_6} D, \end{aligned} \tag{3.30}$$

where $k_1, \cdots, k_6$ are constant reaction rates. The exact solution for this problem can be easily obtained using symbolic computations of MATLAB® [52].

First we construct the graph of species, Fig. 3.1(a). We may have two different clusterings I and II with two subsets ($N = 2$). Clustering I in Fig. 3.1(b) is obtained by cutting off the link between species C and D. The strong couplings within clusters $\{A, B, C\}$ and $\{D, E, F\}$ are preserved. Upon clustering loosely coupled $\{A, E, F\}$ together and leave the rest to compose the other cluster, we obtain Clustering II. The distance in the graph between (A, E) or (A, F) is remote as they are separated by two other species. The difference of the two clusterings also reflects in the rearranged Jacobian matrices by the order of splitting and clustering as shown in Figs. 3.1(c) and (d). We can see that for Clustering I, when solving the cluster of $\{A, B, C\}$ first, only the effect of species D is considered as constant since k_4 is not within the sub-Jacobian matrix. When solving the other cluster $\{D, E, F\}$ subsequently, species A, B and C have no effect due to the corresponding zero entries. In total, the splitting error is attributed to only one element in the Jacobian, i.e. the k_4 block (red color) in Fig. 3.1(c). For Clustering II, the solution of the first cluster $\{A, E, F\}$ introduces no splitting error, whereas errors will occur when solving the cluster $\{B, C, D\}$, due to first-order approximation of $k_1 y_A$ for the production of species C and $k_5 y_E + k_6 y_F$ for the production of species D.

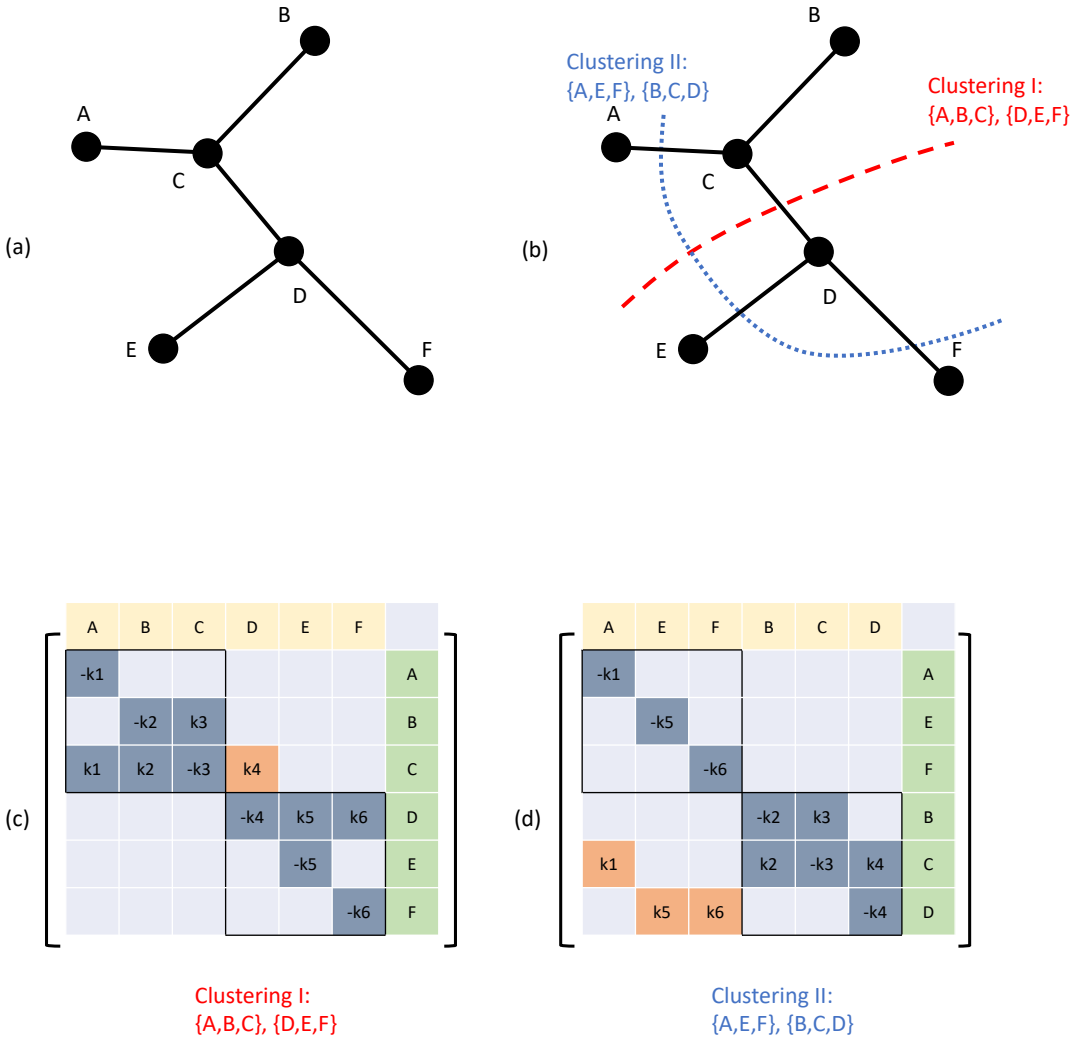

FIGURE 3.1: Reaction system example for species clustering. (a) Each node represents one species in $\{A, B, C, D, E, F\}$, and the edge, e.g. $e(A, C)$, indicates that linked two species participate in at least one reaction as reactant or product; (b) two equal-sized clusterings are easily obtained as $(\{A, B, C\}, \{D, E, F\})$ and $(\{A, E, F\}, \{B, C, D\})$ by cutting off corresponding edges; (c) rearranged Jacobian matrix in the order of Clustering I; (d) rearranged Jacobian matrix in the order of Clustering II.

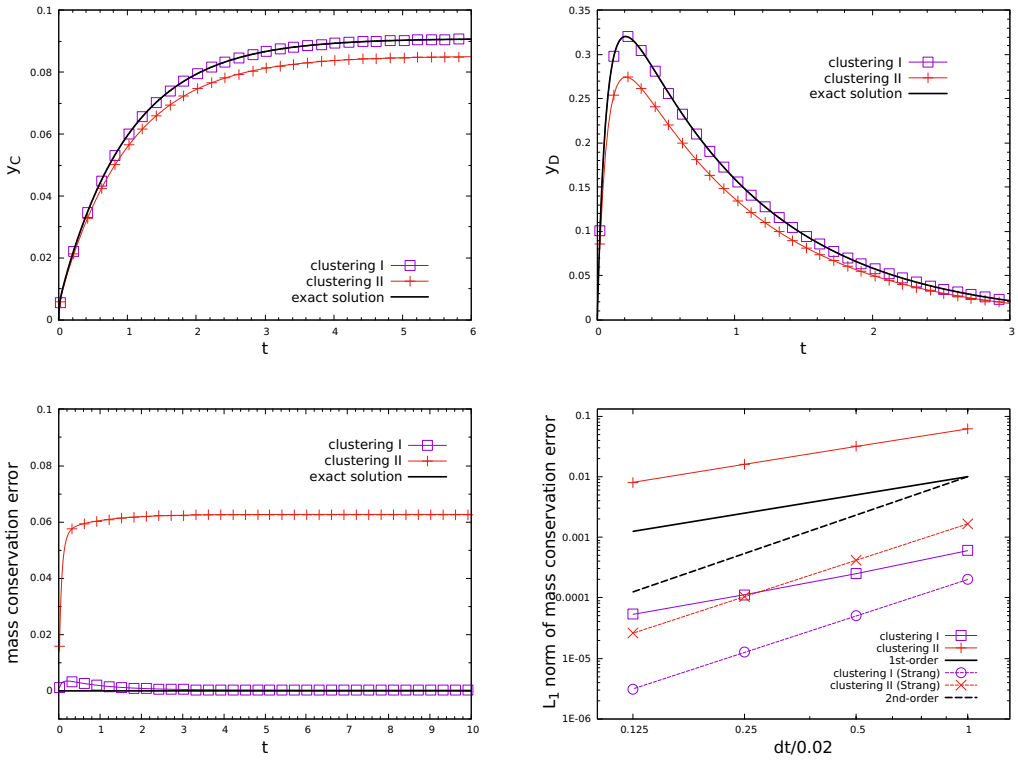

FIGURE 3.2: Numerical integration results with two clusterings by Lie-Trotter and Strang splittings, compared with the exact solution. Reaction rates are $k_1 = 1, k_2 = 10, k_3 = 100, k_4 = 1, k_5 = 10, k_6 = 20$, and the initial condition is $y_A = 0.6, y_E = 0.2, y_F = 0.2$ with zero mass fractions of B, C, D. The base timestep size is $\Delta t = 0.02$.

Numerical tests, in Fig. 3.2, show that Clustering I agrees quite well with the exact solution, while Clustering II underestimates both the mass fractions of species C and D. This observation is in agreement with the previous discussion about operator splitting.

Given a prescribed number of clusters N, there are many possible clustering combinations. One simple strategy is to cluster the species according to species indices appearing in the mechanism. Another very promising strategy is to cluster all 'close' nodes in the graph into a subset, corresponding to having species with strong interactions in the same cluster. In this paper, we introduce diffusion maps [53, 54, 55] as a non-linear technique for dimensionality reduction, data set parameterization and clustering, to serve the purpose.

Let $G = (\Omega, W)$ be a finite graph of n nodes, where the weight matrix $W = \{w(x,y)\}_{x,y\in\Omega}$ is symmetric and component-wise positive [55]. The definition of weight matrix needs to reflect the degree of affinity of nodes x and y. Diffusion maps start with a user-defined weight matrix and utilize the idea of Markov random walk to describe the connectivity of nodes through a diffusion process. For technical details of diffusion maps, we refer to [53, 54, 55].

For the above reaction system, we define, with the help of species graph in Fig. 3.1(a), the weight matrix W by

$$w(x,y) = \begin{cases} max(k_j), & \text{if } x \text{ and } y \text{ both participate in reaction } j, \\ \epsilon, & \text{otherwise,} \end{cases} \tag{3.31}$$

where ϵ takes a small positive value to avoid zero entries, e.g. $\epsilon = 10^{-12}$. The diagonal elements in the weight matrix, $w(x,x)$, can be defined as

$$w(x,x) = max(w(x,y)_{y\neq x}). \tag{3.32}$$

In combination with the reaction rates given in Fig. 3.2, the weight matrix obtained by the above definition is shown in Fig. 3.3. Using diffusion maps to analyze the graph based on our defined weight matrix, we can project the set of species into a diffusion space with at most n dimensions, where the pairwise distance reveals the connectivity between two species. In Fig. 3.3, it is shown that the species are projected onto a x_1x_2 plane using the first two dimensions of the diffusion space. We can see that species A, B and C almost collapse into one point and locations of species D, E and F in the x_1 direction (which is also the first and dominant dimension) are also very close to each other. Their coordinates in the second dimension separate the three species. However, the centroids of subset $\{A,B,C\}$ and subset $\{D,E,F\}$ are far from each other. Accordingly, a straightforward clustering using the k-means algorithm (setting $k \equiv N = 2$) can be easily obtained, i.e. $(\{A,B,C\},\{D,E,F\})$. This clustering from

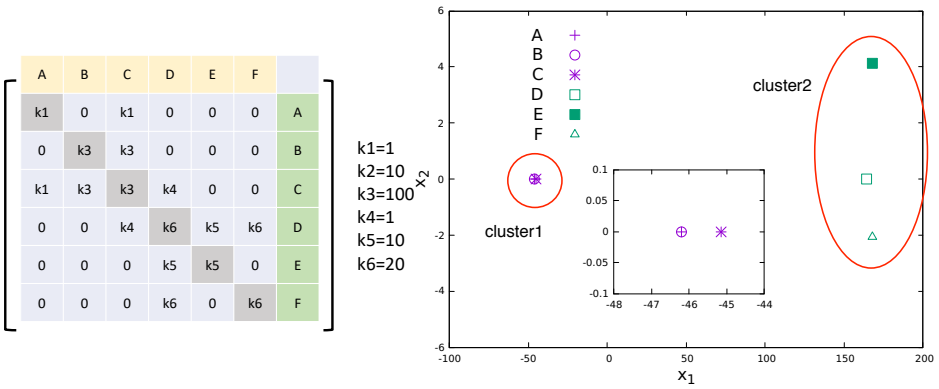

FIGURE 3.3: Weight matrix of diffusion maps for the reaction system (left); embedding and clustering of species in 2D diffusion space (right)

diffusion maps is the same as the previous Clustering I, indicating that it is the optimal case of two clusters for the reaction system above with minimum splitting errors. In Fig. 3.2, we can also observe that exact mass conservation is violated by operator splitting with first-order convergence rate using the Lie-Trotter scheme. However, the optimal Clustering I has a significantly lower mass conservation error than Clustering II. An additional treatment for the correction of mass-conservation errors as in [16] can be applied. In this illustrative example, it should be noted that the underlying fact of $k_4 = 1$ being quite small benefits Clustering I through the weight matrix W in Eq. (3.31). If k_4 becomes larger, both the previous manual clustering and the current diffusion maps based clustering would be different, with the coupling between species C and D to be preserved and both being clustered into the same subset.

For much more complicated realistic chemical kinetics especially involving fuel combustion mechanisms, reaction rates are not always constant but depend on temperature or even pressure of the mixture. This normally can be expressed by the finite-rate Arrhenius model [14, 56] and thus the weight matrix as above should also take into account the varying reaction rates with temperature. Rather than sampling at a single temperature, e.g. the initial temperature of an auto-ignition problem of combustible gas mixtures, we take many temperature samples in order to construct a representative weight matrix. The derived clustering by diffusion maps based on such a weight matrix can be stored and used for other conditions as long as the same mechanism is involved. In such way, the determination of the weight matrix as well as the clustering procedure can be treated as a preprocessing step instead of costly on-the-fly clustering. Since multiple scales of the absolute reaction rates exist, usually spanning several orders of magnitude, logarithmic scaling of the reaction rates can be performed to avoid underestimating the slow reactions. Also, normalization in each row of the matrix relative to the diagonal species is carried out as

$$w(x,y) = \frac{w(x,y)}{w(x,x)}, \tag{3.33}$$

and

$$w(x,y) = max(w(x,y), w(y,x)) \tag{3.34}$$

for all species pairs is further checked to guarantee the symmetry of weight matrix in the diffusion maps.

3.2.2 A split reaction-by-reaction explicit solver

In addition to the above implicit scheme, we also introduce and develop an explicit ODE solver by utilizing operator splitting upon the nonequilibrium chemical kinetics so that a multi-reaction system can be decoupled into a series of single reaction steps.

By operator splitting [57, 50], we can decouple the multi-reaction system, e.g. by Lie-Trotter splitting, as

$$S_r: \quad R_{1st}^{(\Delta t)} = R_{N_r}^{(\Delta t)} \circ R_{N_r-1}^{(\Delta t)} \circ \cdots \circ R_2^{(\Delta t)} \circ R_1^{(\Delta t)}, \tag{3.35}$$

where the operator R_j corresponds to a single reaction j and is independent of all other reactions. The reaction-by-reaction idea resembles a meso-scale model of microscopic kinetics where one molecule/atom can only experience one reaction at a time instance. This is also the case with stochastic simulation of chemical kinetics [58]. At macroscopic scale, reactions involving large numbers of species molecules/atoms are considered as simultaneously occurring processes. In [57] the second-order accurate Strang splitting is adopted, starting with the fastest reaction and ending with the slowest for half a timestep and then backwards for another half timestep. In our approach we simply take the traversal order not according to reaction rates but to the reaction-mechanism index sequence

$$\begin{aligned} S_r: \quad R_{2nd}^{(\Delta t)} &= R_1^{(\frac{\Delta t}{2})} \circ R_2^{(\frac{\Delta t}{2})} \circ \cdots \circ R_{N_r}^{(\frac{\Delta t}{2})} \circ R_{N_r}^{(\frac{\Delta t}{2})} \circ R_{N_r-1}^{(\frac{\Delta t}{2})} \circ \cdots \circ R_1^{(\frac{\Delta t}{2})} \\ &= \overline{R_{1st}^{(\frac{\Delta t}{2})}} \circ R_{1st}^{(\frac{\Delta t}{2})}, \end{aligned} \tag{3.36}$$

where $\overline{R_{1st}}$ is the reverse operator of R_{1st}. Accordingly, for each R_j, we have

$$\begin{aligned} R_j: \quad & \sum_{i=1}^{N_s} \nu_{ji}^f X_i \Longleftrightarrow \sum_{i=1}^{N_s} \nu_{ji}^b X_i, \quad \frac{dy_i}{dt} = \frac{\dot{\omega}_i{}^j}{\rho}, \quad i = 1, \ldots, N_s, \\ & \dot{\omega}_i{}^j = W_i(\nu_{ji}^b - \nu_{ji}^f) \left[k_j^f \prod_{l=1}^{N_s} \left[\frac{\rho_l}{W_l} \right]^{\nu_{jl}^f} - k_j^b \prod_{l=1}^{N_s} \left[\frac{\rho_l}{W_l} \right]^{\nu_{jl}^b} \right]. \end{aligned} \tag{3.37}$$

We now rewrite the ODE in Eq. (3.37) in the following form [14]

$$\frac{dy_i}{dt} = q_i^j - p_i^j y_i, \quad i = 1, \ldots, N_s, \tag{3.38}$$

where $q_i^j \geq 0$ is the production rate and $p_i^j y_i \geq 0$ is the loss rate for the i^{th} species through reaction j.

Following the operator splitting of reactions, we continue to split each reaction j into a forward reaction and a backward reaction (for an irreversible reaction, it can be interpreted as a reversible reaction with zero backward reaction rate)

$$R_j^{(\Delta t)} = R_{j,b}^{(\Delta t)} \circ R_{j,f}^{(\Delta t)} \tag{3.39}$$

such that the species involved will either gain mass or lose mass through the one-way forward/backward reaction from Eq. (3.38), i.e.

$$\text{mass gain} : q_i^j \geq 0,\ p_i^j y_i = 0 \text{ or mass loss} : q_i^j = 0,\ p_i^j y_i \geq 0, \tag{3.40}$$

with the simplified

$$\begin{aligned} q_i^{j,f} &= \frac{W_i}{\rho} \nu_{ji}^b \left[k_j^f \prod_{l=1}^{N_s} \left[\frac{\rho_l}{W_l} \right]^{\nu_{jl}^f} \right],\ p_i^{j,f} y_i = 0 \quad \text{for product species,} \\ q_i^{j,f} &= 0,\ p_i^{j,f} y_i = \frac{W_i}{\rho} \nu_{ji}^f \left[k_j^f \prod_{l=1}^{N_s} \left[\frac{\rho_l}{W_l} \right]^{\nu_{jl}^f} \right] \quad \text{for reactant species} \end{aligned} \tag{3.41}$$

for the forward reaction of Eq. (3.37). The backward reaction can be determined accordingly upon exchanging its reactants and products.

Since each elementary reaction is decoupled from the others and each reaction again is split into two opposite unidirectional reactions, finally only a single reaction equation of the type

$$aA + bB + \cdots \longrightarrow xX + yY + \cdots \tag{3.42}$$

is considered in each operation. Mass conservation and positivity of mass fractions can be properly treated.

For the simple cases of Eq. (3.42), one may find analytical solutions. However, for the general form of Eq. (3.42) whose analytical solution is not explicitly known or difficult to derive, a more convenient alternative is to use quasi-steady-state (QSS) methods to obtain the approximate exact solution. QSS methods are based on the exact solution of Eq. (3.38) for constant p_i^j and q_i^j [59, 60], i.e.

$$y_i^{n+1} = y_i^n e^{-p_i^j \Delta t} + \frac{q_i^j}{p_i^j}(1 - e^{-p_i^j \Delta t}), \quad \text{for all } \nu_{ji}^b - \nu_{ji}^f \neq 0. \tag{3.43}$$

As generally p_i^j and q_i^j depend on $\{y_1, \ldots, y_{N_s}\}$ in Eq. (3.40) or (3.41), Eq. (3.43) provides a linear approximation. For the QSS-based SPRANTS method, the stable timestep size is not limited to the characteristic time scales of the chemical species

and thus a larger timestep implying less computational efforts is possible [57].

Treatment for mass conservation

Employing QSS in Eq. (3.43) for all the species participating in reaction j (with $\nu_{ji}^b - \nu_{ji}^f \neq 0$),

$$\sum_i y_i^{n+1} = \sum_i \left(y_i^n e^{-p_i^j \Delta t} + \frac{q_i^j}{p_i^j}(1 - e^{-p_i^j \Delta t}) \right) \tag{3.44}$$

may not necessarily be unity so that mass may be not exactly conserved. To cure this problem, one may only advance y_k^n to y_k^{n+1} of a reactant k by Eq. (3.43) and update all other $\{y_{i,i=1,\cdots,N_s,i\neq k}\}^{n+1}$ by mass conservation of a single reaction equation in Eq. (3.37). This merit of knowing the exact net gain or loss of mass of other species originates from the fact that each reaction in Eq. (3.37) is decoupled from others. Therefore, for the reactant k, combining Eqs. (3.43) and (3.41) we have

$$y_k^{n+1} = y_k^n e^{-p_k^j \Delta t} \tag{3.45}$$

and for the other species $i \neq k$, including other reactants and all the products in reaction j, the change of mass fraction $\Delta y_i = y_i^{n+1} - y_i^n$ should obey

$$\frac{\Delta y_i / W_i}{\nu_{ji}^b - \nu_{ji}^f} = \frac{\Delta y_k / W_k}{\nu_{jk}^b - \nu_{jk}^f}, \tag{3.46}$$

giving the update

$$y_i^{n+1} = y_i^n + \Delta y_i = y_i^n + \frac{\nu_{ji}^b - \nu_{ji}^f}{\nu_{jk}^b - \nu_{jk}^f} \frac{W_i}{W_k} \Delta y_k. \tag{3.47}$$

It is easy to see that $\sum_{i=1}^{N_s} \Delta y_i = 0$, which is equivalent to $\sum_{i=1}^{N_s} y_i = 1$ for mass conservation.

Positivity-preserving treatment

Without loss of generality, we consider the forward reaction j and assume that reactant species k has $\nu_{jk}^b = 0$ in Eq. (3.45), as $\nu_{jk}^f > 0$ is prescribed for reactants. Similarly assuming that another reactant species i also has $\nu_{ji}^f > 0$ and $\nu_{ji}^b = 0$, we combine Eqs. (3.45) and (3.47) to obtain

$$y_i^{n+1} = y_i^n - \frac{\nu_{ji}^f}{\nu_{jk}^f} \frac{W_i}{W_k} y_k^n + \frac{\nu_{ji}^f}{\nu_{jk}^f} \frac{W_i}{W_k} y_k^n e^{-p_k^j \Delta t}. \tag{3.48}$$

Recalling Eq. (3.41) for reactants i and k, we have

$$\frac{p_i^j y_i}{p_k^j y_k} = \frac{\nu_{ji}^f}{\nu_{jk}^f}\frac{W_i}{W_k}. \tag{3.49}$$

Upon rearranging Eq. (3.49) and substitution into Eq. (3.48) we obtain

$$y_i^{n+1} = y_i^n \frac{p_k^j - p_i^j}{p_k^j} + \frac{\nu_{ji}^f}{\nu_{jk}^f}\frac{W_i}{W_k} y_k^n e^{-p_k^j \Delta t}. \tag{3.50}$$

With the aid of Eq. (3.50), it is readily seen that positivity of y_i^{n+1}, i.e. $y_i^{n+1} \geq 0$, is achieved when $p_k^j \geq p_i^j$ since the third term is always non-negative. Therefore, in order to preserve the positivity of species mass fractions, reactant species k using the QSS approximation should satisfy

$$p_k^j = max\{p_i^j\} \quad \text{for all the reactant species in reaction } j. \tag{3.51}$$

Regarding the positivity for the choosen reactant k, according to Eq. (3.45), it is inherently satisfied through positivity of the exponential function. Eq. (3.45) implies that $0 \leq y_k^{n+1} < 1$ due to the negative exponent such that mass fractions of all species through reaction j are bounded within [0,1] as a result of mass conservation.

3.3 Time discretization

To improve the overall accuracy in time, the strong stability-preserving (SSP) Runge-Kutta schemes [61] are usually employed. Considering the 3rd-order SSP Runge-Kutta scheme, the generalized ODE $\frac{d\phi}{dt} = L(\phi)$ is updated from t^n to t^{n+1} by

$$\begin{aligned}
\tilde{\phi}^{n+1} &= \phi^n + \Delta t L(\phi^n), \\
\bar{\phi}^{n+1} &= \frac{3}{4}\phi^n + \frac{1}{4}\tilde{\phi}^{n+1} + \frac{1}{4}\Delta t L(\tilde{\phi}^{n+1}), \\
\phi^{n+1} &= \frac{1}{3}\phi^n + \frac{2}{3}\bar{\phi}^{n+1} + \frac{2}{3}\Delta t L(\bar{\phi}^{n+1}).
\end{aligned}$$

3.4 Boundary conditions

Boundary conditions (such as inflow/outflow, periodic, symmetric, etc.) are easily imposed using ghost cells outside the domain immediately after the primitive and conserved variables at corresponding internal cells are updated.

Chapter 4

Summaries of publications

In this chapter, the relevant publications of this thesis are briefly summarized.

4.1 A split random time-stepping method for stiffand nonstiff detonation capturing

One of the main challenges for numerical computation of chemically reacting flows are widely varying time scales of chemical kinetics, which may be orders of magnitude faster than the fluid flow time scale [21, 22, 23]. Such cases exhibit numerical stiffness due to the source terms representing chemical reactions [24]. When the chemical scales are not resolved numerically in time and space, a spurious solution may occur exhibiting incorrect propagation of discontinuities and nonphysical states. Here a new operator splitting method for not only stiff but also nonstiff detonation capturing in a unified manner in Paper I [28] is summarized.

4.1.1 Summary of the publication

We develop a split random time-stepping method for chemically reacting flows with general nonequilibrium chemistry in a unified manner, regardless of stiff or nonstiff source terms and under- or well-resolved conditions in space and time. Unlike Bao & Jin's random projection method, the activation and deactivation of chemical reactions in the reaction step is not projected onto two prescribed equilibrium states, but onto two time-dependent states corresponding to advancing the reaction by one timestep forward and interrupting the reaction, respectively. The criterion to activate a reaction follows from comparison of the local computed temperature with a randomized temperature depending on the states of the forward step and its adjoint. To randomize each reaction process, the multi-reaction system is split reaction by reaction [57, 50]. In this way, the multi-reaction system of the nonequilibrium chemical kinetics can be decoupled into a series of single reaction steps. Similarly, each reaction can be further split into a forward reaction and a backward reaction (for an irreversible reaction, it can be interpreted as a reversible reaction with zero backward

reaction rate). By adding a drift term into the random temperature sampling, the proposed method recovers the solution of a deterministic fractional step method in nonstiff cases with increasing resolution.

4.1.2 Individual contributions of the candidate

My contribution to this work was the development of the method and the corresponding computer code for its implementation. I have performed simulations, analyzed the results, and written the manuscript for publication.

4.2 A species-clustered splitting scheme for the integration of large-scale chemical kinetics using detailed mechanisms

Gasoline, diesel and jet fuels, particularly those derived from petroleum sources, are composed of hundreds of components [75]. As the number of hydrocarbon species grows, so does the dimensionality of kinetic mechanism to model hydrocarbon oxidation. For example, the detailed mechanism for methyl decanoate, a biomass fuel surrogate, consists of 3036 species and 8555 reactions [76, 77]. A species-clustered integrator for chemical kinetics with large detailed mechanisms based on operator-splitting, presented in Paper II, is discussed in this section, with a brief review on related works in the literature that inspired our ideas.

4.2.1 Summary of the publication

The quadric/cubic scaling of CPU time to mechanism size using implicit ODE solvers implies that the computational cost of solving a sequence of smaller subsystems ought to be much less than that of solving the entire system in one step. Therefore, unlike the above use of operator splitting in decoupling two or more physical processes, we start with splitting the large-scale chemical kinetics in terms of the involved species. Once the participating species of the large mechanism have been clustered into subsets of a smaller and equal size, an implicit solver can be applied to each group with significantly reduced matrix dimension. To minimize the splitting error, diffusion maps [54, 55, 53] are utilized to analyze the pairwise interaction relations of species by constructing a weight or similarity matrix of chemical kinetics, such that strongly interacting and mutually dependent species can be clustered into the same group. To partition the species into equal clusters, a balanced k-means algorithm [45] is employed.

4.2.2 Individual contributions of the candidate

My contribution to this work was the development of the method and the corresponding computer code for its implementation. I have performed simulations, analyzed the results, and written the manuscript for the publication.

4.3 Partial characteristic decomposition for multi-species Euler equations

With high-order spatial accuracy, characteristic decomposition based FD schemes are widely used for simulating compressible gas flows with multiple species. However, a challenge for the computational efficiency of such schemes is the quadratically increasing dimensionality of the convective flux eigensystem as the number of species increases. The numerical scheme which overcomes this challenge in Paper III is briefly summarized in this section, along with relevant literature review.

4.3.1 Summary of the publication

In our study of multi-species flows, we propose to reduce dimensionality of the eigensystem. Feasibility is based on the fact that the eigenmatrices composed of left and right eigenvectors, respectively, are sparse and non-zero entries in both matrices are mainly distributed along the diagonal. Moreover, the diagonal elements in the right-bottom part of both matrices, which accounts for the species mass convection, are unity. These conveniences can be ascribed to the fact that in the homogeneous multi-species gas mixture, all species are passively transported at a joint mixture velocity, independent of each other.

We take advantages of the structure of the eigenmatrices and propose a partial characteristic decomposition scheme for multi-species Euler equations. We split the eigensystem into two parts along the diagonal of eigenmatrix: one is the gas mixture part and the other part accounts for all the species. Correspondingly, the conserved vector of the total mixture mass, momenta and energy as well as species partial densities is divided into a gas mixture part and the remaining species partial density part. All the species follow a series of independent advection equations in a conservative form. Compared with classical characteristic decomposition schemes, the proposed split scheme utilizes characteristic decomposition for single-fluid Euler equations [37, 11] to handle the first gas mixture part. It allows to avoid the characteristic decomposition of the species part. Therefore, computational effort can be reduced significantly as no species transformation from physical space to characteristic space and back is needed. To cope with the inconsistency issue after decoupling the partial densities of species from the mixture total density, a species mass fraction correction is proposed.

4.3.2 Individual contributions of the candidate

My contribution to this work was the development of the method and the corresponding computer code for its implementation. I have performed simulations, analyzed the results, and written the manuscript for the publication.

Chapter 5

Discussion and outlooks

In this thesis, a series of numerical methods have been proposed to improve the computational efficiency of simulating compressible, chemically reacting flows with multiple species and nonequilibrium kinetics. Targeted at different parts of the reactive multi-species Euler equations, we have the following:

- A new operator splitting method is proposed for capturing stiff and nonstiff detonation waves, balancing numerical accuracy and computational efficiency.
- For the computationally expensive temporal integration of ordinary differential equation (ODE) system of chemical kinetics with detailed mechanisms, a species-clustered operator-splitting scheme is developed by using the idea of optimal partitioning.
- The remaining flow convective terms are considered by using a partial characteristic decomposition scheme to overcome the numerical challenge of quadratically increasing dimensionality of the convective flux eigensystem as the number of species grows in the classical high-order finite difference (FD) framework.

5.1 Discussion

Firstly, a new operator splitting method for simulating chemically reacting flows, especially for capturing stiff detonation waves in under-resolved conditions, has been developed. Two procedures based on operator splitting are included: for the convection step, any shock-capturing scheme can be used; for the reaction step, the multi-species multi-reaction ODE system in the source terms is further split in a reaction-by-reaction manner. Each reaction either proceeds a timestep forward or is interrupted according to a local random temperature rather than being a deterministic process with growing error accumulation. A wide range of numerical experiments including not only simple model kinetics but also realistic nonequilibrium chemistry such as the temperature-dependent finite-rate hydrogen-air combustion are considered in 1D and 2D flows, demonstrating the following properties:

- Mass conservation and positivity of species concentration can be guaranteed by the reaction-split ODE solver, which is almost unconditionally stable due to its using either analytical or approximate exact solutions.
- The proposed SPRANTS method can effectively predict the correct propagation of discontinuities as well as the overall flowfield information in under-resolved conditions, for both model kinetics and realistic finite-rate nonequilibrium kinetics.
- Compared with the deterministic method using CHEMEQ2, the present SPRANTS method exhibits better computational efficiency as it can correctly capture the detonation wave with a larger timestep on coarse grids for nonequilibrium reactive flows.
- By adding a drift term into the random temperature sampling, SPRANTS can recover the deterministic solution as the resolution improves with decreasing stiffness.
- The dimension-independent algorithm for the source terms makes further 3D extension of the proposed method straightforward.

Secondly, for large-scale chemical kinetics involving many species and reactions, computational efforts needed for time integration usually exceeds linear scaling with the dimension of the kinetic mechanism, especially when implicit ODE solvers are used. To achieve a higher computational efficiency, we have proposed operator splitting to integrate the large system in separate yet consecutive subsystems of the same and smaller dimension. Each subsystem includes a cluster of species decoupled from the other species of the full mechanism and is solved separately, e.g. implicitly by VODE. In order to reduce the inevitable splitting error, diffusion maps are applied to analyze the species graph and to cluster strongly coupled species into the same subsystem, by defining an appropriate weight matrix for chemical kinetics. Three hydrocarbon fuel/air ignition problems with an increasing dimension of the mechanism, up to 2115 species and 8157 reactions, are taken into consideration under varying initial conditions. Computational efficiency and accuracy can be improved by choosing a proper number of clusters to split the large system. For the n-heptane mechanism, partition by 4 clusters of species leads to about 8 times speedup compared to the non-split VODE solver and $10 \sim 20$ times speedup versus the explicit solver CHEMEQ2. For the n-hexadecane mechanism, partition by 8 clusters of species results in a speedup factor of around 40. Clustering by diffusion maps based on a given weight matrix outperforms the simple clustering according to species' index in the mechanism, in terms of predicting the correct ignition delay time and post-ignition

equilibrium state. It implies that an optimal clustering for a certain mechanism is preferable not only for computational acceleration but also for higher accuracy.

Finally, we have presented a partial characteristic decomposition scheme for the solution of multi-species Euler equations with high-order finite difference schemes. Since the eigensystem of the multi-species convective flux Jacobian is sparse and non-zero entries in its matrices are mainly distributed along the diagonal, it is feasible to split the eigensystem into two parts: one is the gas mixture part, which is subject to traditional characteristic decomposition schemes for single-fluid Euler equations, and the other part corresponds to a series of species partial mass equations. Since the species part has a sub-eigensystem of which the left and right sub-eigenmatrices are diagonal identity matrices, transforming the species variables from physical space onto characteristic space and back is no longer necessary, so that massive operations on matrix multiplication that is computationally very expensive can be avoided. With extensive numerical examples, the proposed scheme manages to significantly reduce the computational cost for calculating the multi-species convective flux in the following two aspects:

- Computational cost of the full characteristic decomposition schemes depends super-linearly (quadratically even cubically) on the number of species involved.
- Similarly with the 2nd-order AUSM plus MUSCL scheme in the finite volume formulation, the linear scaling of the computational cost with different numbers of species is realized by the proposed decoupled scheme.

Despite the splitting error, since each decoupled part is still discretized by high-order schemes, the proposed scheme is verified to preserve the high-order accuracy of the underlying discretization scheme. The inconsistency issue in the update of species mass fractions has been resolved by summing up all the newly computed partial densities to reproduce a consistent nominal total density to be the base of renormalization. In contrast, using the straightforward update of mass fractions as the fully coupled scheme leads to spurious oscillations around discontinuities with large species gradients.

5.2 Outlooks

The main part of this thesis focuses on developing efficient numerical methods for the computation of multi-species reactive Euler equations with source terms, which are directly related with the compressible chemically reacting flows.

- *Realistic flow simulation in gasdynamics.* Diffusion process or viscosity can be straightforwardly added to the present system, discretized with classical

central-difference schemes. Given the complete system of Navier-Stokes equation, realistic gasdynamics with/without chemical reactions and multiple species can be solved in a consistent manner. Applications like reentry problems with boundary layers and air dissociation in a high-temperature condition, in addition to many internal flows with fuel/oxidizer combustion as in air-breathing propulsion systems [91, 92], can be considered.

- *Operator splitting for large-scale complex nonlinear processes.* It is readily to see that the core idea of operator splitting goes through my entire work of this thesis. One great advantage of the idea of operator splitting lies in that it can overcome the numerical difficulties of conventional methods encountered in large-scale systems such as numerical instability, negative solutions, and convergence issue [50]. It thus implies many potential applications involving large-scale dynamic processes encountered in physics, chemistry and biology. Noticeably, the two ODE solvers utilizing this idea in Paper I & II might be used for general ODE integrations including but not limited to nonequilibrium chemistry in combustion, reaction-diffusion in biological systems [93, 94], etc.

- *Vapor-liquid two-phase flows.* As previously mentioned, the current computational model with multiple species can be easily translated into a multicomponent two-phase model, if corresponding thermodynamical model is coupled instead of the current EoS of ideal gas mixtures. The vapor-liquid equilibrium (VLE) model [31, 32] can serve this purpose. As a result, the fuel injection process as well as its cavitation, atomization, evaporation and combustion in either liquid or gas state can be modeled and simulated in a unified framework. However, there still exists a fundamental issue with the computational efficiency and numerical stability of solving local VLE problems over a wide range of states of pressure, temperature and component compositions [95, 96, 97].

Bibliography

[1] Adam Connell/LLNL. *An artist's rendition of an internal combustion engine with fuel molecules.* 2018. URL: https://www.llnl.gov/news/lab-scientists-optimizing-high-performance-fuels-advanced-internal-combustion-engines (visited on 06/21/2019).

[2] William M. Humphreys. *Components of a typical propulsion-airframe integrated dual-mode scramjet and features of the associated internal flow.* 2018. URL: https://www.researchgate.net/figure/Components-of-a-typical-propulsion-airframe-integrated-dual-mode-scramjet-and-features-of_fig1_279500205 (visited on 06/21/2019).

[3] Joseph H. Jones. *Rocket engine diagrams.* 2018. URL: https://faculty.ung.edu/jjones/astr1010home/rockets.htm (visited on 06/21/2019).

[4] Eleuterio F Toro. *Riemann solvers and numerical methods for fluid dynamics: a practical introduction.* Springer Science & Business Media, 2013.

[5] Robert Eymard, Thierry Gallouët, and Raphaèle Herbin. "Finite volume methods". In: *Handbook of numerical analysis* 7 (2000), pp. 713–1018.

[6] Randall J LeVeque. *Finite volume methods for hyperbolic problems.* Vol. 31. Cambridge university press, 2002.

[7] Meng-Sing Liou. "A sequel to ausm: Ausm+". In: *Journal of Computational Physics* 129.2 (1996), pp. 364–382.

[8] Meng-Sing Liou. "A sequel to AUSM, Part II: AUSM+-up for all speeds". In: *Journal of computational physics* 214.1 (2006), pp. 137–170.

[9] Vladimir A Titarev and Eleuterio F Toro. "Finite-volume WENO schemes for three-dimensional conservation laws". In: *Journal of Computational Physics* 201.1 (2004), pp. 238–260.

[10] Chi-Wang Shu. "High order ENO and WENO schemes for computational fluid dynamics". In: *High-order methods for computational physics.* Springer, 1999, pp. 439–582.

[11] Chi-Wang Shu. "Essentially non-oscillatory and weighted essentially non-oscillatory schemes for hyperbolic conservation laws". In: *Advanced numerical approximation of nonlinear hyperbolic equations.* Springer, 1998, pp. 325–432.

[12] Nelida Črnjarić-Žic, S Vuković, and Luka Sopta. "On different flux splittings and flux functions in WENO schemes for balance laws". In: *Computers & fluids* 35.10 (2006), pp. 1074–1092.

[13] TR Young Jr. *CHEMEQ-A subroutine for solving stiff ordinary differential equations*. Tech. rep. NAVAL RESEARCH LAB WASHINGTON DC, 1980.

[14] David R Mott and Elaine S Oran. *CHEMEQ2: A solver for the stiff ordinary differential equations of chemical kinetics*. Tech. rep. NAVAL RESEARCH LAB WASHINGTON DC, 2001.

[15] Yang Gao et al. "A dynamic adaptive method for hybrid integration of stiff chemistry". In: *Combustion and Flame* 162.2 (2015), pp. 287–295.

[16] Youhi Morii et al. "ERENA: A fast and robust Jacobian-free integration method for ordinary differential equations of chemical kinetics". In: *Journal of Computational Physics* 322 (2016), pp. 547–558.

[17] Peter N Brown, George D Byrne, and Alan C Hindmarsh. "VODE: A variable-coefficient ODE solver". In: *SIAM Journal on Scientific and Statistical Computing* 10.5 (1989), pp. 1038–1051.

[18] Makis Caracotsios and Warren E. Stewart. "Sensitivity analysis of initial value problems with mixed odes and algebraic equations". In: *Computers & Chemical Engineering* 9.4 (1985), pp. 359 –365. ISSN: 0098-1354. DOI: https://doi.org/10.1016/0098-1354(85)85014-6. URL: http://www.sciencedirect.com/science/article/pii/0098135485850146.

[19] PETER E Van Keken, David A Yuen, and Linda R Petzold. "DASPK: a new high order and adaptive time-integration technique with applications to mantle convection with strongly temperature-and pressure-dependent rheology". In: *Geophysical & Astrophysical Fluid Dynamics* 80.1-2 (1995), pp. 57–74.

[20] Gerhard Wanner and Ernst Hairer. *Solving ordinary differential equations II*. Springer Berlin Heidelberg, 1996.

[21] Weizhu Bao and Shi Jin. "The random projection method for hyperbolic conservation laws with stiff reaction terms". In: *Journal of Computational Physics* 163.1 (2000), pp. 216–248.

[22] Weizhu Bao and Shi Jin. "The random projection method for stiff detonation capturing". In: *SIAM Journal on Scientific Computing* 23.3 (2001), pp. 1000–1026.

[23] Weizhu Bao and Shi Jin. "The random projection method for stiff multispecies detonation capturing". In: *Journal of Computational Physics* 178.1 (2002), pp. 37–57.

[24] Helen C Yee et al. "Spurious behavior of shock-capturing methods by the fractional step approach: Problems containing stiff source terms and discontinuities". In: *Journal of Computational Physics* 241 (2013), pp. 266–291.

[25] Phillip Colella, Andrew Majda, and Victor Roytburd. "Theoretical and numerical structure for reacting shock waves". In: *SIAM Journal on Scientific and Statistical Computing* 7.4 (1986), pp. 1059–1080.

[26] Randall J LeVeque and Helen C Yee. "A study of numerical methods for hyperbolic conservation laws with stiff source terms". In: *Journal of Computational Physics* 86.1 (1990), pp. 187–210.

[27] Bin Zhang et al. "The equilibrium state method for hyperbolic conservation laws with stiff reaction terms". In: *Journal of Computational Physics* 263 (2014), pp. 151–176.

[28] Jian-Hang Wang et al. "A split random time-stepping method for stiff and nonstiff detonation capturing". In: *Combustion and Flame* 204 (2019), pp. 397–413.

[29] Jian-Hang Wang et al. "A species-clustered splitting scheme for the integration of large-scale chemical kinetics using detailed mechanisms". In: *Combustion and Flame* 205 (2019), pp. 41–54.

[30] Jian-Hang Wang et al. "Partial characteristic decomposition for multi-species Euler equations". In: *Computers & Fluids* 181 (2019), pp. 364–382.

[31] Ping Yi et al. "A multicomponent real-fluid fully compressible four-equation model for two-phase flow with phase change". In: *Physics of Fluids* 31.2 (2019), p. 026102.

[32] Jan Matheis and Stefan Hickel. "Multi-component vapor-liquid equilibrium model for LES of high-pressure fuel injection and application to ECN Spray A". In: *International Journal of Multiphase Flow* 99 (2018), pp. 294–311.

[33] Robert I McLachlan and G Reinout W Quispel. "Splitting methods". In: *Acta Numerica* 11 (2002), pp. 341–434.

[34] Gilbert Strang. "On the construction and comparison of difference schemes". In: *SIAM Journal on Numerical Analysis* 5.3 (1968), pp. 506–517.

[35] Bram Van Leer. "Towards the ultimate conservative difference scheme. V. A second-order sequel to Godunov's method". In: *Journal of computational Physics* 32.1 (1979), pp. 101–136.

[36] Xiaolong Gou et al. "A dynamic multi-timescale method for combustion modeling with detailed and reduced chemical kinetic mechanisms". In: *Combustion and Flame* 157.6 (2010), pp. 1111–1121.

[37] Philip L Roe. "Approximate Riemann solvers, parameter vectors, and difference schemes". In: *Journal of computational physics* 43.2 (1981), pp. 357–372.

[38] Paul Glaister. "An approximate linearised Riemann solver for the Euler equations for real gases". In: *Journal of Computational Physics* 74.2 (1988), pp. 382–408.

[39] XY Hu, NA Adams, and Gianluca Iaccarino. "On the HLLC Riemann solver for interface interaction in compressible multi-fluid flow". In: *Journal of Computational Physics* 228.17 (2009), pp. 6572–6589.

[40] Jian-Shun Shuen, Meng-Sing Liou, and Bram Van Leer. "Inviscid flux-splitting algorithms for real gases with non-equilibrium chemistry". In: *Journal of Computational Physics* 90.2 (1990), pp. 371–395.

[41] Guang-Shan Jiang and Chi-Wang Shu. "Efficient implementation of weighted ENO schemes". In: *Journal of Computational Physics* 126.1 (1996), pp. 202–228.

[42] Felix Diegelmann, Stefan Hickel, and Nikolaus A Adams. "Three-dimensional reacting shock–bubble interaction". In: *Combustion and Flame* 181 (2017), pp. 300–314.

[43] Robert J Kee et al. *CHEMKIN-III: A FORTRAN chemical kinetics package for the analysis of gas-phase chemical and plasma kinetics*. Tech. rep. Sandia National Labs., Livermore, CA (United States), 1996.

[44] Bonnie J McBride, Sanford Gordon, and Martin A Reno. "Coefficients for calculating thermodynamic and transport properties of individual species". In: (1993).

[45] Mikko I Malinen and Pasi Fränti. "Balanced k-means for clustering". In: *Joint IAPR International Workshops on Statistical Techniques in Pattern Recognition (SPR) and Structural and Syntactic Pattern Recognition (SSPR)*. Springer. 2014, pp. 32–41.

[46] Chao Xu et al. "A sparse stiff chemistry solver based on dynamic adaptive integration for efficient combustion simulations". In: *Combustion and Flame* 172 (2016), pp. 183–193.

[47] Federico Perini, Emanuele Galligani, and Rolf D Reitz. "A study of direct and Krylov iterative sparse solver techniques to approach linear scaling of the integration of chemical kinetics with detailed combustion mechanisms". In: *Combustion and Flame* 161.5 (2014), pp. 1180–1195.

[48] Douglas A Schwer et al. "On upgrading the numerics in combustion chemistry codes". In: *Combustion and Flame* 128.3 (2002), pp. 270–291.

[49] Valeriu Damian et al. "The kinetic preprocessor KPP-a software environment for solving chemical kinetics". In: *Computers & Chemical Engineering* 26.11 (2002), pp. 1567–1579.

[50] Shucheng Pan et al. "A network partition method for solving large-scale complex nonlinear processes". In: *arXiv preprint arXiv:1801.06207* (2018).

[51] M Domijan. "What are... some graphs of chemical reaction networks?" In: (2008).

[52] MATLAB. *version 9.1.0.441655 (R2016b)*. Natick, Massachusetts: The MathWorks Inc., 2016.

[53] Ronald R Coifman et al. "Geometric diffusions as a tool for harmonic analysis and structure definition of data: Diffusion maps". In: *Proceedings of the National Academy of Sciences of the United States of America* 102.21 (2005), pp. 7426–7431.

[54] Ronald R Coifman and Stéphane Lafon. "Diffusion maps". In: *Applied and computational harmonic analysis* 21.1 (2006), pp. 5–30.

[55] Stephane Lafon and Ann B Lee. "Diffusion maps and coarse-graining: A unified framework for dimensionality reduction, graph partitioning, and data set parameterization". In: *IEEE transactions on pattern analysis and machine intelligence* 28.9 (2006), pp. 1393–1403.

[56] Jian-Hang Wang et al. "A Split Random Time Stepping Method for Stiff and Non-stiff Chemically Reacting Flows". In: *arXiv preprint arXiv:1802.04116* (2018).

[57] Khoi Nguyen, Alexandre Caboussat, and Donald Dabdub. "Mass conservative, positive definite integrator for atmospheric chemical dynamics". In: *Atmospheric Environment* 43.40 (2009), pp. 6287–6295.

[58] Michael A Gibson and Jehoshua Bruck. "Efficient exact stochastic simulation of chemical systems with many species and many channels". In: *The journal of physical chemistry A* 104.9 (2000), pp. 1876–1889.

[59] Laurent O Jay et al. "Improved quasi-steady-state-approximation methods for atmospheric chemistry integration". In: *SIAM Journal on Scientific Computing* 18.1 (1997), pp. 182–202.

[60] Jan G Verwer and D Simpson. "Explicit methods for stiff ODEs from atmospheric chemistry". In: *Applied Numerical Mathematics* 18.1-3 (1995), pp. 413–430.

[61] Chi-Wang Shu and Stanley Osher. "Efficient implementation of essentially non-oscillatory shock-capturing schemes". In: *Journal of computational physics* 77.2 (1988), pp. 439–471.

[62] Xi Deng et al. “A new shock-capturing scheme for stiff detonation waves problems”. In: *arXiv preprint arXiv:1708.01000* (2017).

[63] Duc Nguyen, Frédéric Gibou, and Ronald Fedkiw. “A fully conservative ghost fluid method and stiff detonation waves”. In: *12th Int. Detonation Symposium, San Diego, CA*. 2002.

[64] Anne Bourlioux, Andrew J Majda, and Victor Roytburd. “Theoretical and numerical structure for unstable one-dimensional detonations”. In: *SIAM Journal on Applied Mathematics* 51.2 (1991), pp. 303–343.

[65] Anne Bourlioux and Andrew J Majda. “Theoretical and numerical structure for unstable two-dimensional detonations”. In: *Combustion and Flame* 90.3-4 (1992), pp. 211–229.

[66] Rolf Jeltsch and Petra Klingenstein. “Error estimators for the position of discontinuities in hyperbolic conservation laws with source terms which are solved using operator splitting”. In: *Computing and Visualization in Science* 1.4 (1999), pp. 231–249.

[67] Barna L Bihari and Donald Schwendeman. “Multiresolution schemes for the reactive Euler equations”. In: *Journal of Computational Physics* 154.1 (1999), pp. 197–230.

[68] Björn Engquist and Björn Sjögreen. *Robust difference approximations of stiff inviscid detonation waves*. Department of Mathematics, University of California, Los Angeles, 1991.

[69] AC Berkenbosch, EF Kaasschieter, and R Klein. “Detonation capturing for stiff combustion chemistry”. In: *Combustion Theory and Modelling* 2.3 (1998), pp. 313–348.

[70] Christiane Helzel, Randall J Leveque, and Gerald Warnecke. “A modified fractional step method for the accurate approximation of detonation waves”. In: *SIAM Journal on Scientific Computing* 22.4 (2000), pp. 1489–1510.

[71] Luca Tosatto and Luigi Vigevano. “Numerical solution of under-resolved detonations”. In: *Journal of Computational Physics* 227.4 (2008), pp. 2317–2343.

[72] Wei Wang et al. “High order finite difference methods with subcell resolution for advection equations with stiff source terms”. In: *Journal of Computational Physics* 231.1 (2012), pp. 190–214.

[73] Wei Wang et al. “High order finite difference methods with subcell resolution for stiff multispecies discontinuity capturing”. In: *Communications in Computational Physics* 17.2 (2015), pp. 317–336.

[74] Dmitry V Kotov et al. "Computational challenges for simulations related to the NASA electric arc shock tube (EAST) experiments". In: *Journal of Computational Physics* 269 (2014), pp. 215–233.

[75] Ismail E. Mersin et al. "Hexadecane mechanisms: Comparison of hand-generated and automatically generated with pathways". In: *Fuel* 115 (2014), pp. 132 – 144. ISSN: 0016-2361. DOI: https://doi.org/10.1016/j.fuel.2013.06.055. URL: http://www.sciencedirect.com/science/article/pii/S0016236113005966.

[76] Olivier Herbinet, William J Pitz, and Charles K Westbrook. "Detailed chemical kinetic oxidation mechanism for a biodiesel surrogate". In: *Combustion and Flame* 154.3 (2008), pp. 507–528.

[77] Tianfeng Lu and Chung K. Law. "Toward accommodating realistic fuel chemistry in large-scale computations". In: *Progress in Energy and Combustion Science* 35.2 (2009), pp. 192 –215. ISSN: 0360-1285. DOI: https://doi.org/10.1016/j.pecs.2008.10.002. URL: http://www.sciencedirect.com/science/article/pii/S036012850800066X.

[78] Tianfeng Lu and Chung K Law. "A directed relation graph method for mechanism reduction". In: *Proceedings of the Combustion Institute* 30.1 (2005), pp. 1333–1341.

[79] P. Pepiot-Desjardins and H. Pitsch. "An efficient error-propagation-based reduction method for large chemical kinetic mechanisms". In: *Combustion and Flame* 154.1 (2008), pp. 67 –81. ISSN: 0010-2180. DOI: https://doi.org/10.1016/j.combustflame.2007.10.020. URL: http://www.sciencedirect.com/science/article/pii/S0010218007003264.

[80] Wenting Sun et al. "A path flux analysis method for the reduction of detailed chemical kinetic mechanisms". In: *Combustion and Flame* 157.7 (2010), pp. 1298 –1307. ISSN: 0010-2180. DOI: https://doi.org/10.1016/j.combustflame.2010.03.006. URL: http://www.sciencedirect.com/science/article/pii/S0010218010000842.

[81] Kyle E. Niemeyer, Chih-Jen Sung, and Mandhapati P. Raju. "Skeletal mechanism generation for surrogate fuels using directed relation graph with error propagation and sensitivity analysis". In: *Combustion and Flame* 157.9 (2010), pp. 1760 –1770. ISSN: 0010-2180. DOI: https://doi.org/10.1016/j.combustflame.2009.12.022. URL: http://www.sciencedirect.com/science/article/pii/S0010218010000039.

[82] Zhuyin Ren et al. "Dynamic adaptive chemistry with operator splitting schemes for reactive flow simulations". In: *Journal of Computational Physics* 263 (2014), pp. 19–36.

[83] MA Singer and SB Pope. "Exploiting ISAT to solve the reaction-diffusion equation". In: *Combustion theory and modelling* 8.2 (2004), pp. 361–383.

[84] MA Singer, SB Pope, and HN Najm. "Operator-splitting with ISAT to model reacting flow with detailed chemistry". In: *Combustion Theory and Modelling* 10.2 (2006), pp. 199–217.

[85] Omar M Knio, Habib N Najm, and Peter S Wyckoff. "A semi-implicit numerical scheme for reacting flow: II. Stiff, operator-split formulation". In: *Journal of Computational Physics* 154.2 (1999), pp. 428–467.

[86] Zhuyin Ren and Stephen B Pope. "Second-order splitting schemes for a class of reactive systems". In: *Journal of Computational Physics* 227.17 (2008), pp. 8165–8176.

[87] Ronald P Fedkiw, Barry Merriman, and Stanley Osher. "High accuracy numerical methods for thermally perfect gas flows with chemistry". In: *Journal of Computational Physics* 132.2 (1997), pp. 175–190.

[88] Jack L Ziegler et al. "An adaptive high-order hybrid scheme for compressive, viscous flows with detailed chemistry". In: *Journal of Computational Physics* 230.20 (2011), pp. 7598–7630.

[89] Arnab Chaudhuri et al. "Numerical study of compressible mixing layers using high-order WENO schemes". In: *Journal of Scientific Computing* 47.2 (2011), pp. 170–197.

[90] Pedro José Martínez Ferrer et al. "A detailed verification procedure for compressible reactive multicomponent Navier–Stokes solvers". In: *Computers & Fluids* 89 (2014), pp. 88–110.

[91] Frank K Lu and Eric M Braun. "Rotating detonation wave propulsion: experimental challenges, modeling, and engine concepts". In: *Journal of Propulsion and Power* 30.5 (2014), pp. 1125–1142.

[92] Edward T Curran. "Scramjet engines: the first forty years". In: *Journal of Propulsion and Power* 17.6 (2001), pp. 1138–1148.

[93] Duygu Balcan et al. "Multiscale mobility networks and the spatial spreading of infectious diseases". In: *Proceedings of the National Academy of Sciences* 106.51 (2009), pp. 21484–21489.

[94] Jean-Christophe Rain et al. "The protein–protein interaction map of Helicobacter pylori". In: *Nature* 409.6817 (2001), p. 211.

[95] Michael L Michelsen. "The isothermal flash problem. Part I. Stability". In: *Fluid phase equilibria* 9.1 (1982), pp. 1–19.

[96] Michael L Michelsen. "The isothermal flash problem. Part II. Phase-split calculation". In: *Fluid phase equilibria* 9.1 (1982), pp. 21–40.

[97] Marcelo Castier. “Solution of the isochoric–isoenergetic flash problem by direct entropy maximization”. In: *Fluid Phase Equilibria* 276.1 (2009), pp. 7–17.

Appendix A

List of publications

A.1 Peer-reviewed journal papers

- JH Wang, S Pan, XY Hu, NA Adams, A split random time-stepping method for stiffand nonstiff detonation capturing, *Combustion and Flame*, **204**, 397–413, 2019.
- JH Wang, S Pan, XY Hu, NA Adams, A species-clustered splitting scheme for the integration of large-scale chemical kinetics using detailed mechanisms, *Combustion and Flame*, **205**, 41-54, 2019.
- JH Wang, S Pan, XY Hu, NA Adams, Partial characteristic decomposition for multi-species Euler equations, *Computers and Fluids*, **181**, 364–382, 2019.

A.2 Conferences

- JH Wang, SZ Yang, Chaouki Habchi, Xiangyu Hu, Nikolaus A. Adams, "A multi-component real-fluid two-phase flow solver with high-order finite-difference schemes", 29th European Conference on Liquid Atomization and Spray Systems, Sep 2-4 2019, Paris, France.
- JH Wang, Xiangyu Hu, Nikolaus A. Adams, "Species-clustered ODE solver for large-scale chemical kinectics", GAMM 2018, 89th GAMM Annual Meeting, Munich, Germany.
- JH Wang, Xiangyu Hu, Nikolaus A. Adams, "Surfactant effects on surface tension using a multi-resolution conservative level-set based sharp-interface method", 5th Cavitation Workshop, June 27-28 2017, Chania, Greece.

Appendix B

Original journal papers

Here, the peer-reviewed journal publications of the present work are attached.

B.1 Paper I

Jianhang Wang, Shucheng Pan, Xiangyu Y. Hu, Nikolaus A. Adams

A split random time-stepping method for stiff and nonstiff detonation capturing

In *Combustion and Flame*, Volume 204, 2019, pp. 397-413, DOI: `https://doi.org/10.1016/j.combustflame.2019.03.034`.

Contribution: My contribution to this work was the development of the method and the corresponding computer code for its implementation. I performed simulations and analyzed the results, and wrote the manuscript for the publication.

Combustion and Flame 204 (2019) 397–413

Contents lists available at ScienceDirect

Combustion and Flame

journal homepage: www.elsevier.com/locate/combustflame

A split random time-stepping method for stiff and nonstiff detonation capturing

Jian-Hang Wang, Shucheng Pan*, Xiangyu Y. Hu*, Nikolaus A. Adams

Chair of Aerodynamics and Fluid Mechanics, Department of Mechanical Engineering, Technical University of Munich, Garching 85748, Germany

ARTICLE INFO

Article history:
Received 28 May 2018
Revised 30 January 2019
Accepted 22 March 2019

Keywords:
Chemically reacting flows
Stiff source terms
Nonequilibrium kinetics
Operator splitting
Wrong propagation speed of discontinuities

ABSTRACT

In this paper, a new operator splitting method is proposed for capturing stiff and nonstiff detonation waves. In stiff cases, an incorrect propagation of discontinuities might be observed for general shock-capturing methods due to under-resolution in space and time. Previous random projection methods have been applied successfully for stiff detonation capturing at under-resolved conditions. Not relying on random projection of the intermediate state onto two presumed equilibrium states (completely burnt or unburnt) as with the random projection method, the present approach randomly advances or interrupts the reaction process. Each one-way reaction is decoupled from the multi-reaction kinetics by operator splitting. The local temperature is compared with a random temperature within a temperature interval to control the random reaction. Random activation or deactivation in the reaction step serves to reduce the accumulated error of discontinuity propagation. Extensive numerical experiments demonstrate the effectiveness and robustness of the method. For nonstiff problems, the proposed random method recovers the accuracy of general operator splitting methods by adding a drift term.

1. Introduction

One of the main challenges for numerical computation of chemically reacting flows are widely varying time scales of chemical kinetics, which may be orders of magnitude faster than the fluid flow time scale [1–3]. Such cases exhibit numerical stiffness due to the source terms representing chemical reactions [4]. When the chemical scales are not resolved numerically in time and space, a spurious solution may occur exhibiting incorrect propagation of discontinuities and nonphysical states.

This problem is well-known and has been an active area of research during the past three decades. It was first observed by Colella et al. [5] and by analysis of a scalar problem. LeVeque and Yee [6] found that the propagation error is mainly due to numerical dissipation contained in the scheme, which smears the discontinuity front and activates the source term in a nonphysical manner. To overcome this difficulty, one may reduce numerical dissipation [3,7,8] or use a sufficiently fine mesh. Front-tracking approaches [9–11] or local grid/timestep refinement [12,13] may obtain the correct propagation of the reactive front. However, generally full resolution of all fine scales cannot always be afforded. Since numerical dissipation is practically inevitable, another approach focuses on establishing corrected temperatures from the artificially diffused solution [14–16]. Tosatto and Vigevano [17] proposed a threshold method based on a variable reconstruction within bounds determined from the local cell neighbors. Difficulties with such methods are encountered in the extension to either spatially high-dimensional or multi-species/multi-reaction kinetics based reacting flows. Wang et al. [18,19] proposed a high-order finite-difference method utilizing the Harten ENO subcell resolution method for stiff source terms. In [4], many different methods with or without operator splitting/subcell resolution/nonlinear filters are tested, showing that the degree of propagation speed mismatch of discontinuities is highly dependent on the accuracy of the numerical method, time step and grid spacing. Kotov et al. [20] further presented a realistic hypersonic non-equilibrium flow that mimics the spurious behavior and some important numerical challenges affecting the accuracy in such simulations. Zhang et al. [7] proposed the equilibrium state method where the cell average is replaced by a local two-equilibrium-state reconstruction, making its extension to high dimensions straightforward. They also extended the method to multi-reaction systems by treating the two one-way reactions independently. Methods applicable for realistic nonequilibrium chemical kinetics with multiple finite-rate reversible reactions, to our best knowledge, have not been reported in literature so far.

Bao and Jin [1–3] introduced a random projection method for the reaction step by replacing the ignition temperature with a

* Corresponding authors.
E-mail addresses: jianhang.wang@tum.de (J.-H. Wang), shucheng.pan@tum.de (S. Pan), xiangyu.hu@tum.de (X.Y. Hu), nikolaus.adams@tum.de (N.A. Adams).

https://doi.org/10.1016/j.combustflame.2019.03.034
0010-2180/

uniformly distributed random variable. Although the random projection method cannot avoid the introduction of numerical dissipation by shock-capturing schemes, it can eliminate its effect. The method was established for scalar problems and successfully applied to model problems of 1D/2D reactive Euler equations. With the presumption of two time-independent equilibrium states of totally burnt and unburnt gases (regardless of the detailed reaction process), the method is only suitable for under-resolved stiff cases.

In this paper, we develop a split random time-stepping method for chemically reacting flows with general nonequilibrium chemistry in a unified manner, regardless of stiff or nonstiff source terms and under- or well-resolved conditions in space and time. Unlike Bao and Jin's random projection method, the activation and deactivation of chemical reactions in the reaction step is not projected onto two prescribed equilibrium states, but onto two time-dependent states corresponding to advancing the reaction by one timestep forward and interrupting the reaction, respectively. The criterion to activate a reaction follows from comparison of the local computed temperature with a randomized temperature depending on the states of the forward step and its adjoint. To randomize each reaction process, the multi-reaction system is split reaction by reaction [21,22]. By adding a drift term into the random temperature sampling, the proposed method recovers the solution of a deterministic fractional step method in nonstiff cases with increasing resolution.

The paper is organized as follows. In Section 2, we introduce the reactive Euler equations with chemical reaction source terms. A standard fractional step method is outlined by operator splitting into the convection step and reaction step. In the reaction step, a reaction-split ODE solver is developed to approximate the exact solution for general chemical kinetics, based on which random time-stepping of each reaction is performed. In Section 3, we examine the pure ODE solver and the split random time-stepping method by extensive model examples and realistic reacting flows in both 1D and 2D. Conclusions are drawn in the last section. More information about the ODE solver are provided in the appendix.

2. Formulation

Assuming the flow is compressible, inviscid and in two dimensions for simplicity, the multi-species Euler equations coupled with reaction source terms take the form

$$U_t + F(U)_x + G(U)_y = S(U), \tag{1}$$

where

$$\begin{aligned} U &= \left(\rho, \rho u, \rho v, \rho e_t, \rho y_1, \rho y_2, \ldots, \rho y_{N_s-1}\right)^T, \\ F(U) &= \left(\rho u, \rho u^2 + p, \rho uv, (\rho e_t + p)u, \rho u y_1, \rho u y_2, \ldots, \rho u y_{N_s-1}\right)^T, \\ G(U) &= \left(\rho v, \rho uv, \rho v^2 + p, (\rho e_t + p)v, \rho v y_1, \rho v y_2, \ldots, \rho v y_{N_s-1}\right)^T, \\ S(U) &= \left(0, 0, 0, 0, \dot{\omega}_1, \dot{\omega}_2, \ldots, \dot{\omega_{N_s-1}}^T\right) \end{aligned} \tag{2}$$

are vectors of the conserved variables, convective flux in the x- or y-direction and source terms, respectively, with $\dot{\omega}_i$ representing rate of change of the ith species concentration in the reactive gas mixture due to the chemical kinetics consisting of N_r reactions and N_s species. Furthermore, $e_t = e + \frac{1}{2}(u^2 + v^2)$ is the specific total energy including the specific internal energy e. To close the system, an equation of state (EoS) of the form

$$p = \rho \sum_{i=1}^{N_s} y_i \frac{R_u}{W_i} T \tag{3}$$

is used, with y_i and W_i denoting the mass fraction and molecular weight of the ith species, respectively, and R_u being the universal gas constant.

The above conservation laws of mass, momentums and energy with source terms are usually solved by operator splitting. The first step is flow convection

$$S_c: \quad U_t + F(U)_x + G(U)_y = 0 \tag{4}$$

assuming no chemical reactions and passive transport of all species. The second step solves the system of ODEs of chemical kinetics

$$S_r: \quad \frac{dy_i}{dt} = \frac{\dot{\omega}_i}{\rho}, \quad i = 1, \ldots, N_s, \tag{5}$$

under adiabatic and constant-volume conditions with fixed total density and constant specific internal energy. The first-order accurate Lie–Trotter splitting scheme [23] or the second-order Strang splitting [24] can be employed to approximate the solution from the discrete time level n to $n+1$ with a timestep Δt, i.e.

$$U^{n+1} = S_r^{(\Delta t)} \circ S_c^{(\Delta t)} U^n \quad \text{or} \quad U^{n+1} = S_c^{(\frac{\Delta t}{2})} \circ S_r^{(\Delta t)} \circ S_c^{(\frac{\Delta t}{2})} U^n, \tag{6}$$

with symbol '$\circ$' to separate each operator and to indicate that an operator is applied to the following arguments. For the convection operator S_c, a shock-capturing scheme [25–28] can be adopted. For the reaction step S_r, an ODE solver such as VODE [29], CHEMEQ2 [30] and MTS/HMTS [31] can be used with or without adaptive error control.

We first utilize operator splitting upon the nonequilibrium chemical kinetics so that a multi-reaction system can be decoupled into a series of single reaction steps. Then we introduce the established concept of random projection into the ODE solver in order to realize random ignition of reactions. Each reaction process is randomly advanced one timestep forward (activation) or interrupted (deactivation) instead of being projected onto two prescribed equilibrium states. In the following, we term the randomized and reaction-by-reaction ODE solver for nonequilibrium chemistry as Split Random Time-Stepping method (SPRANTS).

2.1. Split reaction-by-reaction ODE solver for chemical kinetics

For common nonequilibrium chemical kinetics, chemical production rates in Eq. (5) are derived from a reaction mechanism that consists of N_s species and N_r reactions

$$\sum_{i=1}^{N_s} \nu_{ji}^f X_i \Longleftrightarrow \sum_{i=1}^{N_s} \nu_{ji}^b X_i, \quad j = 1, \ldots, N_r, \tag{7}$$

where ν_{ji}^f and ν_{ji}^b are the stoichiometric coefficients of species i with description X_i appearing as a reactant and as a product in reaction j. The total production rate of species i in Eqs. (2) and (5) is the sum of the production rate from each single elementary reaction as

$$\dot{\omega}_i = W_i \sum_{j=1}^{N_r} \left(\nu_{ji}^b - \nu_{ji}^f\right) \left[k_j^f \prod_{l=1}^{N_s} \left[\frac{\rho_l}{W_l}\right]^{\nu_{jl}^f} - k_j^b \prod_{l=1}^{N_s} \left[\frac{\rho_l}{W_l}\right]^{\nu_{jl}^b} \right], \tag{8}$$

with k_j^f and k_j^b denoting the forward and backward reaction rates of each chemical reaction, and $\rho_l = y_l \rho$.

By operator splitting [21,22], we can decouple the multi-reaction system, e.g., by Lie–Trotter splitting, as

$$S_r: \quad R_{1st}^{(\Delta t)} = R_{N_r}^{(\Delta t)} \circ R_{N_r-1}^{(\Delta t)} \circ \cdots \circ R_2^{(\Delta t)} \circ R_1^{(\Delta t)}, \tag{9}$$

where the operator R_j corresponds to a single reaction j and is independent of all other reactions. The reaction-by-reaction idea resembles a meso-scale model of microscopic kinetics where one molecule/atom can only experience one reaction at a time instance. This is also the case with stochastic simulation of chemical kinetics [32]. At macroscopic scale, reactions involving large numbers of

species molecules/atoms are considered as simultaneously occurring processes. In [21] the second-order accurate Strang splitting is adopted, starting with the fastest reaction and ending with the slowest for half a timestep and then backwards for another half timestep. In our approach we simply take the traversal order not according to reaction rates but to the reaction-mechanism index sequence

$$S_r: \quad R_{2nd}^{(\Delta t)} = R_1^{(\frac{\Delta t}{2})} \circ R_2^{(\frac{\Delta t}{2})} \circ \cdots \circ R_{N_r}^{(\frac{\Delta t}{2})} \circ R_{N_r}^{(\frac{\Delta t}{2})} \circ R_{N_r-1}^{(\frac{\Delta t}{2})} \circ \cdots \circ R_1^{(\frac{\Delta t}{2})} = \overline{R_{1st}^{(\frac{\Delta t}{2})}} \circ R_{1st}^{(\frac{\Delta t}{2})}, \tag{10}$$

where $\overline{R_{1st}}$ is the reverse operator of R_{1st}. Accordingly, for each R_j, we have

$$R_j: \quad \sum_{i=1}^{N_s} \nu_{ji}^f X_i \Longleftrightarrow \sum_{i=1}^{N_s} \nu_{ji}^b X_i, \quad \frac{dy_i}{dt} = \frac{\dot{\omega}_i{}^j}{\rho}, \quad i = 1, \ldots, N_s,$$
$$\dot{\omega}_i{}^j = W_i\left(\nu_{ji}^b - \nu_{ji}^f\right)\left[k_j^f \prod_{l=1}^{N_s}\left[\frac{\rho_l}{W_l}\right]^{\nu_{jl}^f} - k_j^b \prod_{l=1}^{N_s}\left[\frac{\rho_l}{W_l}\right]^{\nu_{jl}^b}\right]. \tag{11}$$

We now rewrite the ODE in Eq. (11) in the following form [30]

$$\frac{dy_i}{dt} = q_i^j - p_i^j y_i, \quad i = 1, \ldots, N_s, \tag{12}$$

where $q_i^j \geq 0$ is the production rate and $p_i^j y_i \geq 0$ is the loss rate for the ith species through reaction j.

Following the operator splitting of reactions, we continue to split each reaction j into a forward reaction and a backward reaction (for an irreversible reaction, it can be interpreted as a reversible reaction with zero backward reaction rate)

$$R_j^{(\Delta t)} = R_{j,b}^{(\Delta t)} \circ R_{j,f}^{(\Delta t)} \tag{13}$$

such that the species involved will either gain mass or lose mass through the one-way forward/backward reaction from Eq. (12), i.e.

$$\text{mass gain}: q_i^j \geq 0,\ p_i^j y_i = 0 \text{ or mass loss}: q_i^j = 0,\ p_i^j y_i \geq 0, \tag{14}$$

with the simplified

$$q_i^{j,f} = \frac{W_i}{\rho}\nu_{ji}^b\left[k_j^f \prod_{l=1}^{N_s}\left[\frac{\rho_l}{W_l}\right]^{\nu_{jl}^f}\right],\ p_i^{j,f} y_i = 0 \quad \text{for product species},$$
$$q_i^{j,f} = 0,\ p_i^{j,f} y_i = \frac{W_i}{\rho}\nu_{ji}^f\left[k_j^f \prod_{l=1}^{N_s}\left[\frac{\rho_l}{W_l}\right]^{\nu_{jl}^f}\right] \quad \text{for reactant species} \tag{15}$$

for the forward reaction of Eq. (11). The backward reaction can be determined accordingly upon exchanging its reactants and products.

Since each elementary reaction is decoupled from the others and each reaction again is split into two opposite unidirectional reactions, finally only a single reaction equation of the type

$$aA + bB + \cdots \longrightarrow xX + yY + \cdots \tag{16}$$

is considered in each operation. Mass conservation and positivity of mass fractions can be properly treated.

For the simple cases of Eq. (16), one may find analytical solutions, see Appendix A. However, for the general form of Eq. (16) whose analytical solution is not explicitly known or difficult to derive, a more convenient alternative is to use quasi-steady-state (QSS) methods to obtain the approximate exact solution. QSS methods are based on the exact solution of Eq. (12) for constant p_i^j and q_i^j [33,34], i.e.

$$y_i^{n+1} = y_i^n e^{-p_i^j \Delta t} + \frac{q_i^j}{p_i^j}(1 - e^{-p_i^j \Delta t}), \quad \text{for all } \nu_{ji}^b - \nu_{ji}^f \neq 0. \tag{17}$$

As generally p_i^j and q_i^j depend on $\{y_1, \ldots, y_{N_s}\}$ in Eq. (14) or (15), Eq. (17) provides a linear approximation. For the QSS-based SPRANTS method, the stable timestep size is not limited to the characteristic time scales of the chemical species and thus a larger timestep implying less computational efforts is possible [21].

Remark 1. The QSS approximation adopted here in SPRANTS is first-order accurate. For application to reacting flows the achievably absolute error magnitude generally is sufficient [30].

2.1.1. Treatment for mass conservation

Employing QSS in Eq. (17) for all the species participating in reaction j (with $\nu_{ji}^b - \nu_{ji}^f \neq 0$),

$$\sum_i y_i^{n+1} = \sum_i \left(y_i^n e^{-p_i^j \Delta t} + \frac{q_i^j}{p_i^j}\left(1 - e^{-p_i^j \Delta t}\right)\right) \tag{18}$$

may not necessarily be unity so that mass may be not exactly conserved. To cure this problem, one may only advance y_k^n to y_k^{n+1} of a reactant k by Eq. (17) and update all other $\{y_{i,i=1,\ldots,N_s,i\neq k}\}^{n+1}$ by mass conservation of a single reaction equation in Eq. (11). This merit of knowing the exact net gain or loss of mass of other species originates from the fact that each reaction in Eq. (11) is decoupled from others. Therefore, for the reactant k, combining Eqs. (17) and (15) we have

$$y_k^{n+1} = y_k^n e^{-p_k^j \Delta t} \tag{19}$$

and for the other species $i \neq k$, including other reactants and all the products in reaction j, the change of mass fraction $\Delta y_i = y_i^{n+1} - y_i^n$ should obey

$$\frac{\Delta y_i / W_i}{\nu_{ji}^b - \nu_{ji}^f} = \frac{\Delta y_k / W_k}{\nu_{jk}^b - \nu_{jk}^f}, \tag{20}$$

giving the update

$$y_i^{n+1} = y_i^n + \Delta y_i = y_i^n + \frac{\nu_{ji}^b - \nu_{ji}^f}{\nu_{jk}^b - \nu_{jk}^f}\frac{W_i}{W_k}\Delta y_k. \tag{21}$$

It is easy to see that $\sum_{i=1}^{N_s} \Delta y_i = 0$, which is equivalent to $\sum_{i=1}^{N_s} y_i = 1$ for mass conservation.

2.1.2. Positivity-preserving treatment

Without loss of generality, we consider the forward reaction j and assume that reactant species k has $\nu_{jk}^b = 0$ in Eq. (19), as $\nu_{jk}^f > 0$ is prescribed for reactants. Similarly assuming that another reactant species i also has $\nu_{ji}^f > 0$ and $\nu_{ji}^b = 0$, we combine Eqs. (19) and (21) to obtain

$$y_i^{n+1} = y_i^n - \frac{\nu_{ji}^f}{\nu_{jk}^f}\frac{W_i}{W_k}y_k^n + \frac{\nu_{ji}^f}{\nu_{jk}^f}\frac{W_i}{W_k}y_k^n e^{-p_k^j \Delta t}. \tag{22}$$

Recalling Eq. (15) for reactants i and k, we have

$$\frac{p_i^j y_i}{p_k^j y_k} = \frac{\nu_{ji}^f}{\nu_{jk}^f}\frac{W_i}{W_k}. \tag{23}$$

Upon rearranging Eq. (23) and substitution into Eq. (22) we obtain

$$y_i^{n+1} = y_i^n \frac{p_k^j - p_i^j}{p_k^j} + \frac{\nu_{ji}^f}{\nu_{jk}^f}\frac{W_i}{W_k}y_k^n e^{-p_k^j \Delta t}. \tag{24}$$

Table 1
Convergence rates for S_1 and S_4 using Lie–Trotter and Strang splittings.

		S_1				S_4			
	Δt	L_1 error	Rate	L_∞ error	Rate	L_1 error	Rate	L_∞ error	Rate
Lie–Trotter	6.25E−03	3.47E−15	–	5.01E−15	–	1.47E−12	–	2.27E−12	–
	1.25E−02	7.30E−15	1.0709	1.05E−14	1.07166	2.94E−12	0.999772	4.53E−12	0.999815
	2.50E−02	1.60E−14	1.13228	2.32E−14	1.13699	5.89E−12	0.999544	9.07E−12	0.999631
	5.00E−02	3.76E−14	1.23291	5.51E−14	1.24985	1.18E−11	0.999088	1.81E−11	0.999261
	1.00E−01	9.76E−14	1.37647	1.47E−13	1.41746	2.35E−11	0.998174	3.62E−11	0.99852
Strang	6.25E−03	3.14E−17	–	1.00E−16	–	5.25E−17	–	8.32E−17	–
	1.25E−02	1.24E−16	1.97793	4.00E−16	1.99959	2.10E−16	1.99745	3.34E−16	2.00663
	2.50E−02	4.94E−16	1.99949	1.60E−15	2.0001	8.39E−16	1.99996	1.34E−15	2.00002
	5.00E−02	1.98E−15	2.00021	6.40E−15	1.99999	3.36E−15	1.99999	5.35E−15	1.9999
	1.00E−01	7.91E−15	1.99997	2.56E−14	2	1.34E−14	1.99999	2.14E−14	2

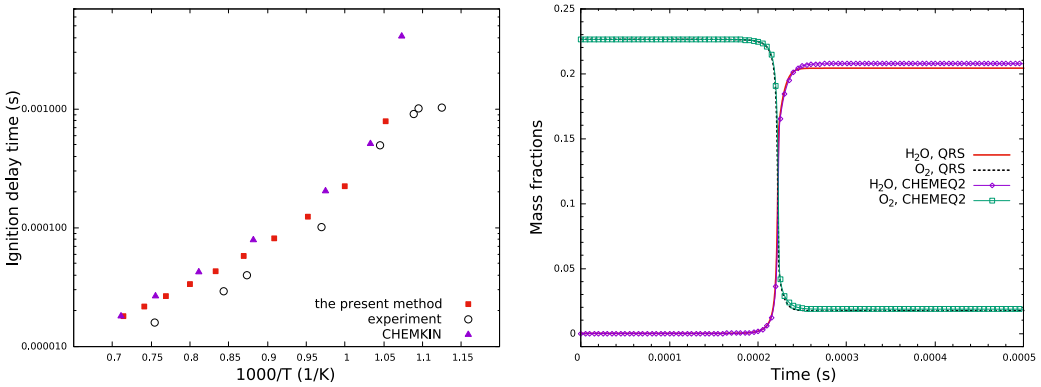

Fig. 1. Ignition delay times with different initial temperatures (left) and time histories of mass fractions of H and H_2O with $T_0 = 1000$ K (right).

With the aid of Eq. (24), it is readily seen that positivity of y_i^{n+1}, i.e. $y_i^{n+1} \geq 0$, is achieved when $p_k^j \geq p_i^j$ since the third term is always non-negative. Therefore, in order to preserve the positivity of species mass fractions, reactant species k using the QSS approximation should satisfy

$$p_k^j = max\{p_i^j\} \quad \text{for all the reactant species in reaction } j. \tag{25}$$

Regarding the positivity for the choosen reactant k, according to Eq. (19), it is inherently satisfied through positivity of the exponential function. Eq. (19) implies that $0 \leq y_k^{n+1} < 1$ due to the negative exponent such that mass fractions of all species through reaction j are bounded within [0,1] as a result of mass conservation.

Remark 2. The present reaction-split method using analytical or approximate solutions can perform sufficiently well, as a standalone solver, for the ODE system in chemical kinetics. Its following randomization is not motivated for integrating the ODE accurately, but primarily aimed at alleviating the effect of numerical dissipation introduced by S_c through shock-capturing schemes into S_r.

2.2. Finite randomization of chemical reactions

Bao and Jin [1–3] first proposed the idea of random projection into the ODE solver in place of the deterministic projection. They also proved that the random projection method gives first-order convergence for scalar problems. For scalar problems and Euler equations with stiff source terms, the random projection method shows excellent performance in obtaining correct shocks and reacting fronts for under-resolved spatial and temporal discretizations.

Through operation splitting of the ODE system in S_r, we merely need to consider the randomization of a single one-way reaction from time t_n to t_{n+1}. In Bao and Jin's formulation, temperature is randomized and compared with a pre-set ignition temperature, T_{ign}. Upper and lower temperature limits are needed, i.e. T_u and T_b (corresponding to the two equilibrium states of the initial combustible gas mixture being completely burnt and unburnt).

Here we advance the current state vector $\{y_1, \ldots, y_{N_s}\}$ through a single one-way reaction with subscript j, as in Eq. (16),

$$\{y_1, \ldots, y_{N_s}\}^+ = R_j^{(\Delta t)}\{y_1, \ldots, y_{N_s}\}, \tag{26}$$

where $\{y_1, \ldots, y_{N_s}\}^+$ represents the advance in time by operation R_j (for reversible reactions R_j^f or R_j^b). The change of mass fractions for the species involved in this reaction is

$$\{\Delta y_1, \ldots, \Delta y_{N_s}\}_j = \{y_1, \ldots, y_{N_s}\}^+ - \{y_1, \ldots, y_{N_s}\}. \tag{27}$$

The reverse operation from time level n is

$$\{y_1, \ldots, y_{N_s}\}^- = \{y_1, \ldots, y_{N_s}\} - \{\Delta y_1, \ldots, \Delta y_{N_s}\}_j. \tag{28}$$

Since mass fractions of species involved are constrained in [0,1], all mass fractions have to be rescaled if necessary according to Eq. (20). For the two states with superscripts + and −, two limit temperatures T^+ and T^- can be implicitly obtained according to Eq. (3) with the thermodynamic relation

$$h(y_1, \ldots, y_{N_s}, T) - e = \frac{p(y_1, \ldots, y_{N_s}, T)}{\rho}, \tag{29}$$

where ρ and e are fixed during a constant-volume adiabatic reaction and h represents the specific enthalpy. If we assume that the present reaction is exothermal, we have $T^- < T < T^+$. The converse applies to endothermal reactions. T^+ corresponds to T_b in the original random projection method while T^- corresponds to T_u. Given the two limit temperatures, we can assemble a local random temperature by

$$T^* = T^- + \theta_n(T^+ - T^-), \tag{30}$$

where θ_n is a uniformly distributed random real number between 0 and 1, and T^* is the randomized local temperature with $min\{T^-, T^+\} < T^* < max\{T^-, T^+\}$ and $T^* \neq T$ in general. Regarding

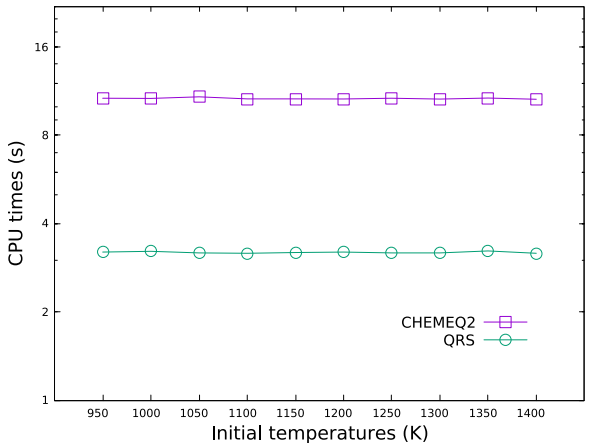

Fig. 2. CPU times with different initial temperatures.

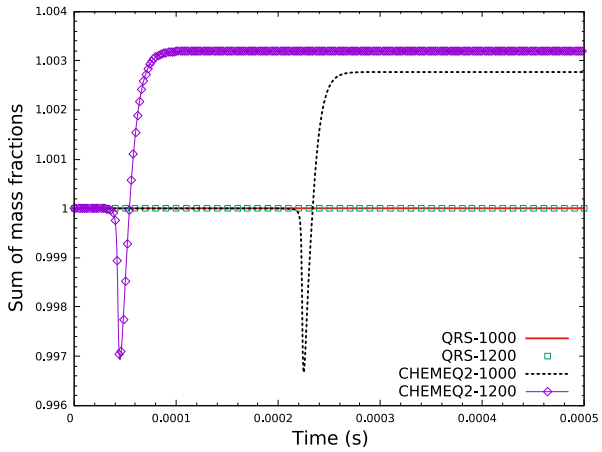

Fig. 3. Time histories of the sum of mass fractions with '1000': $T_0 = 1000$ K and '1200': $T_0 = 1200$ K.

the generation of random number θ_n, Bao and Jin suggested the van der Corput sampling scheme [35].

Given the random temperature T^*, the unidirectional reaction j is performed as

$$P_j^{(\Delta t)}: \quad \{y_1, \ldots, y_{N_s}\}_j = \begin{cases} \{y_1, \ldots, y_{N_s}\}^+, & \text{if } T > T^*, \\ \{y_1, \ldots, y_{N_s}\}, & \text{otherwise.} \end{cases} \tag{31}$$

The updated state solution $\{y_1, \ldots, y_{N_s}\}_j$ is taken as the initial state for the next reaction $j+1$.

Remark 3. As the random temperature T^* is uniformly distributed between the two temperature limits, the mean propagation of the reaction front recovers the physically correct position [1]. With deterministic ODE solvers, accumulation of errors may lead to non-physical reacting front propagation, see the detailed explanation in [7,36].

Inserting Eq. (31) into the split ODE solver in Eqs. (9) and (10), the present SPRANTS method can be written as

$$P_{1st}^{(\Delta t)} = P_{N_r}^{(\Delta t)} \circ P_{N_r-1}^{(\Delta t)} \circ \cdots \circ P_2^{(\Delta t)} \circ P_1^{(\Delta t)} \tag{32}$$

corresponding to the Lie–Trotter splitting or as

$$P_{2nd}^{(\Delta t)} = P_1^{(\frac{\Delta t}{2})} \circ P_2^{(\frac{\Delta t}{2})} \circ \cdots \circ P_{N_r}^{(\frac{\Delta t}{2})} \circ P_{N_r}^{(\frac{\Delta t}{2})} \circ P_{N_r-1}^{(\frac{\Delta t}{2})} \circ \cdots \circ P_1^{(\frac{\Delta t}{2})} \tag{33}$$

corresponding to Strang splitting.

Remark 4. Not requiring either the flow information at each cell and its neighbors [17] or an additional procedure to locate the reacting front in the computational domain [1], the proposed method solves the source terms at each cell locally as a 0D problem, such that its extension to 3D reacting flows is straightforward.

For nonstiff cases when the reaction zone is well-resolved in space and time, the present SPRANTS method gradually degenerates to a deterministic ODE solver upon modification of the sampling interval in Eq. (30) as

$$T^{**} = \begin{cases} T^* - \frac{1}{2}(T^+ - T^-)f, & \text{if } f < 1, \\ T^*, & \text{otherwise,} \end{cases} \tag{34}$$

where

$$f = N\left|\frac{T^+ - T^-}{T^{++} - T^{--} + \epsilon}\right|. \tag{35}$$

T^{++} is an estimated upper bound of the temperature after N time steps (e.g., $N = 5$) and T^{--} corresponding to its reverse state according to Eqs. (27) and (28), and ϵ is a small positive number. Thus f represents a dynamic measure for the time resolution of the respective reaction. One can see that, when the resolution is fine and linear approximation applies to temperature evolution, $f \to 1$ and Eq. (34) gives

$$\lim_{f\to 1} E(T^{**}) = E(T^*) - \frac{1}{2}(T^+ - T^-) = T^- < T \tag{36}$$

for a uniformly distributed θ_n in Eq. (30). The random time-stepping of reactions therefore reduces to a deterministic process according to Eq. (31) in non-stiff cases.

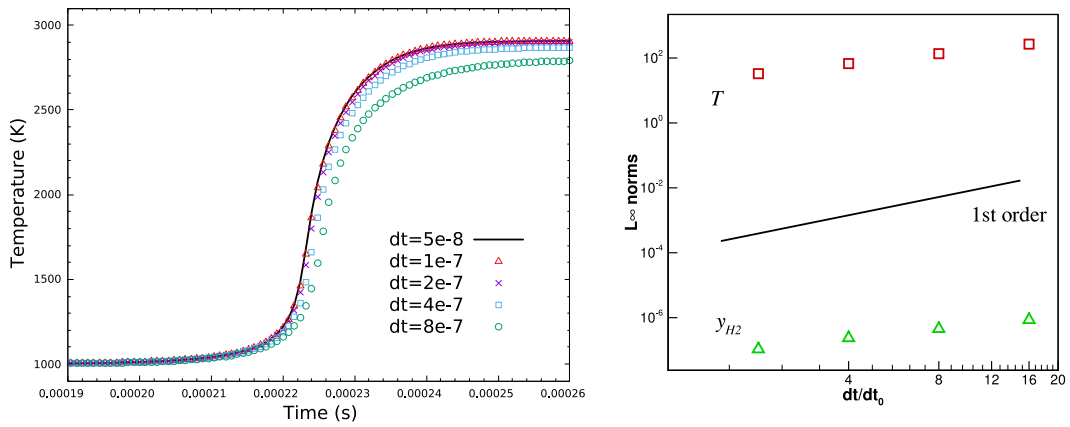

Fig. 4. Temperature histories using different timesteps (left) and L_∞ error norms of temperature and mass fraction y_{H_2} (right); $T_0 = 1000$ K and $dt_0 = 5 \times 10^{-8}$ s.

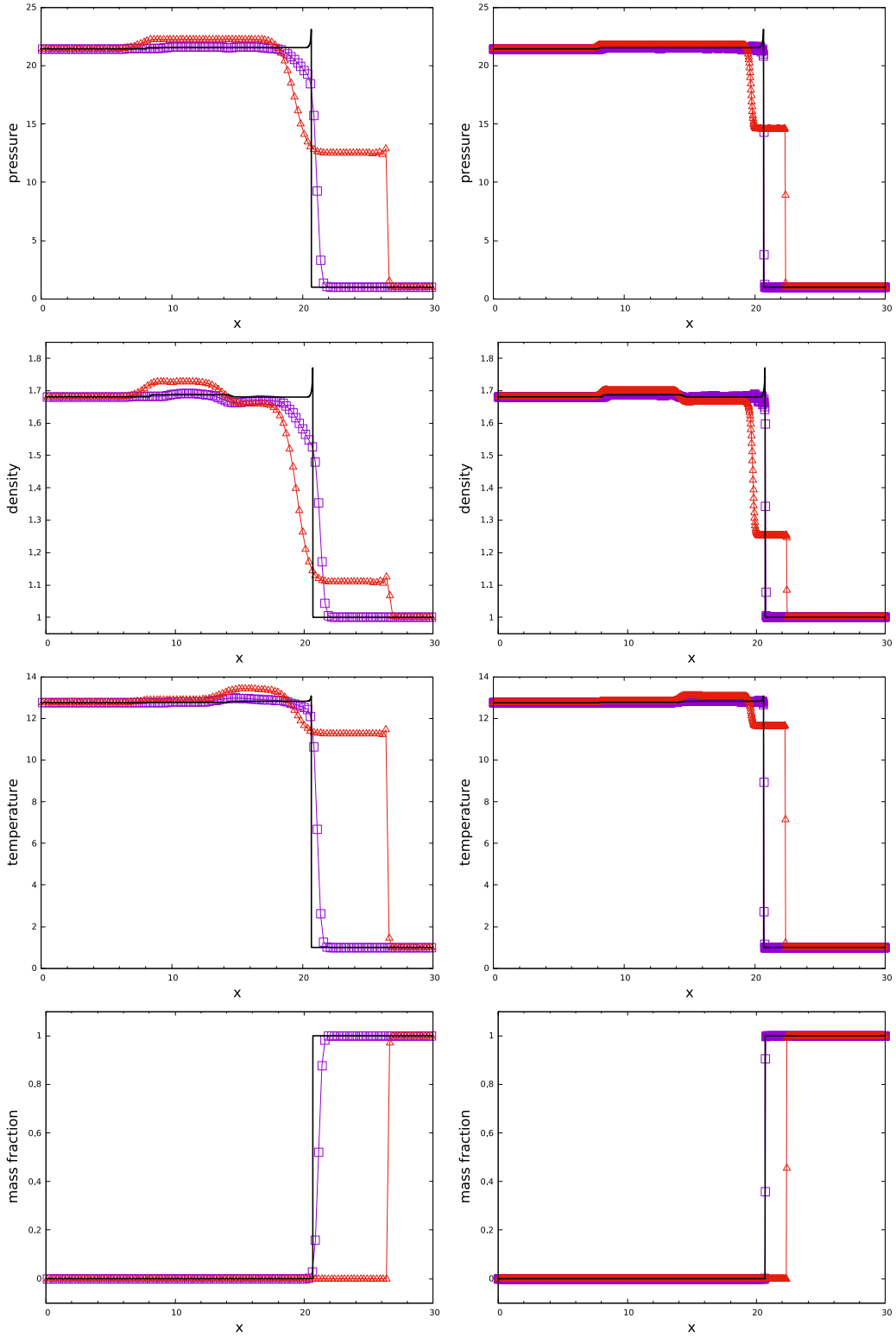

Fig. 5. Example 1 one reaction, CJ detonation at $t = 1.5$. Purple square line: SPRANTS solution; red triangle line: deterministic solution with Arrhenius kinetics; black solid line: reference solution; left column: $\Delta x = 0.25,\ \Delta t = 0.01$; right column: $\Delta x = 0.025,\ \Delta t = 0.001$. (For interpretation of the references to color in this figure legend, the reader is referred to the web version of this article.)

Remark 5. Due to the reduced randomness between activation and deactivation, the proposed SPRANTS method can also cope with nonstiff problems while the original random projection method is suitable for under-resolved stiff cases [7].

3. Numerical results and discussion

In this section, we consider three types of numerical experiments. The first serves to assess the split reaction-by-reaction ODE solver based on either analytical solutions or QSS approximation

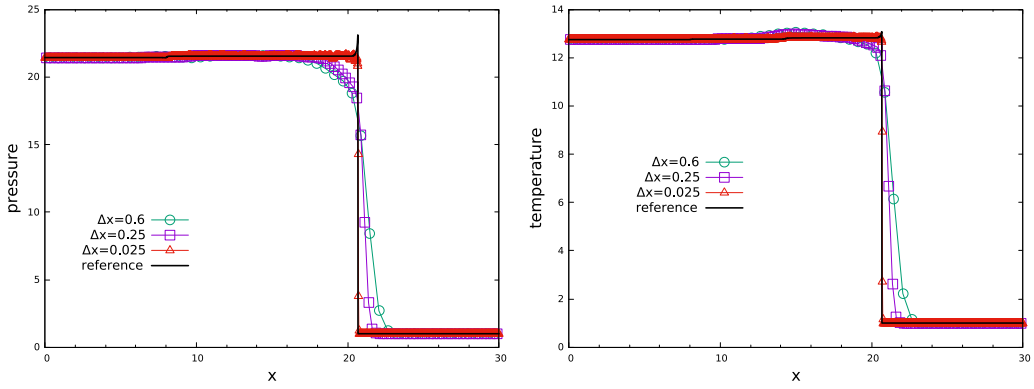

Fig. 6. Example 1 SPRANTS results at $t = 1.5$ with varying resolutions. The timestep for the $\Delta x = 0.6$ grid is equally scaled from $\Delta x = 0.25$, $\Delta t = 0.01$.

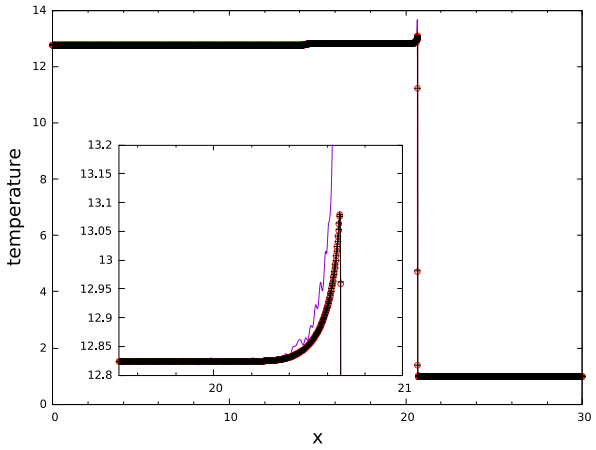

Fig. 7. Example 1 temperature profiles at $t = 1.5$ by SPRANTS with or without the drift term using the resolved grid and timestep of $\Delta x = 0.0025$, $\Delta t = 0.0001$. Purple line: SPRANTS solution without drift term; red circle line: SPRANTS solution with drift term; black cross line: reference solution. (For interpretation of the references to color in this figure legend, the reader is referred to the web version of this article.)

for the zero-dimensional reaction operator, ignoring fluid transport. The following two types consider the coupled fluid dynamics with chemical kinetics by using simplified model kinetics and realistic finite-rate kinetics, respectively, in 1D or 2D.

3.1. Reaction-split ODE solver for chemical kinetics

3.1.1. Michaelis–Menten test

The first case is the Michaelis–Menten system [37], i.e. $S_1 + S_2 \xrightarrow{k_1} S_3$, $S_3 \xrightarrow{k_2} S_1 + S_2$, $S_3 \xrightarrow{k_3} S_2 + S_4$, where the rate constants $k_1 = 10^6$, $k_2 = 10^{-4}$ and $k_3 = 10^{-1}$. The initial concentrations are 5×10^{-7} for S_1 and 2×10^{-7} for S_2 with $S_3 = 0$ and $S_4 = 0$ [37,38]. For this case, analytical solutions are provided for each reaction, see Appendix A. Reactions are simulated until $t = 50$. In Table 1, the L_1 and L_∞ error norms of species S_1 and S_4 are detailed, showing the expected convergence rates, i.e. 1st order for Lie–Trotter splitting and 2nd order for Strang splitting.

3.1.2. Hydrogen–air ignition delay test

Hydrogen ignition in air considers not only temperature-dependent reversible reactions but also third-body reactions, making the approximate solution to each reaction is practically preferred. The mechanism of H_2–air combustion follows O'Conaire et al. [39], consisting of 9 species (including the inert N_2) with 23 reversible reactions (equivalent to 46 one-way reactions). This mechanism has exhibited good prediction for the ignition delay time in [40]. All temperature-dependent reaction rates are calculated using the Arrhenius law

$$k_r = AT^B \exp(-T_{ign}/T), \tag{37}$$

where the subscript r is f for forward reactions or b for backward reactions and T is the temperature. Parameters A, B and T_{ign} for the forward rate of each reaction are often given in the mechanism. Backward rates often need to be calculated from the equilibrium constant K_{eq} and k_f by assuming the corresponding reaction to be in chemical equilibrium, i.e. $K_{eq} = k_f/k_b$ [41]. The third-body effect is accounted for by the summation of third-body collision efficiencies times the corresponding molar densities of species.

Initially the reactive H_2-air mixture is at a pressure of 1 atm, and has molar ratio 2: 1: 3.76 for H_2: O_2: N_2. Nitrogen is inert. All simulations end at $t = 1 \times 10^{-3}$ s. First we vary the initial temperature T_0 from 950 K to 1400 K in steps of 50 K. A fixed timestep of 1×10^{-8} s and Lie–Trotter splitting are applied. We compare the ignition delay times predicted by the present solver with the experimental data and CHEMKIN [42] results from Ref. [40] (see its Fig. 3) in Fig. 1 (left). The present QSS-based reaction-split method (or abbreviated as QRS) exhibits good predictions for the ignition induction of hydrogen using the present mechanism, especially in the high initial temperature range. In Fig. 1 (right), we compare the computed mass fractions with CHEMEQ2 at an initial temperature of 1000 K, and good agreement is achieved especially for the ignition time. For either QRS or CHEMEQ2, there is little difference between CPU times with different initial temperatures. QRS, however, exhibits better efficiency than CHEMEQ2 for the 9-species 23-reaction mechanism at a fixed timestep, as shown in Fig. 2. By choosing the initial temperatures at 1000 K and 1200 K, respectively, we consider the mass conservation of QRS and CHEMEQ2 in Fig. 3. It is readily to see that QRS can always preserve the mass, whereas for the CHEMEQ2 results some total mass loss or gain occurs around the ignition time.

We continue to consider the accuracy of QRS by adjusting the timestep from 5×10^{-8} s to 8×10^{-7} s with an amplifying factor of 2. The initial temperature is fixed at 1000 K. Figure 4 (left) shows that the temperature profiles converge with decreasing timesteps. By assessing the error norms of temperature and mass fraction of H in Fig. 4 (right), it can be seen that QRS is 1st-order convergent when Lie–Trotter splitting is applied.

3.2. Reactive Euler equations with simplified model kinetics

In this part, we consider reactive Euler equations coupled with simplified model kinetics in several stiff detonation problems. In

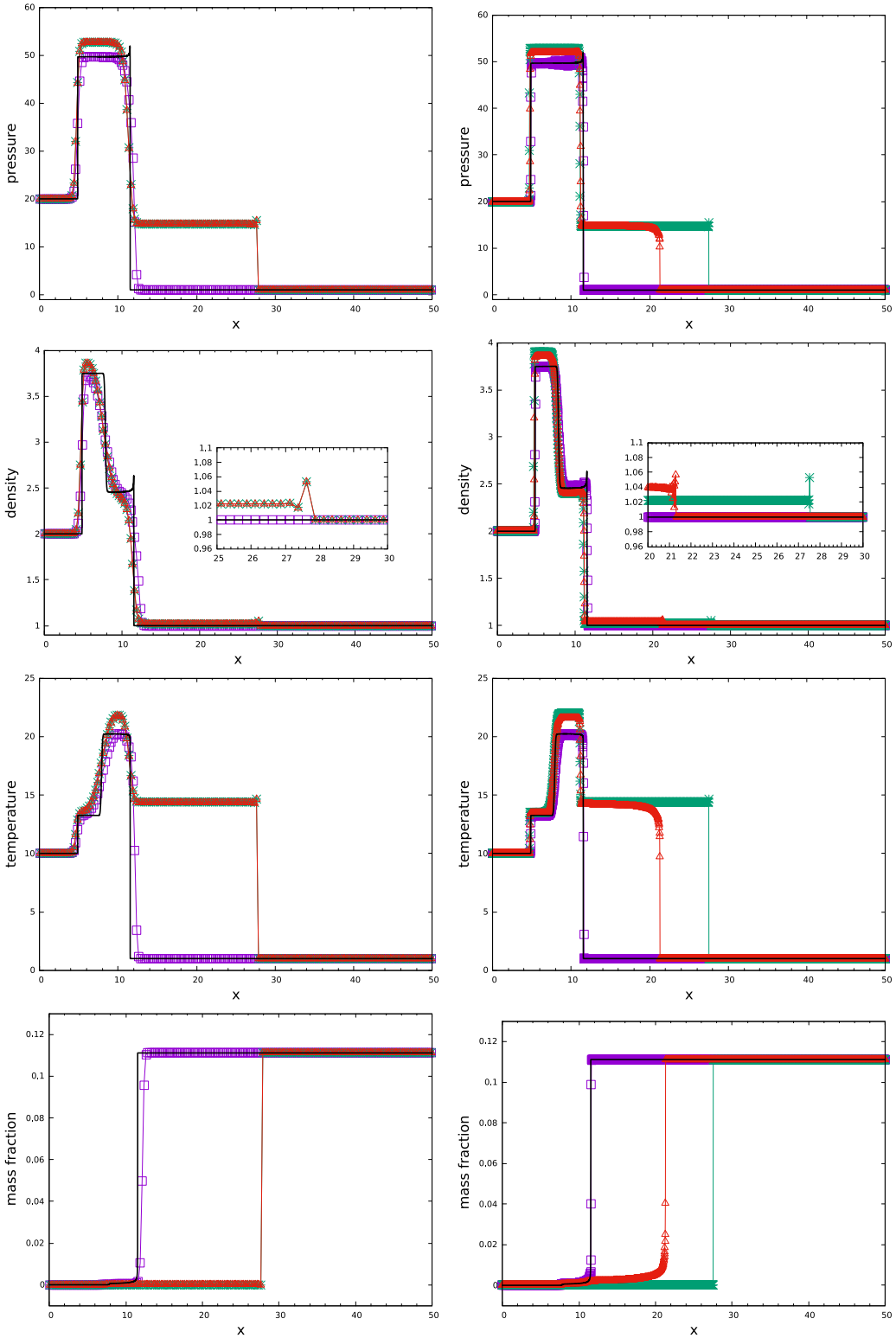

Fig. 8. Example 2 one reaction, strong detonation at $t = 1$. Purple square line: SPRANTS solution; red triangle line: deterministic solution with Arrhenius kinetics; green cross line: deterministic solution with Heaviside kinetics; black solid line: reference solution; left column: $\Delta x = 0.25$, $\Delta t = 0.01$; right column: $\Delta x = 0.025$, $\Delta t = 0.001$. (For interpretation of the references to color in this figure legend, the reader is referred to the web version of this article.)

such cases, the Arrhenius form of reaction rates in Eq. (37) also can be written as Heaviside form

$$k_r = \begin{cases} AT^B, & T \geq T_{ign}, \\ 0, & T < T_{ign}. \end{cases}$$

The EoS in Eq. (3) for the model problems is simplified by

$$p = (\gamma - 1)(\rho e - q_1 \rho y_1 - q_2 \rho y_2 - \cdots - q_{N_s} \rho y_{N_s})$$

and $T = p/\rho$. Numerical experiments cover single reaction to multi-reaction system in 1D and 2D detonation problems. In our computation, the AUSM+ scheme [28] is employed together with MUSCL reconstruction using a TVD Minmod limiter [43] in the

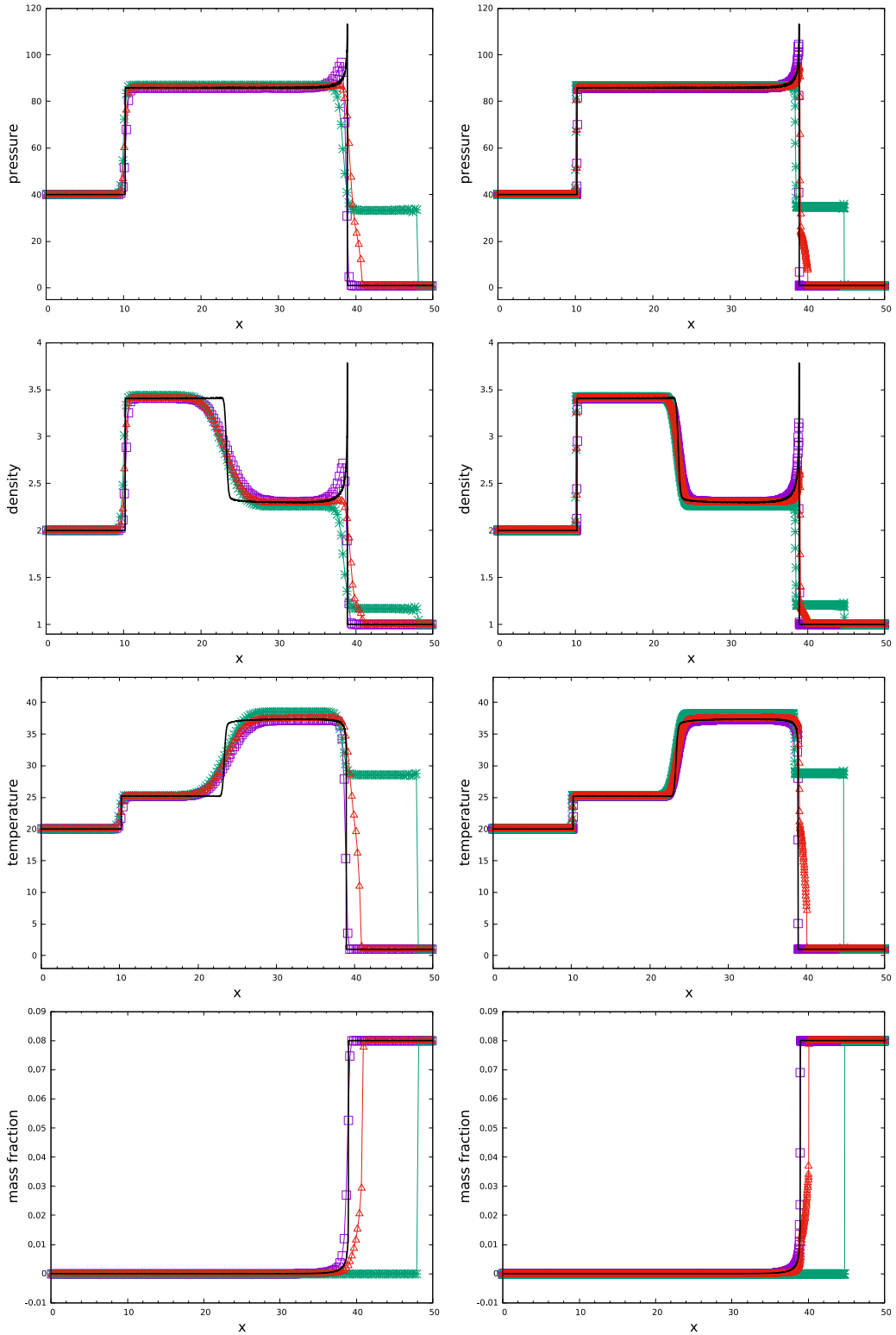

Fig. 9. Example 3 two reactions, strong detonation at $t = 3$. Purple square line: SPRANTS solution; red triangle line: deterministic solution with Arrhenius kinetics; green cross line: deterministic solution with Heaviside kinetics; black solid line: reference solution ($\Delta x = 0.0025,\ \Delta t = 0.0001$); left column: $\Delta x = 0.25,\ \Delta t = 0.01$; right column: $\Delta x = 0.025,\ \Delta t = 0.001$. (For interpretation of the references to color in this figure legend, the reader is referred to the web version of this article.)

convection step. The reaction step adopts the proposed SPRANTS method or QRS as a deterministic method.

Example 1 (Chapman–Jouguet (CJ) detonation)**.** The first case considers the simplest reacting model, which has been studied in [7], with only one reaction and two mutually dependent species

$$A \longrightarrow B,$$

where A represents the fuel being burnt by the one-way reaction and mass fraction of the product can be given directly by $y_B = 1 - y_A$.

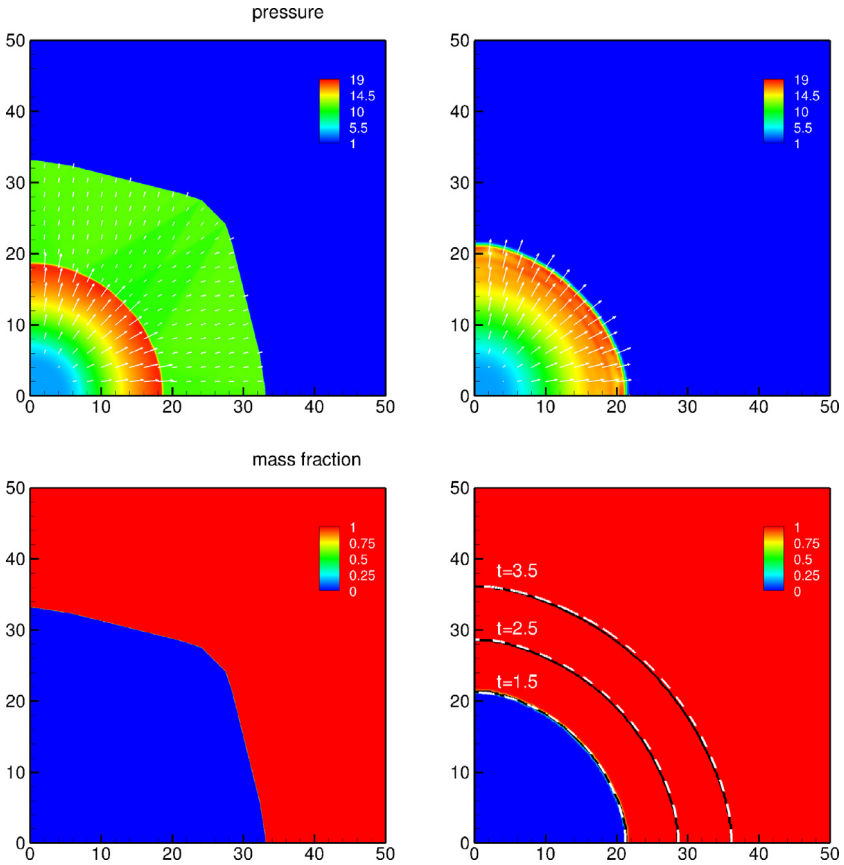

Fig. 10. Example 4 2D case, one infinite-rate reaction, CJ detonation. Left: deterministic solution; right: SPRANTS solution. Locations of the CJ detonation wave at three times are marked by $y_A = 0.5$ with black solid line (low resolution) and white dashed line (high resolution).

Parameters for the reaction model and species properties are

$$(\gamma, q_A, q_B) = (1.4, 25, 0),$$
$$\left(A, B, T_{ign}\right) = (16418, 0.1, 15). \tag{38}$$

Note that the ignition temperature T_{ign} is only used by the deterministic method. The initial condition to generate the detonation wave consists of two parts in only one spatial dimension, with piecewise constants given by

$$(p, T, u, y_A, y_B) = \begin{cases} (21.435, 12.75134, 2.899, 0, 1), & x < 10, \\ (1, 1, 0, 1, 0), & x \geq 10. \end{cases}$$

The left part gas is at the burnt equilibrium state and moves at a speed u_{CJ} relative to the stationary unburnt gas of the right part. The initial CJ state on the left can be obtained in theory [1,4,7]. This problem is solved on the interval [0, 30]. The left-end boundary condition is the inflow condition with fixed identical constants as the initial data on the left. Boundary condition for the right end is extrapolation from the mirror image points inside the domain.

The exact solution is simply a CJ detonation wave moving to the right and we obtain the reference 'exact' solution by the deterministic method (QRS) using a well-resolved grid ($\Delta x = 0.0025$) and a timestep of $\Delta t = 0.0001$. We compare the under-resolved results by SPRANTS and QRS, respectively, using two sets of grid ($\Delta x = 0.25, 0.025$) and timestep ($\Delta t = 0.01, 0.001$) with the same kinetics. Figure 5 shows the computed pressure, density, temperature and mass fraction. The proposed random method can capture the correct propagation of the detonation wave with both coarse and fine grids, while the deterministic method produces the spurious solutions in the same under-resolved conditions, i.e. a weak detonation wave propagates faster than the theoretical detonation speed of $D_{CJ} = 7.124$ in this case. Since a coarser grid with a larger timestep renders the stiffness more severe, the deterministic method produces far more nonphysical weak detonation wave compared to the SPRANTS or the reference solution. The location of the reacting front on the coarse grid may be shifted from the exact location due to randomization, but the shift amplitude does not grow in time [1], whereas the error accumulates with the deterministic method.

In Fig. 6, the SPRANTS result based on a very coarse grid ($\Delta x = 0.6$ corresponding to 50 grid points) is compared with the aforementioned under-resolved solutions by SPRANTS in terms of pressure and temperature at $t = 1.5$. Correct location of the detonation wave is captured despite the smeared discontinuity. Convergence of pressure and temperature profiles with an increasing resolution can be seen towards the reference solution, demonstrating the accuracy of the proposed SPRANTS method in capturing the correct propagation speed of discontinuities at under-resolved conditions. We also notice that a grid of 300 nodes is employed to obtain the correct wave propagation in [7] and 50 grid points are used by a high-order finite difference scheme (WENO5/SR) in [18] for this case.

In Fig. 7, we demonstrate that with the drift term the SPRANTS solution captures not only the correct location of reacting front but also the resolved reaction zone, in good agreement with the reference solution obtained by the deterministic method. Without the drift term, although the random method can still give the correct shock propagation, it fails to capture details of the resolved post-shock reaction zone by overshooting the temperature magnitude.

Example 2 (Strong detonation)**.** This example considers a reacting model, which has been studied in [7], with one reaction and three

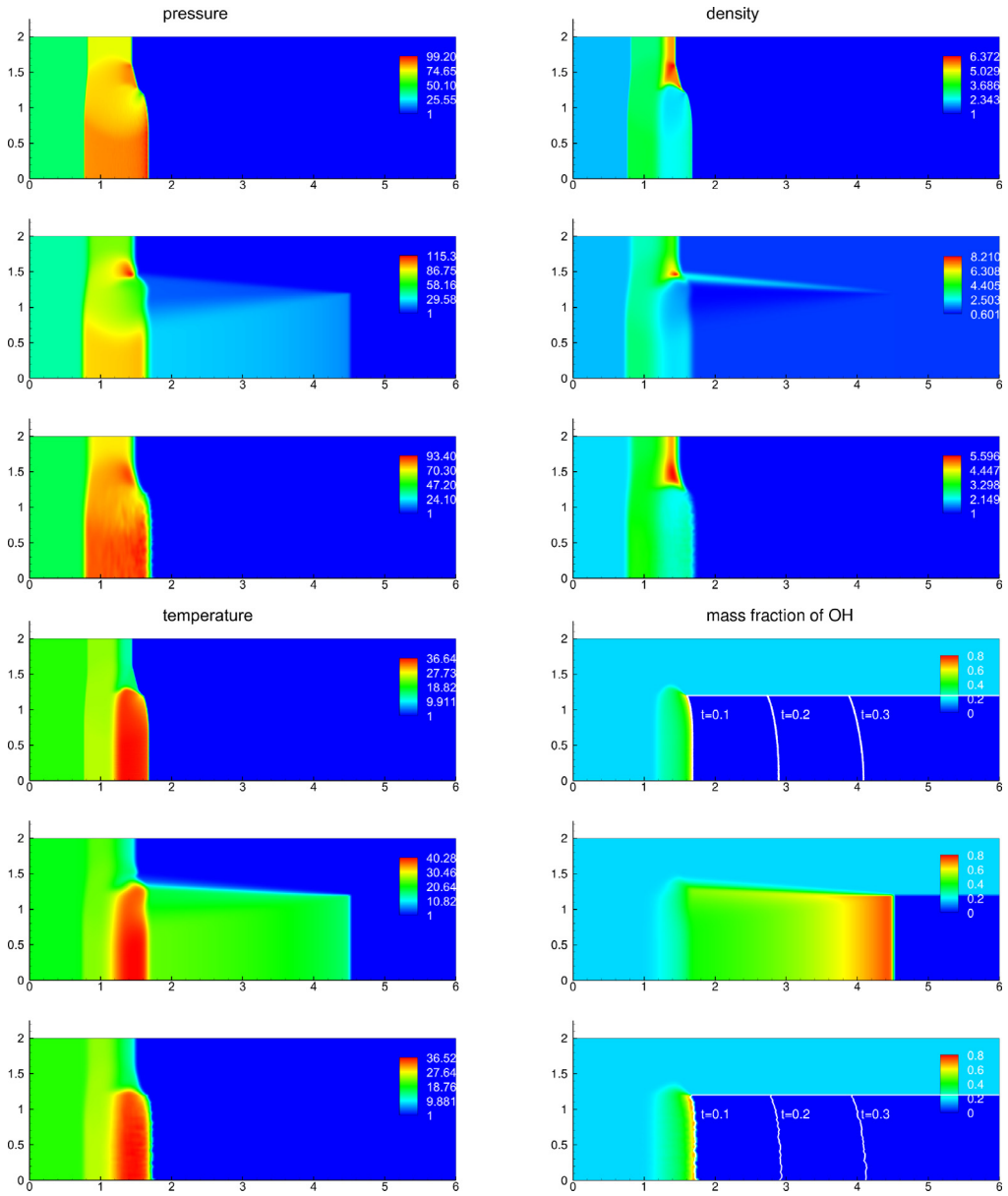

Fig. 11. Example 5 2D case, two reactions, strong detonation at $t = 0.1$. Top: reference solution; middle: deterministic solution with Arrhenius kinetics; bottom: SPRANTS solution; in the mass fraction contour, locations of the detonation front at $t = 0.1, 0.2, 0.3$ are additionally marked by setting $y_{O_2} = 0.5$ in white solid lines.

species

$$2H_2 + O_2 \longrightarrow 2H_2O.$$

Parameters for the reaction kinetics and species properties are

$$\left(\gamma, q_{H_2}, q_{O_2}, q_{H_2O}, W_{H_2}, W_{O_2}, W_{H_2O}\right) = (1.4, 300, 0, 0, 2, 32, 18),$$
$$\left(A, B, T_{ign}\right) = \left(10^6, 0, 2\right).$$

The initial condition of piecewise constants is given by

$$\left(p, T, u, y_{H_2}, y_{O_2}, y_{H_2O}\right) = \begin{cases} (20, 10, 8, 0, 0, 1), & x < 2.5, \\ \left(1, 1, 0, \frac{1}{9}, \frac{8}{9}, 0\right), & x \geq 2.5. \end{cases}$$

The left part gas is at the burnt equilibrium state and it is moving at a speed larger than u_{CJ} relative to the stationary unburnt gas of the right part so that a strong detonation wave is to occur. This problem is solved on the interval [0, 50].

The exact solution consists of a detonation wave, followed by a contact discontinuity and a shock, all moving to the right. Again, we obtain the reference solution by QRS using a resolved grid ($\Delta x = 0.0025$) and a very small timestep ($\Delta t = 0.0001$). We compare the results by SPRANTS and the deterministic method using a coarse grid and a finer grid with stable timesteps, as explained in Fig. 8. Note that in the deterministic method, we adopt both the Arrhenius model and the Heaviside model for the chemical kinetics. The proposed SPRANTS method can capture all discontinuities effectively, while the deterministic method produces spurious solutions at the same under-resolved conditions. In particular, using the Heaviside model, the deterministic method produces a less accurate solution due to the stronger stiffness compared to the Arrhenius model (see the right column of Fig. 8).

Example 3 (Strong detonation)**.** This case considers a multi-step reaction mechanism with two one-way reactions and five species

1) $H_2 + O_2 \longrightarrow 2OH,$
2) $2OH + H_2 \longrightarrow 2H_2O,$

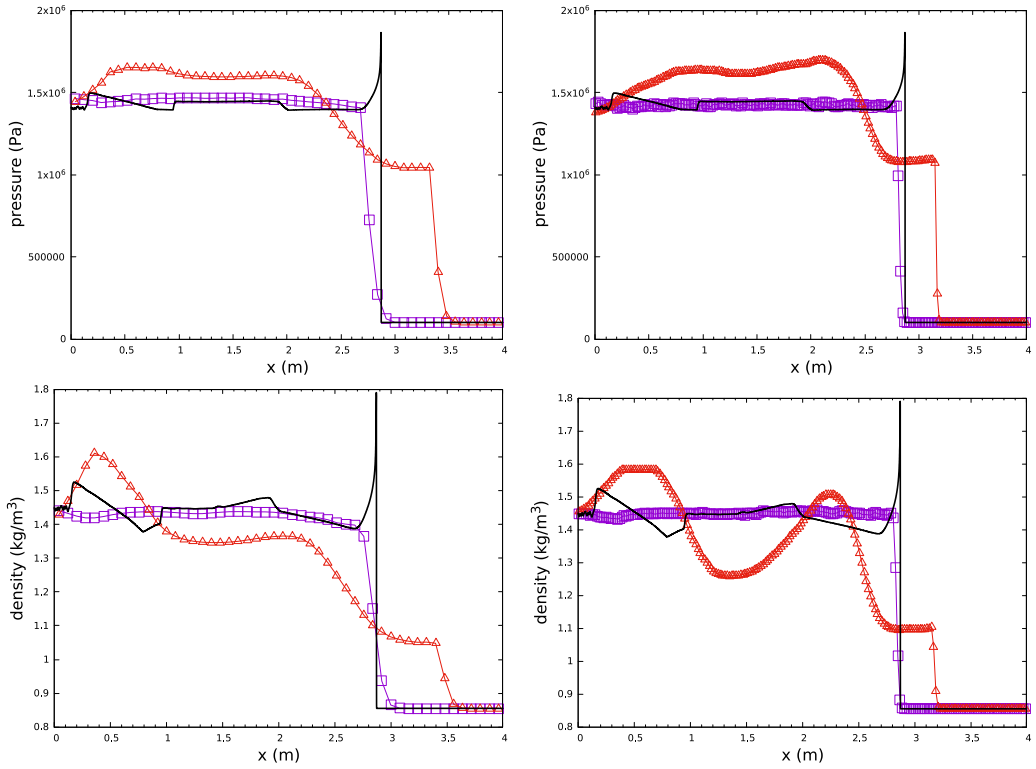

Fig. 12. Example 6 hydrogen–air CJ detonation at $t = 1.2 \times 10^{-3}$ s. Purple square line: SPRANTS solution; red triangle line: deterministic solution by CHEMEQ2; black solid line: reference solution; left column: $\Delta x = 0.08$ m, $\Delta t = 1 \times 10^{-6}$ s; right column: $\Delta x = 0.02$ m, $\Delta t = 2.5 \times 10^{-7}$ s. (For interpretation of the references to color in this figure legend, the reader is referred to the web version of this article.)

Table 2
Initial condition for hydrogen–air CJ detonation in Example 6.

	Post-shock gas	Pre-shock gas
Pressure (Pa)	1481999.362037	101,325
Temperature (K)	2941.677242	298
Velocity (m/s)	800 ($\approx u_{CJ}$)	0
Mass fraction		
y_H	0.000247	0
y_O	0.001617	0
y_{H_2O}	0.225404	0
y_{OH}	0.014915	0
y_{O_2}	0.013336	0.226362
y_{H_2}	0.002429	2.852103E−2
$y_{H_2O_2}$	2.601600E−6	0
y_{HO_2}	1.857550E−5	0
y_{N_2}	0.742031	0.745117

with N_2 as a dilute catalyst. Similar examples have been studied in Example 5.4 [3].

Parameters for the reaction model and species properties are

$$\left(\gamma, q_{H_2}, q_{O_2}, q_{OH}, q_{H_2O}, q_{N_2}\right) = (1.4, 0, 0, -20, -100, 0),$$
$$\left(W_{H_2}, W_{O_2}, W_{OH}, W_{H_2O}, W_{N_2}\right) = (2, 32, 17, 18, 28),$$
$$\left(A^1, B^1, T^1_{ign}\right) = \left(10^5, 0, 2\right),$$
$$\left(A^2, B^2, T^2_{ign}\right) = \left(2 \times 10^4, 0, 10\right).$$

The initial condition of piecewise constants is given by

$$\left(p, T, u, y_{H_2}, y_{O_2}, y_{OH}, y_{H_2O}, y_{N_2}\right) = \begin{cases} (40, 20, 10, 0, 0, 0.17, 0.63, 0.2), & x < 2.5, \\ (1, 1, 0, 0.08, 0.72, 0, 0, 0.2), & x \geq 2.5. \end{cases}$$

This problem is solved on the interval [0, 50].

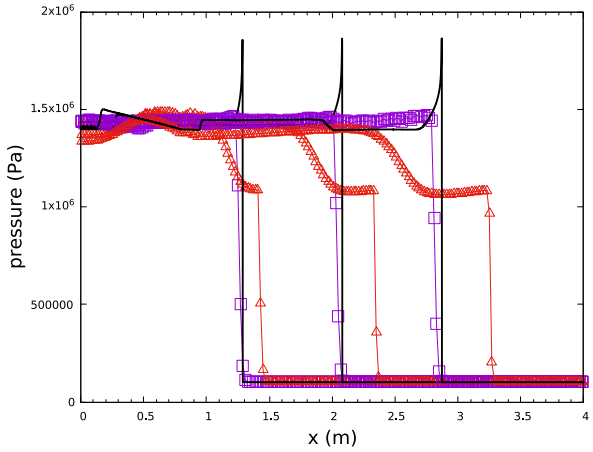

Fig. 13. Example 6 hydrogen–air CJ detonation at $t = 0.4, 0.8, 1.2 \times 10^{-3}$ s. Purple square line: SPRANTS solution; red triangle line: deterministic solution by CHEMEQ2; black solid line: reference solution; both solutions use $\Delta x = 0.02$ m, $\Delta t = 2.5 \times 10^{-7}$ s. (For interpretation of the references to color in this figure legend, the reader is referred to the web version of this article.)

Figure 9 presents different computational conditions and results obtained accordingly. All waves are captured with the correct speeds by the SPRANTS method, in good agreement with the reference solution. However, the deterministic method obviously cannot handle the Heaviside model with the same under-resolved grids and timesteps. Although the slower propagation of the reacting front is captured by the Arrhenius model, the deterministic method still results in spurious weak detonation, refer to the transit points around $x \approx 40$ especially in the profiles at the right column of Fig. 9.

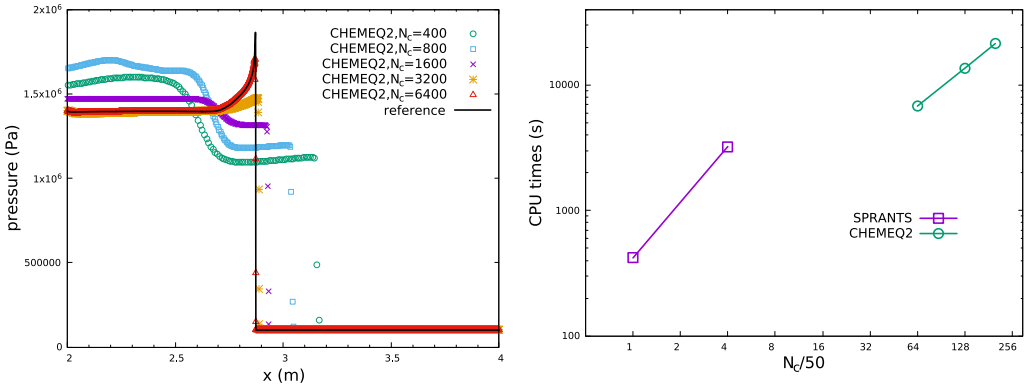

Fig. 14. Example 6 hydrogen–air CJ detonation at $t = 1.2 \times 10^{-3}$ s by the deterministic method with CHEMEQ2 using different grids (left) and CPU times (s) compared to SPRANTS on two coarser grids (right).

Example 4 (CJ detonation in 2D)**.** This 2D case extends EXAMPLE 1 to a radially symmetric point-source explosion, where A in Eq. (38) is amplified by a factor of 10,000 to approximate the infinitely fast reaction with extreme stiffness. Similar tests have been studied in [3,16].

A quarter domain is considered exploiting sectorial symmetry on $[0,\ 50]\times[0,\ 50]$. The hot-spot area of the initial high-temperature high-pressure burnt gas is a circle with radius 10 and the reactive unburnt gas takes the outside. Initial condition is the same as in Example 1 except the initial velocity of the circle area is adjusted to along the radial direction, i.e.

$$(u, v) = \begin{cases} (2.899x/r, 2.899y/r), & r < 10, \\ (0, 0), & r \geq 10, \end{cases}$$

where $r = \sqrt{x^2 + y^2}$.

In our computations, a coarse grid (200×200) and a finer grid (2000×2000) are employed referring to Example 1. Corresponding timesteps are $\Delta t = 1 \times 10^{-2}$ and 1×10^{-3}, respectively. With the finer grid, the deterministic method still produces a spurious solution at $t = 1.5$, see the left column of Fig. 10, in that a nonphysical weak detonation wave is generated and the reacting front is no more circular. In contrast, the SPRANTS method can capture shape and location of the CJ detonation front accurately, see the right column of the figure, by observing the radial velocity vector in the pressure contour even in the low resolution and the self-similarly circular outwards-developing detonation fronts in black/white lines of two resolutions at different times. The line-marked locations calculated by the random method in two resolutions agree excellently with each other and thus a grid convergence to the exact solution is reasonable to expect for the proposed SPRANTS method. With negligible curvature effects [44,45] and the under-resolved reaction zone being infinitesimal, the calculated speed of the detonation front approaches the 1D theoretical speed of $D_{CJ} = 7.1247$ as in Example 1.

Example 5 (Strong detonation in 2D)**.** The present case considers the same multi-step reaction mechanism as in Example 3 except that q_{OH} in Eq. (38) changes into -50. This is a 2D case used to prove the dimension-independent nature of the proposed method, unlike the original random projection method which requires a dimension-by-dimension scanning for local projection. Geometry and initial condition of piecewise constants in the 2D domain can be referred to [7].

A uniformly distributed coarse grid (300×100) and a refined grid (3000×1000) are employed. Corresponding timesteps are $\Delta t = 5 \times 10^{-4}$ and 5×10^{-5}, respectively. The reference solution is obtained by the deterministic method using the fine grid and tiny timestep. The comparison of the SPRANTS method and deterministic method on capturing stiff detonation waves is based on the under-resolved grid and timestep. In Fig. 11, at $t = 0.1$ the spurious solution given by the deterministic method on the coarse grid contains a too fast weak detonation wave, which has passed half of the domain. However, the correct detonation waves from the SPRANTS method on the same resolution and the deterministic method on a fine grid agree with each other excellently. Good agreement of the self-similar propagation of the detonation wave from $t = 0.1$ to 0.3 also can be seen in the mass fraction contour given by the reference solution and the under-resolved SPRANTS solution, respectively. The slight difference between the two solutions lies in some small near-shock statistical fluctuations due to the random nature of the method [1].

Table 3
CPU times (s) by SPRANTS and the deterministic method with CHEMEQ2 in Example 6.

N_c	50	200	3200	6400	10000
	✓	✓			
SPRANTS	418.523	3235.12			
	×	×	✓	✓	✓
CHEMEQ2	52.9419	214.142	6788.82	13592.8	21356.0

N_c represents the number of grid points and symbol ✓or × indicates the correct or incorrect wave propagation being captured.

3.3. Reactive Euler equations with realistic nonequilibrium kinetics

In this subsection, we validate the SPRANTS method for capturing stiff detonation waves governed by the reactive Euler equations coupled with realistic chemical nonequilibrium kinetics which introduces multiple temperature-dependent reactions with distinct timescales. To our knowledge, both the two test cases below are reported for the first time, taking into account the detailed hydrogen–air combustion mechanism as in Section 3.1.2. Two different scenarios with a CJ detonation and strong detonation wave, respectively, are simulated in 1D or 2D domain. The convection operator adopts an ordinary shock capturing scheme as in the former subsection, and the reaction step is solved by the proposed SPRANTS method and CHEMEQ2 as the deterministic method to make a comparison. Reaction splitting in the SPRANTS method employs the 2nd-order Strang scheme to reduce splitting errors.

Example 6 (Realistic CJ detonation)**.** The setup consists of two parts divided by a shock moving to the right in a 1D domain of length $L = 4$ m, as in Table 2. The theoretical CJ detonation states for the unburnt gas can be generated using the NASA Chemical

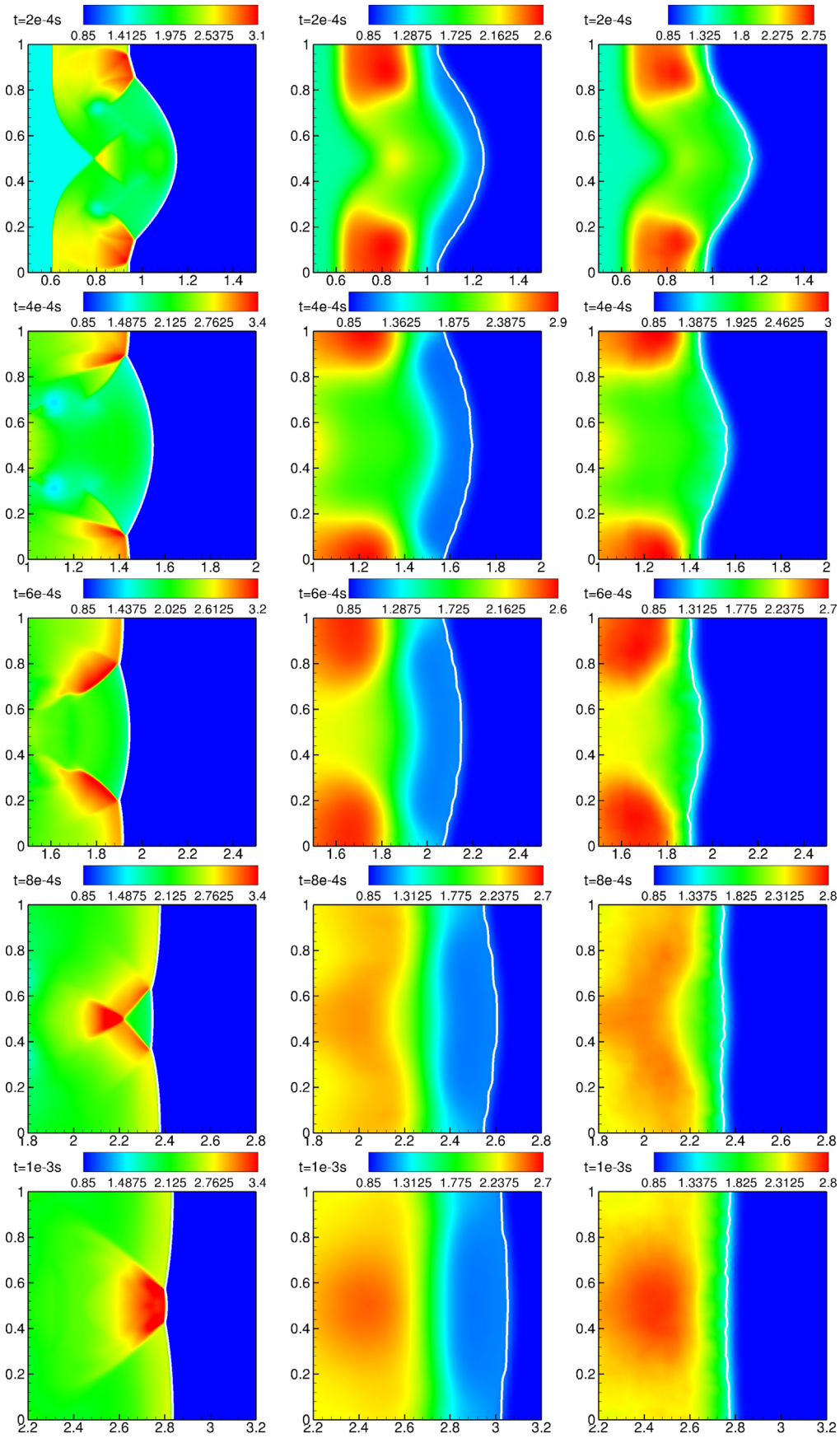

Fig. 15. Example 7 the density distribution and the detonation front location at different times. Left: reference solution; middle: deterministic solution by CHEMEQ2; right: SPRANTS solution; the location of the reacting front is marked by the white solid line with $y_{H_2O} = 0.1$.

Equilibrium Analysis (CEA) program [46], and according to the CJ condition [1,4,7], i.e.

$$D_{CJ} = u_{CJ} + (\gamma p_b/\rho_b)^{1/2},$$

we adopt $u_b = 800\,\text{m/s} \approx u_{CJ}$ for the initial velocity of the burnt gas, to generate a CJ detonation wave sweeping the stationary unburnt gas. The shock is initially located at $x = 0.4$ m. Boundary condition for the left/right end is simply extrapolation from the mirror image points inside the domain. All simulations are terminated at $t = 1.2 \times 10^{-3}$ s and use the same mechanism [39].

The exact solution is a steady self-similar CJ detonation wave traveling from left to right. We obtain the reference exact solution by the deterministic method using a very fine grid with 10,000 points and a fixed tiny timestep of $\Delta t = 5 \times 10^{-8}$ s. Two sets of under-resolved grid and timestep are considered, i.e. $\Delta x = 0.08$ m, $\Delta t = 1 \times 10^{-6}$ s and $\Delta x = 0.02$ m, $\Delta t = 2.5 \times 10^{-7}$ s, respectively.

In Fig. 12 at the given time: although the resolution of the grid and timestep is far lower than the resolved solution, the SPRANTS method predicts the properties of the flowfield in quite good agreement with the reference solution, including the location of the detonation wave and profiles of the mixture pressure and density. The obtained profiles tend to converge to the reference solution with increasing resolution (and decreasing stiffness). In contrast, using the same under-resolved grid and timestep, the deterministic method yields the spurious nonphysical weak detonation ahead of the shock and the flowfield profiles are totally changed in an incorrect way. In Fig. 13, wave propagation at different times is presented by looking into the pressure distribution. Despite the deviation by few grid points, SPRANTS can always capture the correct wave location while the error in the location of reaction front by the deterministic method deteriorates by showing a too fast weak detonation wave. Note that the von Neumann spike inside the reaction zone of the reference solution can be calculated only by very fine resolution both in space and time.

In Fig. 14 (left), we additionally obtain several solutions by the deterministic method with CHEMEQ2 using $N_c = 400, 800$ up to 6400 grids with linearly decreasing global timesteps (lower to $\Delta t = 5 \times 10^{-8}$ s as the reference solution with $N_c = 10,000$). It can be seen that the pressure profiles converge to the reference solution (with 10,000 grid points) including the spurious weak detonation waves with $N_c = 400$ to 1600. When the number of grid points increases to 3200 or more, the weak detonation wave disappears and the correct location of the reacting front is captured. We compare the CPU times for the reaction step of two methods based on different grids, listed in Table 3 and plotted in Fig. 14 (right), as the computational cost of integrating the ODE system dominates in reacting flow simulations. With the same mechanism, SPRANTS consumes more CPU time in the reaction step than the deterministic method using the same resolution, since each random reaction needs to assume a forward state or backward state to determine the random temperature, invoking a costly iterative root-finding operation. The deterministic method requires a much higher resolution in both space and time to reach the same prediction accuracy so that its overall computational efficiency dramatically decreases.

Example 7 (Realistic strong detonation in 2D)**.** The setup consists of two parts divided by a shock traveling to the right in a rectangular domain of $[0, 3]$ m $\times$ $[0, 1]$ m. The post-shock burnt gas part is given by

$$\{|y - 0.5| > 0.25, x < 0.5\} \cup \{|y - 0.5| \le 0.25, x - 0.25 < y < 1.25 - x\},$$

and the unburnt gas occupies the remaining domain in front of the initial shock. Initial states are identical with those in Example 6 except for the x-velocity of the post-shock part being increased to $u_b = 2000$ m/s $> u_{CJ}$, to create a strong detonation wave. The boundary condition for the left/right end is simply extrapolation from the mirror image points inside the domain and the top/bottom boundary is considered as a slip wall. All simulations are finished at $t = 1 \times 10^{-3}$ s and still use the 9-species 23-reaction mechanism [39].

With the previous 1D example, it was shown that the deterministic solution based on a grid of 3200 points in the 4 m long domain recovers the correct shock position in Fig. 14 (left). Therefore, we generate a reference solution in 2D by the deterministic method using a fine grid with 3000×1000 points and a fixed tiny timestep of $\Delta t = 2.5 \times 10^{-8}$ s. A set of under-resolved uniform grid and timestep is also considered, i.e. 150×50, $\Delta t = 2.5 \times 10^{-7}$ s. Figure 15 displays the density distributions along with locations of the detonation wave at different times in three solutions. In comparison with the reference solution, the SPRANTS method gives reasonable locations of the reacting front at all times. Due to the low resolution used in SPRANTS, detailed characteristics presented in the reference solution such as the triple points, slip lines, small vortices and peak values of density are diffused while the overall flowfield including the profile of reacting front has been correctly captured. For the deterministic method with the same resolution, a spurious weak detonation wave can be observed with a maximum error of nearly 10% of the domain length within only 1 ms.

4. Conclusions

A new operator splitting method for simulating chemically reacting flows, especially for capturing stiff detonation waves in under-resolved conditions has been developed. Two procedures based on operator splitting are included: for the convection step, any shock-capturing scheme can be used; for the reaction step, the multi-species multi-reaction ODE system in the source terms is further split in a reaction-by-reaction manner. Each reaction either proceeds a timestep forward or is interrupted according to a local random temperature rather than a deterministic process with growing error accumulation. A wide range of numerical experiments including not only simple model kinetics but also realistic nonequilibrium chemistry such as the temperature-dependent finite-rate hydrogen–air combustion are considered in 1D and 2D flows, demonstrating the following properties:

1. Mass conservation and positivity of species concentration can be guaranteed by the reaction-split ODE solver, which is almost unconditionally stable due to its using either analytical or approximate exact solutions.
2. The proposed SPRANTS method can effectively predict the correct propagation of discontinuities as well as the overall flowfield information in under-resolved conditions, for both model kinetics and realistic finite-rate nonequilibrium kinetics.
3. Compared with the deterministic method using CHEMEQ2, the present SPRANTS method exhibits better computational efficiency as it can correctly capture the detonation wave with a larger timestep on coarse grids for nonequilibrium reactive flows.
4. By adding a drift term into the random temperature sampling, SPRANTS can recover the deterministic solution as the resolution improves with decreasing stiffness.
5. The dimension-independent algorithm for the source terms makes further 3D extension of the proposed method straightforward.

Employing high-order low-dissipation schemes for the present method is a subject of future research.

Acknowledgments

The financial support from the EU Marie Skłodowska-Curie Innovative Training Networks (ITN-ETN) (Project ID: 675528-IPPAD-H2020-MSCA-ITN-2015) for the first author is gratefully acknowledged. Xiangyu Y. Hu is also thankful for the partial support by National Natural Science Foundation of China (NSFC) (Grant No: 11628206).

Appendix A. Analytical solutions to some simple forms of a one-way reaction equation

For the simplest form of a reaction such as $A \longrightarrow$ products, we have an ODE for the molar concentration $[A]$, as $\frac{d[A]}{dt} = -k[A]$, with k being the rate constant and initial value of $[A]_0$ at $t = t_0$. This ODE written in terms of molar concentration is equivalent to Eq. (11) using density and mass fraction since $[A] = \frac{\rho_A}{W_A} = \frac{\rho y_A}{W_A}$. Its solution by separation of variables is $[A] = [A]_0 e^{-k(t-t_0)}$.

For the reaction form

$$A + B \longrightarrow \text{products}, \tag{A.1}$$

we have the ODE system as

$$\frac{d[A]}{dt} = \frac{d[B]}{dt} = -k[A][B]. \tag{A.2}$$

This means that $d[A] = d[B]$ holds for any time interval dt and thus

$$[A] - [A]_0 = [B] - [B]_0. \tag{A.3}$$

Substituting relation (A.3) into Eq. (A.2), we have $\frac{d[A]}{dt} = -k[A]([A] + \Delta_{AB})$, where $\Delta_{AB} = [B]_0 - [A]_0$, leading to the solution of $[A]$ as

$$[A] = \begin{cases} \frac{\Delta_{AB}}{\frac{[B]_0}{[A]_0} e^{\Delta_{AB} k(t-t_0)} - 1}, & \text{if } \Delta_{AB} \neq 0, \\ \frac{1}{k(t-t_0) + \frac{1}{[A]_0}}, & \text{otherwise.} \end{cases}$$

Reaction $2A \longrightarrow$ products is a special case of reaction (A.1) and the solution is $[A] = \frac{1}{k(t-t_0) + \frac{1}{[A]_0}}$.

For a third-order reaction $A + B + C \longrightarrow$ products, we also utilize the relations $[A] - [A]_0 = [B] - [B]_0 = [C] - [C]_0$ and perform separation of variables to obtain an implicit solution for $[A]_0 \neq [B]_0 \neq [C]_0$, i.e.

$$\left(\frac{[A]}{[A] + \Delta_{AC}} \frac{[C]_0}{[A]_0} \right)^{\frac{1}{\Delta_{CB}\Delta_{AC}}} - \left(\frac{[A]}{[A] + \Delta_{AB}} \frac{[B]_0}{[A]_0} \right)^{\frac{1}{\Delta_{CB}\Delta_{AB}}} = e^{-k(t-t_0)}.$$

Only for $[A]_0 = [B]_0 = [C]_0$ or for the special reaction $3A \longrightarrow$ products, an explicit analytical solution exists, i.e. $[A] = \sqrt{\frac{1}{\frac{1}{[A]_0^2} + 2k(t-t_0)}}$.

After the determination of the new state of the reactant species $[A]$, states of the remaining species including all the products and other reactants can be updated by mass conservation in Eq. (20).

References

[1] W. Bao, S. Jin, The random projection method for hyperbolic conservation laws with stiff reaction terms, J. Comput. Phys. 163 (1) (2000) 216–248.
[2] W. Bao, S. Jin, The random projection method for stiff detonation capturing, SIAM J. Sci. Comput. 23 (3) (2001) 1000–1026.
[3] W. Bao, S. Jin, The random projection method for stiff multispecies detonation capturing, J. Comput. Phys. 178 (1) (2002) 37–57.
[4] H.C. Yee, D.V. Kotov, W. Wang, C.-W. Shu, Spurious behavior of shock-capturing methods by the fractional step approach: problems containing stiff source terms and discontinuities, J. Comput. Phys. 241 (2013) 266–291.
[5] P. Colella, A. Majda, V. Roytburd, Theoretical and numerical structure for reacting shock waves, SIAM J. Sci. Stat. Comput. 7 (4) (1986) 1059–1080.
[6] R.J. LeVeque, H.C. Yee, A study of numerical methods for hyperbolic conservation laws with stiff source terms, J. Comput. Phys. 86 (1) (1990) 187–210.
[7] B. Zhang, H. Liu, F. Chen, J.H. Wang, The equilibrium state method for hyperbolic conservation laws with stiff reaction terms, J. Comput. Phys. 263 (2014) 151–176.
[8] X. Deng, H. Teng, B. Xie, F. Xiao, A new shock-capturing scheme for stiff detonation waves problems, arXiv:1708.01000 (2017).
[9] D. Nguyen, F. Gibou, R. Fedkiw, A fully conservative ghost fluid method and stiff detonation waves, 12th International Detonation Symposium, San Diego, CA, 2002.
[10] A. Bourlioux, A.J. Majda, V. Roytburd, Theoretical and numerical structure for unstable one-dimensional detonations, SIAM J. Appl. Math. 51 (2) (1991) 303–343.
[11] A. Bourlioux, A.J. Majda, Theoretical and numerical structure for unstable two-dimensional detonations, Combust. Flame 90 (3–4) (1992) 211–229.
[12] R. Jeltsch, P. Klingenstein, Error estimators for the position of discontinuities in hyperbolic conservation laws with source terms which are solved using operator splitting, Comput. Vis. Sci. 1 (4) (1999) 231–249.
[13] B.L. Bihari, D. Schwendeman, Multiresolution schemes for the reactive euler equations, J. Comput. Phys. 154 (1) (1999) 197–230.
[14] B. Engquist, B. Sjögreen, Robust difference approximations of stiff inviscid detonation waves, Department of Mathematics, University of California, Los Angeles, 1991.
[15] A. Berkenbosch, E. Kaasschieter, R. Klein, Detonation capturing for stiff combustion chemistry, Combust. Theory Model. 2 (3) (1998) 313–348.
[16] C. Helzel, R.J. Leveque, G. Warnecke, A modified fractional step method for the accurate approximation of detonation waves, SIAM J. Sci. Comput. 22 (4) (2000) 1489–1510.
[17] L. Tosatto, L. Vigevano, Numerical solution of under-resolved detonations, J. Comput. Phys. 227 (4) (2008) 2317–2343.
[18] W. Wang, C.-W. Shu, H.C. Yee, B. Sjögreen, High order finite difference methods with subcell resolution for advection equations with stiff source terms, J. Comput. Phys. 231 (1) (2012) 190–214.
[19] W. Wang, C.-W. Shu, H.C. Yee, D.V. Kotov, B. Sjögreen, High order finite difference methods with subcell resolution for stiff multispecies discontinuity capturing, Commun. Comput. Phys. 17 (2) (2015) 317–336.
[20] D.V. Kotov, H.C. Yee, M. Panesi, D.K. Prabhu, A.A. Wray, Computational challenges for simulations related to the nasa electric arc shock tube (East) experiments, J. Comput. Phys. 269 (2014) 215–233.
[21] K. Nguyen, A. Caboussat, D. Dabdub, Mass conservative, positive definite integrator for atmospheric chemical dynamics, Atmos. Environ. 43 (40) (2009) 6287–6295.
[22] S. Pan, J. Wang, X. Hu, N.A. Adams, A network partition method for solving large-scale complex nonlinear processes, arXiv:1801.06207 (2018).
[23] R.I. McLachlan, G.R.W. Quispel, Splitting methods, Acta Numer. 11 (2002) 341–434.
[24] G. Strang, On the construction and comparison of difference schemes, SIAM J. Numer. Anal. 5 (3) (1968) 506–517.
[25] A. Harten, High resolution schemes for hyperbolic conservation laws, J. Comput. Phys. 49 (3) (1983) 357–393.
[26] A. Harten, B. Engquist, S. Osher, S.R. Chakravarthy, Uniformly high order accurate essentially non-oscillatory schemes, III, J. Comput. Phys. 71 (2) (1987) 231–303, doi:10.1016/0021-9991(87)90031-3.
[27] G.-S. Jiang, C.-W. Shu, Efficient implementation of weighted ENO schemes, J. Comput. Phys. 126 (1) (1996) 202–228.
[28] M.-S. Liou, A sequel to AUSM: AUSM+, J. Comput. Phys. 129 (2) (1996) 364–382.
[29] P.N. Brown, G.D. Byrne, A.C. Hindmarsh, VODE: a variable-coefficient ODE solver, SIAM J. Sci. Stat. Comput. 10 (5) (1989) 1038–1051.
[30] D.R. Mott, E.S. Oran, CHEMEQ2: a solver for the stiff ordinary differential equations of chemical kinetics, Technical Report, Naval Research Lab, Washington DC, 2001.
[31] X. Gou, W. Sun, Z. Chen, Y. Ju, A dynamic multi-timescale method for combustion modeling with detailed and reduced chemical kinetic mechanisms, Combust. Flame 157 (6) (2010) 1111–1121.
[32] M.A. Gibson, J. Bruck, Efficient exact stochastic simulation of chemical systems with many species and many channels, J. Phys. Chem. A 104 (9) (2000) 1876–1889.
[33] L.O. Jay, A. Sandu, F.A. Potra, G.R. Carmichael, Improved quasi-steady-state-approximation methods for atmospheric chemistry integration, SIAM J. Sci. Comput. 18 (1) (1997) 182–202.
[34] J.G. Verwer, D. Simpson, Explicit methods for stiff odes from atmospheric chemistry, Appl. Numer. Math. 18 (1–3) (1995) 413–430.
[35] J. Hammersley, Monte Carlo methods, Springer Science & Business Media, 2013.
[36] B. Zhang, J.-H. Wang, A short note on the counter-intuitive spurious behaviors in stiff reacting flow, J. Comput. Phys. 291 (2015) 52–59.
[37] D.J. Higham, Modeling and simulating chemical reactions, SIAM Rev. 50 (2) (2008) 347–368.
[38] D.J. Wilkinson, Stochastic modelling for systems biology, CRC Press, 2011.
[39] M. Ó Conaire, H.J. Curran, J.M. Simmie, W.J. Pitz, C.K. Westbrook, A comprehensive modeling study of hydrogen oxidation, Int. J. Chem. Kinet. 36 (11) (2004) 603–622.
[40] V.P. Zhukov, Verification, validation, and testing of kinetic mechanisms of hydrogen combustion in fluid-dynamic computations, ISRN Mech. Eng. 2012 (2012) 1–11.
[41] F. Diegelmann, S. Hickel, N.A. Adams, Three-dimensional reacting shock–bubble interaction, Combust. Flame 181 (2017) 300–314.

[42] R.J. Kee, F.M. Rupley, J.A. Miller, Chemkin-II: a Fortran chemical kinetics package for the analysis of gas-phase chemical kinetics, Technical Report, Sandia National Labs, Livermore, CA (USA), 1989.
[43] R.J. LeVeque, R.J. Leveque, Numerical methods for conservation laws, 132, Springer, 1992.
[44] T.D. Aslam, D.S. Stewart, Detonation shock dynamics and comparisons with direct numerical simulation, Combust. Theory Model. 3 (1) (1999) 77–101.
[45] M. Short, J.J. Quirk, C.D. Meyer, C. Chiquete, Steady detonation propagation in a circular arc: a detonation shock dynamics model, J. Fluid Mech. 807 (2016) 87–134.
[46] S. Gordon, B.J. McBride, Computer program for calculation of complex chemical equilibrium compositions and applications, 1, National Aeronautics and Space Administration, Office of Management, Scientific and Technical Information Program, 1994.

B.2 Paper II

Jianhang Wang, Shucheng Pan, Xiangyu Y. Hu, Nikolaus A. Adams

A species-clustered splitting scheme for the integration of large-scale chemical kinetics using detailed mechanisms

In *Combustion and Flame*, Volume 205, 2019, pp. 41-54, DOI: `https://doi.org/10.1016/j.combustflame.2019.03.036`.

Contribution: My contribution to this work was the development of the method and the corresponding computer code for its implementation. I performed simulations and analyzed the results, and wrote the manuscript for the publication.

Combustion and Flame 205 (2019) 41–54

Contents lists available at ScienceDirect

Combustion and Flame

journal homepage: www.elsevier.com/locate/combustflame

A species-clustered splitting scheme for the integration of large-scale chemical kinetics using detailed mechanisms

Jian-Hang Wang, Shucheng Pan*, Xiangyu Y. Hu*, Nikolaus A. Adams

Chair of Aerodynamics and Fluid Mechanics, Department of Mechanical Engineering, Technical University of Munich, Garching 85748, Germany

ARTICLE INFO

Article history:
Received 9 November 2018
Revised 21 January 2019
Accepted 25 March 2019

Keywords:
Ordinary differential equations
Implicit solver
Detailed kinetic mechanisms
Operator splitting
Balanced clustering
n-heptane/n-hexadecane ignition

ABSTRACT

In this study, a species-clustered integrator for chemical kinetics with large detailed mechanisms based on operator-splitting is presented. The ordinary differential equation (ODE) system of large-scale chemical kinetics is split into clusters of species by using graph partition methods which have been intensely studied in areas of model reduction, parameterization and coarse-graining, e.g., diffusion maps based on the concept of Markov random walk. The definition of the weight (similarity) matrix is application-dependent and follows from chemical kinetics. Each species cluster is integrated by the variable-coefficient ODE solver VODE. The theoretically expected speedup in computational efficiency is reproduced by numerical experiments on three zero-dimensional (0D) auto-ignition problems, considering detailed hydrocarbon/air combustion mechanisms at varying scales, from 53 species with 325 reactions of methane to 2115 species with 8157 reactions of n-hexadecane. Optimal clustering weighing both prediction accuracy (for ignition delay and equilibrium temperature) and computational efficiency is implied with the clustering number $N = 2$ for the 53-species methane mechanism, $N = 4$ for the 561-species n-heptane mechanism and $N = 8$ for the 2115-species n-hexadecane mechanism.

1. Introduction

Gasoline, diesel and jet fuels, particularly those derived from petroleum sources, are composed of hundreds of components [1]. As the number of hydrocarbon species grows, so does the dimensionality of kinetic mechanism to model hydrocarbon oxidation. For example, the detailed mechanism for methyl decanoate, a biomass fuel surrogate, consists of 3036 species and 8555 reactions [2,3]. For the accurate prediction of combustion processes such as ignition, extinction and flame propagation, the efficient solution of large-scale detailed chemical kinetics is a key [4], limited, however, by the current computing power. The above-mentioned mechanism is time consuming even for 0D simulations [3], no matter whether using explicit or implicit solvers. This limitation therefore motivates to the development of mechanism reduction methods, e.g., directed relation graph (DRG) based methods [5–8], etc.

Moreover, numerical stiffness due to large differences of reaction timescales exists, so that the high-cost implicit ODE solvers, e.g., VODE [9] and DASAC [10], requires robust use of reasonably large timesteps [4]. Since Jacobian evaluation and factorization in implicit solvers dominate the computational cost for compressible and reactive CFD [11], the CPU time scales with the number of species in the mechanism as $\mathcal{O}(N^2)$ to $\mathcal{O}(N^3)$ with dense matrix operations [12,13].

For general multi-dimensional reactive flows, operator splitting has been widely used to separate chemistry integration from that of transport processes to reduce computational efforts [14–18]. Xu et al. [4] and Gao et al. [19] adaptively separate the dynamic system into a fast operator including only fast reactions and a slow operator including slow reactions and the transport process, with each part being imposed of an implicit solver and a more efficient explicit solver, respectively. For the chemical dynamics only, Nguyen et al. [20] aiming at preserving mass conservation and positivity solves each chemical reaction after splitting the multi-reaction system into decoupled processes. Pan *et al.* [21] introduce the graph/network partition into large-scale stochastic and mass concentration based chemical networks.

The quadric/cubic scaling of CPU time to mechanism size using implicit ODE solvers implies that the computational cost of solving a sequence of smaller subsystems ought to be much less than that of solving the entire system in one step. Therefore, unlike the above use of operator splitting in decoupling two or more physical processes, we start with splitting the large-scale chemical kinetics in terms of the involved species. Once the participating species of the large mechanism have been clustered into subsets of a smaller and equal size, an implicit solver can be applied to

* Corresponding author.
E-mail addresses: jianhang.wang@tum.de (J.-H. Wang), shucheng.pan@tum.de (S. Pan), xiangyu.hu@tum.de (X.Y. Hu), nikolaus.adams@tum.de (N.A. Adams).

https://doi.org/10.1016/j.combustflame.2019.03.036
0010-2180/

each group with significantly reduced matrix dimension. To minimize the splitting error, diffusion maps [22–24] are utilized to analyze the pairwise interaction relations of species by constructing a weight or similarity matrix of chemical kinetics, such that strongly interacting and mutually dependent species can be clustered into the same group. To partition the species into equal clusters, a balanced k-means algorithm [25] is employed.

The paper is organized as follows. In Section 2, we introduce the ODE system of chemical kinetics and formulate the species-clustered solver illustrated by a simple model example. Results from the proposed method for three detailed mechanisms in varying scales are presented and discussed in Section 3, considering the 0D auto-ignition problem at constant-volume and adiabatic conditions. Conclusions are drawn in Section 4.

2. Methodology

2.1. Operator splitting by species for chemical kinetics

The ODE system for chemical kinetics under adiabatic and constant-volume conditions can be expressed as

$$\frac{\mathrm{d}y_i}{\mathrm{d}t} = \frac{\dot{\omega}_i}{\rho}, \quad i = 1, \ldots, N_s, \tag{1}$$

where y_i and $\dot{w}_i$ denote the mass fraction and the total production rate of species i, respectively, in a mechanism consisting of N_s species and N_r reactions. Each reaction can be written as

$$\sum_{i=1}^{N_s} \nu_{ji}^f X_i \Longleftrightarrow \sum_{i=1}^{N_s} \nu_{ji}^b X_i, \quad j = 1, \ldots, N_r, \tag{2}$$

where ν_{ji}^f and ν_{ji}^b are the stoichiometric coefficients of species i appearing as a reactant and as a product in reaction j. The total production rate of species i in Eq. (1) is the sum of the production rate from each single elementary reaction

$$\dot{\omega}_i = W_i \sum_{j=1}^{N_r} (\nu_{ji}^b - \nu_{ji}^f) \left[k_j^f \prod_{l=1}^{N_s} \left[\frac{\rho_l}{W_l}\right]^{\nu_{jl}^f} - k_j^b \prod_{l=1}^{N_s} \left[\frac{\rho_l}{W_l}\right]^{\nu_{jl}^b} \right], \tag{3}$$

with k_j^f and k_j^b denoting the forward and backward reaction rates of each chemical reaction, and W_i being the molecular weight of the ith species and the partial density $\rho_l = y_l \rho$. With fixed total density and constant specific internal energy, the equation of state (EoS) for an ideal gas mixture can be used to determine the evolution of mixture temperature and thus to close the system.

The solution vector $\Phi = \{y_1, \ldots, y_{N_s}\}^T$ at time level n is integrated through the above ODE system for one timestep of Δt with the implicit solver VODE [9] to obtain

$$\Phi^{n+1} = R_{\Delta t}(\Phi^n). \tag{4}$$

The operator R represents the time integration by VODE. Upon operator splitting by species, we obtain

$$\Phi^{n+1} = R_{\Delta t}(\Phi_1^n) \circ R_{\Delta t}(\Phi_2^n) \cdots \circ R_{\Delta t}(\Phi_N^n), \tag{5}$$

corresponding to the Lie–Trotter splitting scheme [26], where Φ_k denotes the mass fractions of the species clustered in subset S_k out of N subsets in total. Clustering of species in each subset obeys

$$\begin{aligned} &\Phi = \{\Phi_1, \ldots, \Phi_N\}^T, \\ &S = \cup_{k=1}^N S_k, \ \ S_i \cap S_j = \emptyset \text{ if } i \neq j. \end{aligned} \tag{6}$$

Each subset of species cluster should have no overlap with others, and an almost equal number of species in each subset is assumed varying by at most one species, which requests a balanced partition/clustering algorithm [25]. The extension to higher-order splitting of Strang [27] is straightforward but inevitably more time consuming. Recalling that the scaling of computational cost to the number of species or the size of the kinetic mechanism involved using an implicit solver such as VODE is [4]

$$t_{\mathrm{CPU}} \sim \mathcal{O}\left(N_s^2\right) \text{ to } \mathcal{O}\left(N_s^3\right), \tag{7}$$

the total cost after species splitting can be reduced to

$$t_{\mathrm{CPU}}^{'} \sim \mathcal{O}\left(\frac{N_s^2}{N}\right) \text{ to } \mathcal{O}\left(\frac{N_s^3}{N^2}\right), \tag{8}$$

assuming equal computational consumption for each subsystem after species-splitting. A large mechanism consisting of ten thousand species, e.g., split the system into ten clusters with the Lie–Trotter scheme, results in a computational speedup of ten to a hundred times, without the need for additional sparse matrix techniques [12,13,28].

The essence of operator splitting by species for chemical kinetics lies in clustering species into subsets, each corresponding to a sub-ODE-system to be integrated by VODE or other implicit solvers. The merits of operator splitting by species are improved speedup of computational efficiency without changing the implicit solver, fast convergence and numerical stability [21].

2.2. Graph-based species clustering

A chemical reaction system with multiple species and reactions can be translated to a bi-partite graph [29], in which two sets of nodes represent the chemical species and reactions. Herein, we simply consider a finite graph consisting of the chemical species only and the non-linear coupling between pairs of species through reactions is abstracted as undirected edges linking every two nodes of species. For the sake of illustration, we consider $N_s = 6$ six species, {*A, B, C, D, E, F*}, and six first-order one-way reactions, i.e.

$$\begin{aligned} &A \xrightarrow{k_1} C, \ \ B \xrightarrow{k_2} C, \ \ C \xrightarrow{k_3} B, \\ &D \xrightarrow{k_4} C, \ \ E \xrightarrow{k_5} D, \ \ F \xrightarrow{k_6} D, \end{aligned} \tag{9}$$

where $k_1, \ldots, k_6$ are constant reaction rates. The exact solution for this problem can be easily obtained using symbolic computations of MATLAB® [30].

First we construct the graph of species, Fig. A.1(a). We may have two different clusterings I and II with two subsets ($N = 2$). Clustering I in Fig. A.1(b) is obtained by cutting off the link between species *C* and *D*. The strong couplings within clusters {*A, B, C*} and {*D, E, F*} are preserved. Upon clustering loosely coupled {*A, E, F*} together and leave the rest to compose the other cluster, we obtain Clustering II. The distance in the graph between (*A, E*) or (*A, F*) is remote as they are separated by two other species. The difference of the two clusterings also reflects in the rearranged Jacobian matrices by the order of splitting and clustering as shown in Fig. A.1(c) and (d). We can see that for Clustering I, when solving the cluster of {*A, B, C*} first, only the effect of species *D* is considered as constant since k_4 is not within the sub-Jacobian matrix. When solving the other cluster {*D, E, F*} subsequently, species *A, B* and *C* have no effect due to the corresponding zero entries. In total, the splitting error is attributed to only one element in the Jacobian, i.e. the k_4 block (red color) in Fig. A.1(c). For Clustering II, the solution of the first cluster {*A, E, F*} introduces no splitting error, whereas errors will occur when solving the cluster {*B, C, D*}, due to first-order approximation of $k_1 y_A$ for the production of species *C* and $k_5 y_E + k_6 y_F$ for the production of species *D*.

Numerical tests, in Fig. A.2, show that Clustering I agrees quite well with the exact solution, while Clustering II underestimates both the mass fractions of species *C* and *D*. This observation is in agreement with the previous discussion about operator splitting.

Given a prescribed number of clusters *N*, there are many possible clustering combinations. One simple strategy is to cluster the

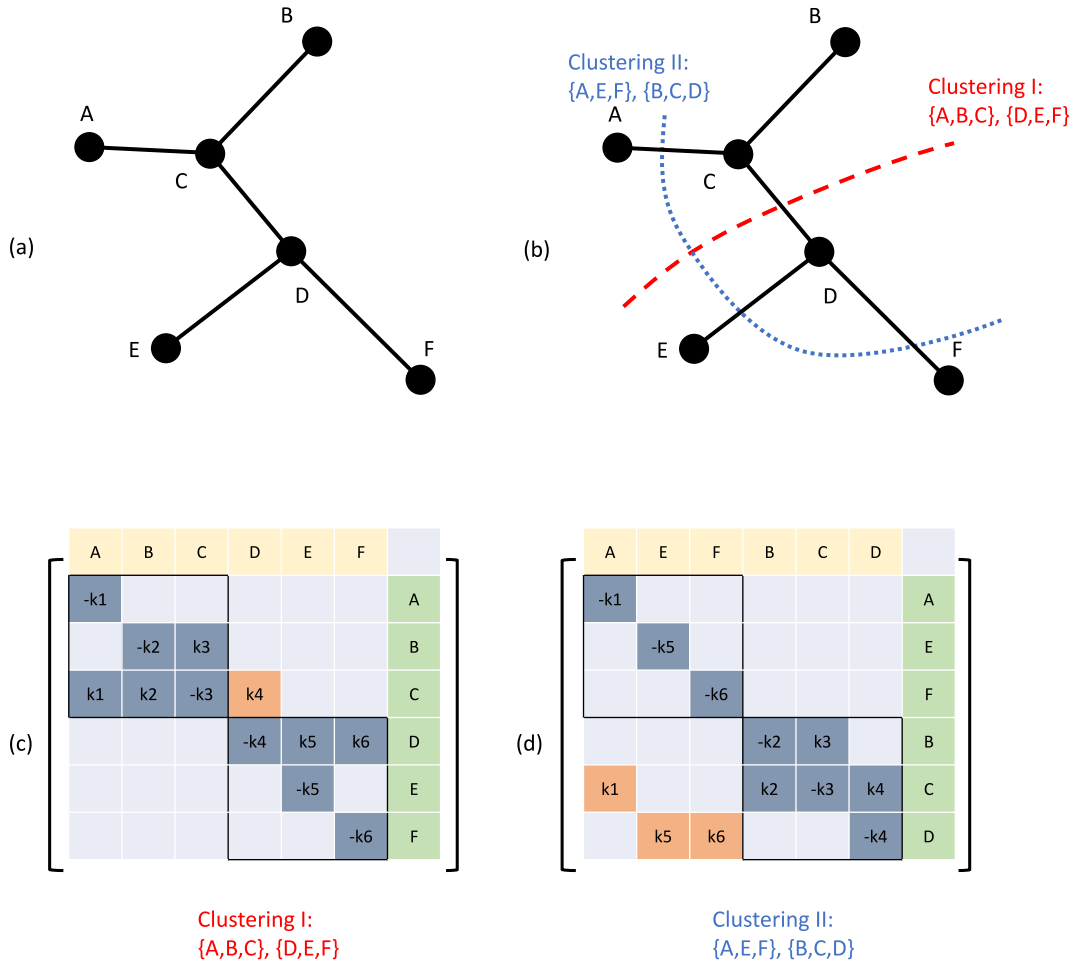

Fig. A.1. Reaction system example for species clustering. (a) Each node represents one species in {*A, B, C, D, E, F*}, and the edge, e.g., *e*(*A, C*), indicates that linked two species participate in at least one reaction as reactant or product; (b) two equal-sized clusterings are easily obtained as ({*A, B, C*}, {*D, E, F*}) and ({*A, E, F*}, {*B, C, D*}) by cutting off corresponding edges; (c) rearranged Jacobian matrix in the order of Clustering I; (d) rearranged Jacobian matrix in the order of Clustering II.

species according to species indices appearing in the mechanism. Another very promising strategy is to cluster all 'close' nodes in the graph into a subset, corresponding to having species with strong interactions in the same cluster. In this paper, we introduce diffusion maps [22–24] as a non-linear technique for dimensionality reduction, data set parameterization and clustering, to serve the purpose.

Let $G = (\Omega, W)$ be a finite graph of n nodes, where the weight matrix $W = \{w(x, y)\}_{x,y\in\Omega}$ is symmetric and component-wise positive [23]. The definition of weight matrix needs to reflect the degree of affinity of nodes x and y. Diffusion maps start with a user-defined weight matrix and utilize the idea of Markov random walk to describe the connectivity of nodes through a diffusion process. For technical details of diffusion maps, we refer to [22–24].

For the above reaction system, we define, with the help of species graph in Fig. A.1(a), the weight matrix W by

$$w(x,y) = \begin{cases} max(k_j), & \text{if } x \text{ and } y \text{ both participate in reaction } j, \\ \epsilon, & \text{otherwise,} \end{cases} \tag{10}$$

where ϵ takes a small positive value to avoid zero entries, e.g., $\epsilon = 10^{-12}$. The diagonal elements in the weight matrix, $w(x, x)$, can be defined as

$$w(x,x) = max(w(x,y)_{y\neq x}). \tag{11}$$

In combination with the reaction rates given in Fig. A.2, the weight matrix obtained by the above definition is shown in Fig. A.3. Using diffusion maps to analyze the graph based on our defined weight matrix, we can project the set of species into a diffusion space with at most n dimensions, where the pairwise distance reveals the connectivity between two species. In Fig. A.3, it is shown that the species are projected onto a x_1x_2 plane using the first two dimensions of the diffusion space. We can see that species *A, B* and *C* almost collapse into one point and locations of species *D, E* and *F* in the x_1 direction (which is also the first and dominant dimension) are also very close to each other. Their coordinates in the second dimension separate the three species. However, the centroids of subset {*A, B, C*} and subset {*D, E, F*} are far from each other. Accordingly, a straightforward clustering using the k-means algorithm (setting $k \equiv N = 2$) can be easily obtained, i.e. ({*A, B, C*}, {*D, E, F*}). This clustering from diffusion maps is the same as the previous Clustering I, indicating that it is the optimal case of two clusters for the reaction system above with minimum splitting errors. In Fig. A.2, we can also observe that exact mass conservation is violated by operator splitting with first-order convergence rate using the Lie–Trotter scheme. However, the optimal Clustering I has a significantly lower mass conservation error than Clustering II. An additional treatment for the correction of mass-conservation errors as in [11] can be applied. In this illustrative example, it should be noted that the underlying fact of $k_4 = 1$ being quite small benefits Clustering I through the weight matrix W in Eq. (10). If k_4 becomes larger, both the previous manual clustering and the current diffusion maps based clustering would be different, with the coupling between species *C*

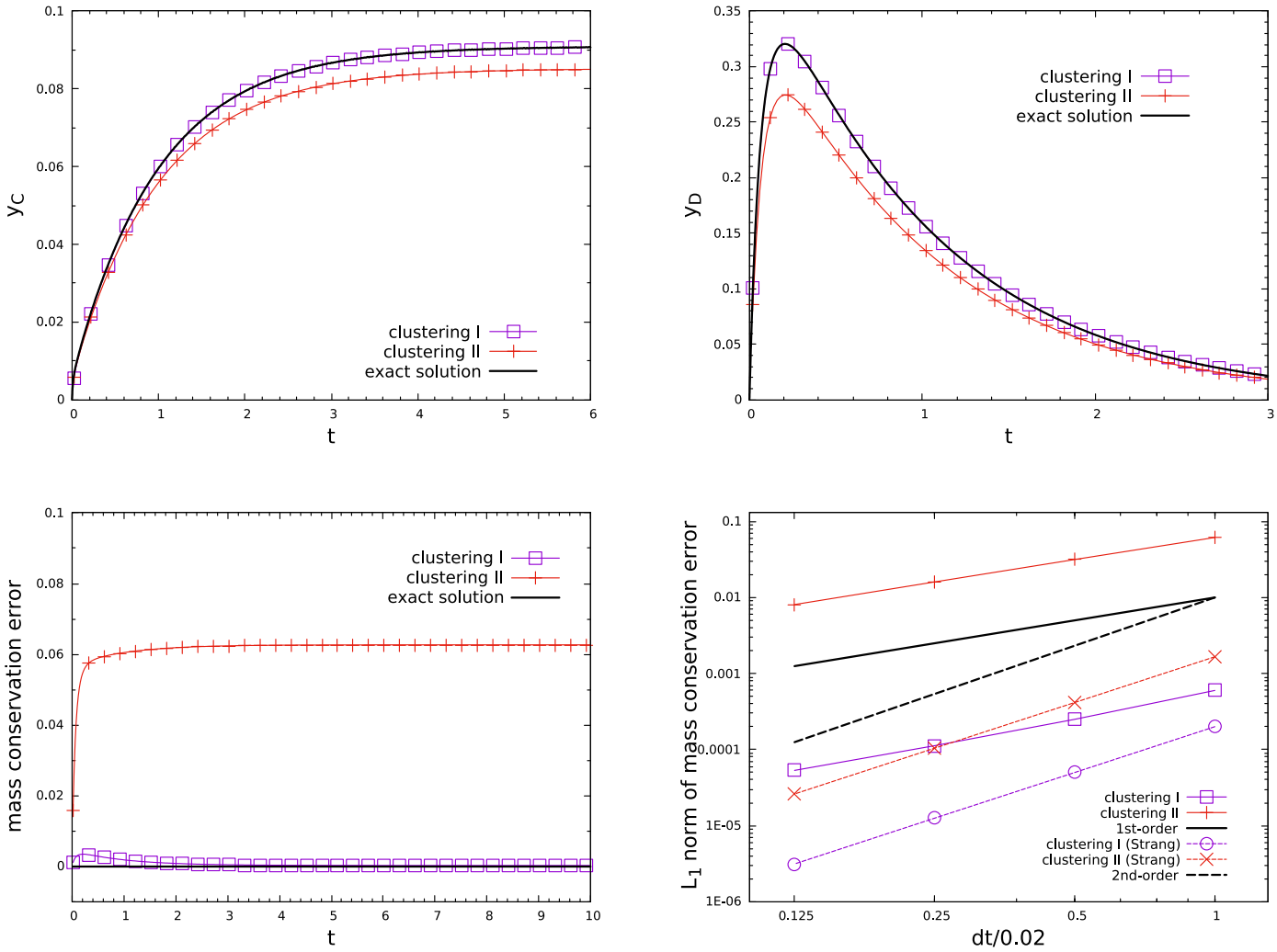

Fig. A.2. Numerical integration results with two clusterings by Lie–Trotter and Strang splittings, compared with the exact solution. Reaction rates are $k_1 = 1, k_2 = 10, k_3 = 100, k_4 = 1, k_5 = 10, k_6 = 20$, and the initial condition is $y_A = 0.6, y_E = 0.2, y_F = 0.2$ with zero mass fractions of *B, C, D*. The base timestep size is $\Delta t = 0.02$.

A	B	C	D	E	F	
k1	0	k1	0	0	0	A
0	k3	k3	0	0	0	B
k1	k3	k3	k4	0	0	C
0	0	k4	k6	k5	k6	D
0	0	0	k5	k5	0	E
0	0	0	k6	0	k6	F

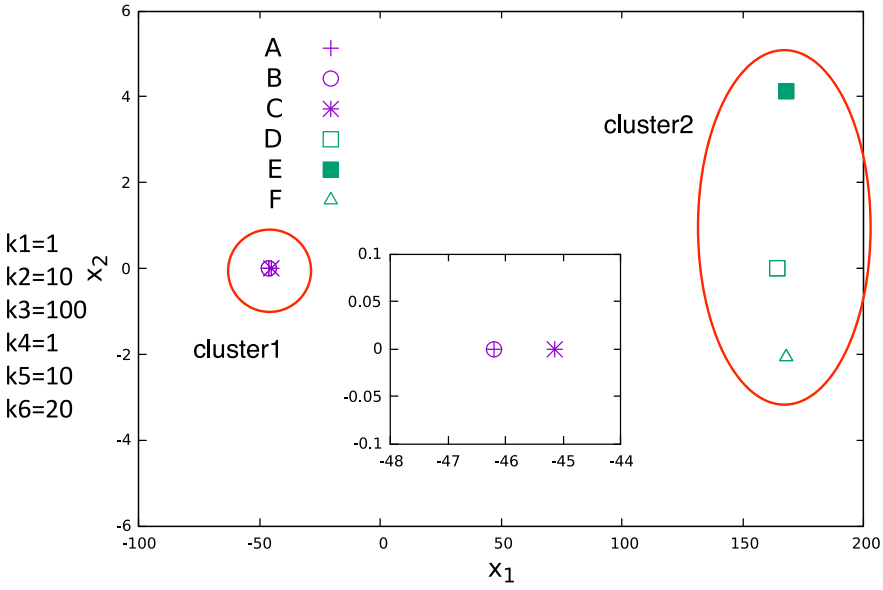

Fig. A.3. Weight matrix of diffusion maps for the reaction system (left); embedding and clustering of species in 2D diffusion space (right).

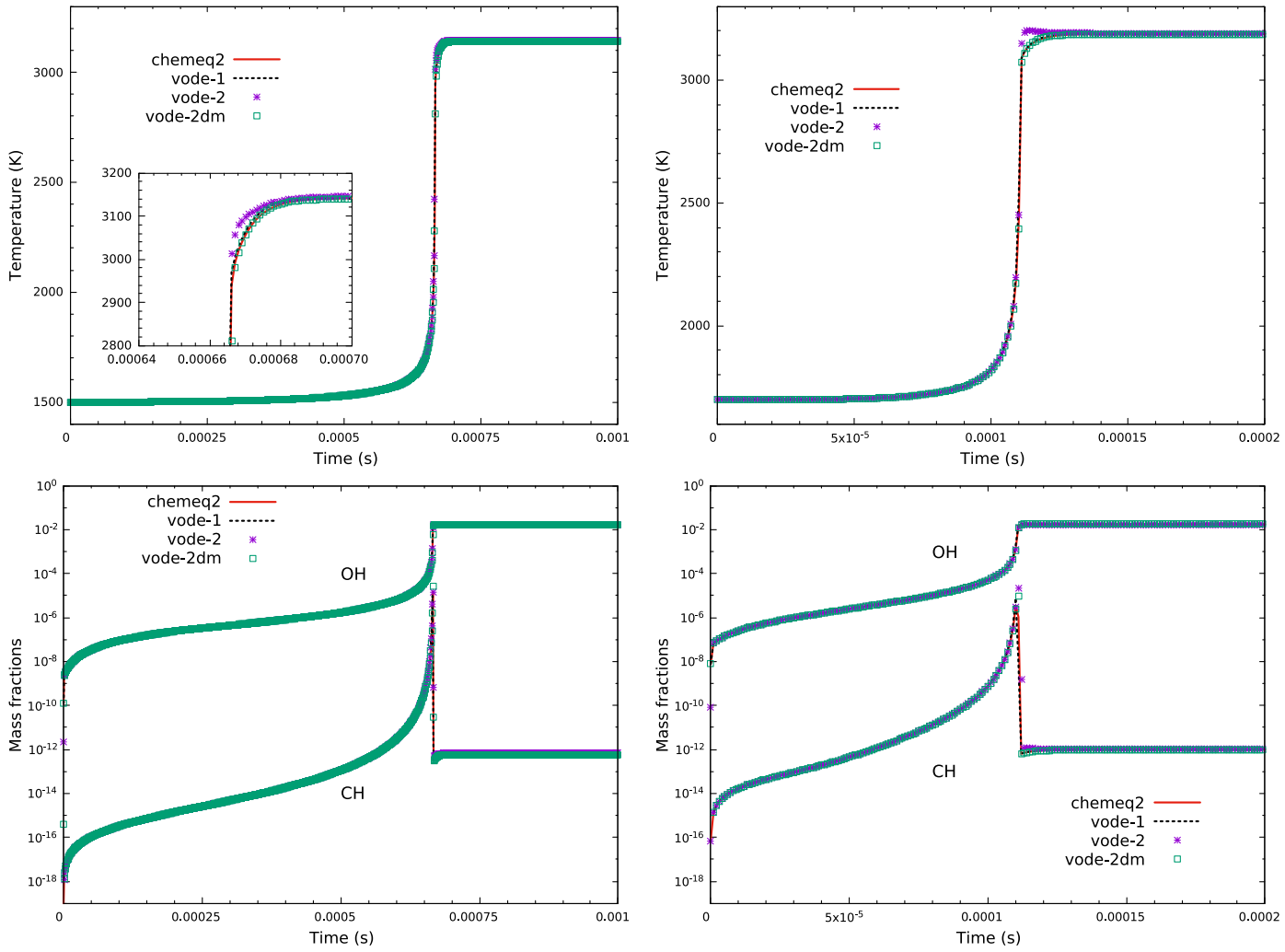

Fig. A.4. Calculated temperature and mass fraction histories for methane/air ignition delay problem in two initial conditions: left column (Case 1) and right column (Case 2).

and D to be preserved and both being clustered into the same subset.

For much more complicated realistic chemical kinetics especially involving fuel combustion mechanisms, reaction rates are not always constant but depend on temperature or even pressure of the mixture. This normally can be expressed by the finite-rate Arrhenius model [31,32] and thus the weight matrix as above should also take into account the varying reaction rates with temperature. Rather than sampling at a single temperature, e.g., the initial temperature of an auto-ignition problem of combustible gas mixtures, we take many temperature samples in order to construct a representative weight matrix. The derived clustering by diffusion maps based on such a weight matrix can be stored and used for other conditions as long as the same mechanism is involved. In such way, the determination of the weight matrix as well as the clustering procedure can be treated as a preprocessing step instead of costly on-the-fly clustering. Since multiple scales of the absolute reaction rates exist, usually spanning several orders of magnitude, logarithmic scaling of the reaction rates can be performed to avoid underestimating the slow reactions. Also, normalization in each row of the matrix relative to the diagonal species is carried out as

$$w(x,y) = \frac{w(x,y)}{w(x,x)}, \tag{12}$$

Table 1
Numbers of species and reactions in detailed mechanisms.

	No. of species	No. of reactions
CH_4	53	325
n-C_7H_{16}	561	2539
n-$C_{16}H_{34}$	2115	8157

and

$$w(x,y) = max(w(x,y), w(y,x)) \tag{13}$$

for all species pairs is further checked to guarantee the symmetry of weight matrix in the diffusion maps.

3. Numerical results and discussion

In this section with numerical experiments, we consider three detailed mechanisms for hydrocarbon fuel combustion: the GRI-Mech 3.0 mechanism for methane (CH_4) [33], the n-heptane (n-C_7H_{16}) mechanism (Version 2) [34,35], and the n-hexadecane (n-$C_{16}H_{34}$) mechanism [36]. The dimensions of three mechanisms are listed in Table 1, exhibiting increasing numbers of species and reactions as well as growing computational complexity of time integration. Zero-dimensional auto-ignition of the fuel/air mixture under adiabatic and constant-volume conditions is taken into consideration.

Table 2
Initial conditions for methane/air mixture.

	CH_4–O_2–Ar molar ratio	Temperature (K)	Pressure (atm)
Case 1	9.1–18.2–72.7%	1500	1.8
Case 2		1700	2.04

3.1. Methane/air auto-igniton

The first example considers the ignition delay problem of methane/air mixture. Two different initial conditions [37] are considered as in Table 2. For Case 1, the computation is carried out until $t = 0.001$ s and the timestep size is fixed at $\Delta t = 1 \times 10^{-7}$ s (this timestep size is also adopted for other cases and is comparably large for compressible and reactive CFD analysis). The computation of Case 2 is until $t = 2 \times 10^{-4}$ s. CHEMEQ2 [31] as a popular explicit ODE solver for chemical kinetics is also employed here for reference, together with the implicit solver VODE. In CHEMEQ2, the convergence parameter of the predictor–corrector method is 1×10^{-4}. In VODE, the relative and absolute error thresholds (RTOL and ATOL) are 1×10^{-5} and 1×10^{-13}, respectively. Since the dimension of the methane mechanism is relatively small, we cluster the 53 species into two subsets, and each cluster of species is integrated by VODE by operator splitting as in Eq. (5). Accuracy and convergence of the splitting method using species clustering are examined by this example. Benefits of computational efficiency from operator splitting by species clustering is to be tested by the following two mechanisms of much larger dimensions. As an important parameter to measure the accuracy of mechanism and ODE solver, ignition delay times, t_{ign}, for the two cases can be referred to [37], i.e. $t_{ign} = 666$ ms for Case 1 and $t_{ign} = 110$ ms for Case 2.

To validate operator splitting by species, the results obtained by CHEMEQ2 and VODE with/without species clustering are shown in Fig. A.4, where VODE-1 is without species clustering (that is, all the species are solved in a single set and a single step) while both VODE-2 and VODE-2dm partition the species into two clusters for operator splitting by setting $N = 2$. The difference of clustering is that VODE-2 simply clusters the species in accordance with the species' index in the mechanism (e.g., species of odd or even indexing numbers are clustered in different subsets) while VODE-2dm utilizes diffusion maps for species clustering based on the weight matrix defined in Eqs. (10)–(13), see Appendix A. In general, clustering based on the indices of species can be readily obtained by

$$\text{Species } i \in \begin{cases} \text{cluster } 1: & \text{if } mod(i,N) = 1, \\ \text{cluster } 2: & \text{if } mod(i,N) = 2, \\ \cdots & \\ \text{cluster } N-1: & \text{if } mod(i,N) = N-1, \\ \text{cluster } N: & \text{if } mod(i,N) = 0, \end{cases} \tag{14}$$

where i denotes the ith species in the mechanism and N is the number of clusters by partition. It can be seen that all four solutions give the correct ignition delay times in two cases. For Case 1, VODE-2 overestimates the temperature slightly before it reaches an equilibrium state while VODE-2dm has nearly the same temperature with both CHEMEQ2 and VODE-1. The deficiency of VODE-2 solution is larger in Case 2, which also occurs at the end of the ignition process. Different predictions by VODE-2 and VODE-2dm can be attributed to the splitting error: with diffusion maps, the error in VODE-2dm is smaller than that in VODE-2. This can be illustrated by embedding the clustered species into a diffusion space, as shown in Fig. A.5. As the clustered species are projected into the 3D diffusion space, we can clearly see that the two clusters of species are separated from each other using diffusion maps, which indicates that each cluster is able to preserve the close interactions between coupling species. In particular, for the VODE-2dm clustering, the first species H and the last species CH_3CHO are within the same cluster as the 13th species CH_3, due to the high activity of H which is involved in composition or decomposition reactions with hydrocarbon species such as

$$O + C_2H_5 \Longleftrightarrow H + CH_3CHO,$$
$$H + CH_3(+M) \Longleftrightarrow CH_4(+M).$$

Also, playing a critical role in the mechanism (as it participates in a large number of reactions), H is located at the center of the diffusion map among all the species. On the other hand, species such as NO and NH are clustered into the other subset because they mainly participate in nitrogen-related reactions, with weaker interactions with hydrocarbon species. In contrast, H is clustered into the NH and NO group in the VODE-2 clustering by index. The obtained two clusters merge each other in the diffusion map, and some pairs of two species with short distances are divided into different clusters, leading to larger splitting error with VODE-2 than with VODE-2dm.

We examine convergence of the splitting method by varying the fixed timestep adopted in Fig. A.6. It can be seen that as the timestep decreases the evolution of temperature and mass fractions approach the corresponding profiles at the shortest timestep:

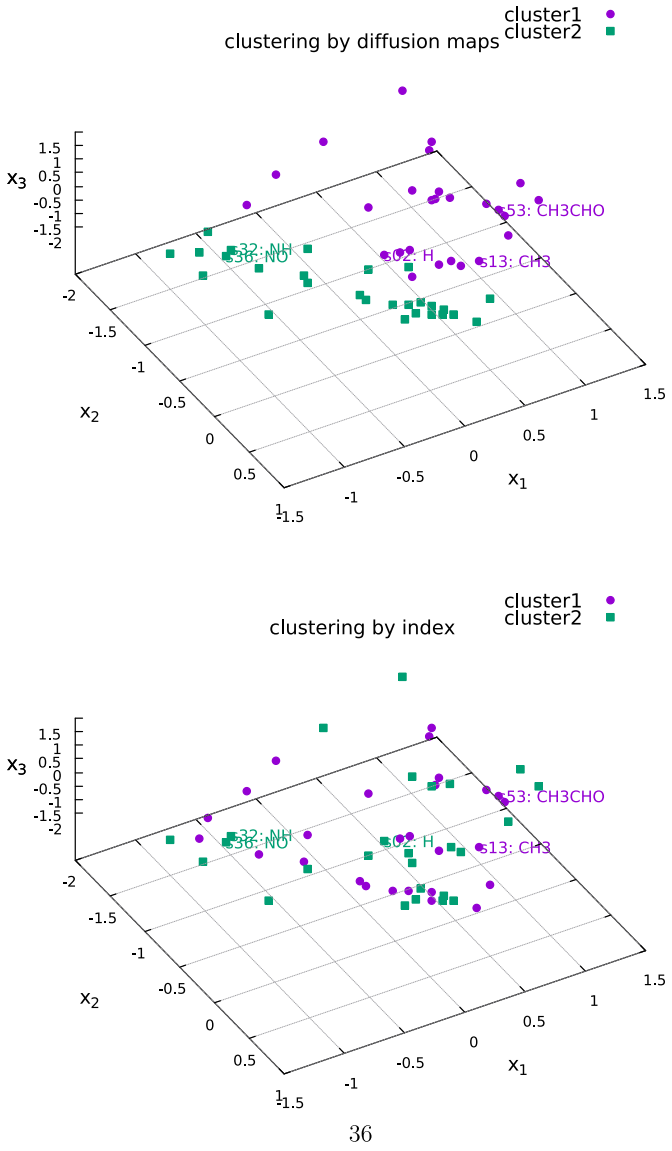

Fig. A.5. Embedding with first three diffusion coordinates of species for methane mechanism.

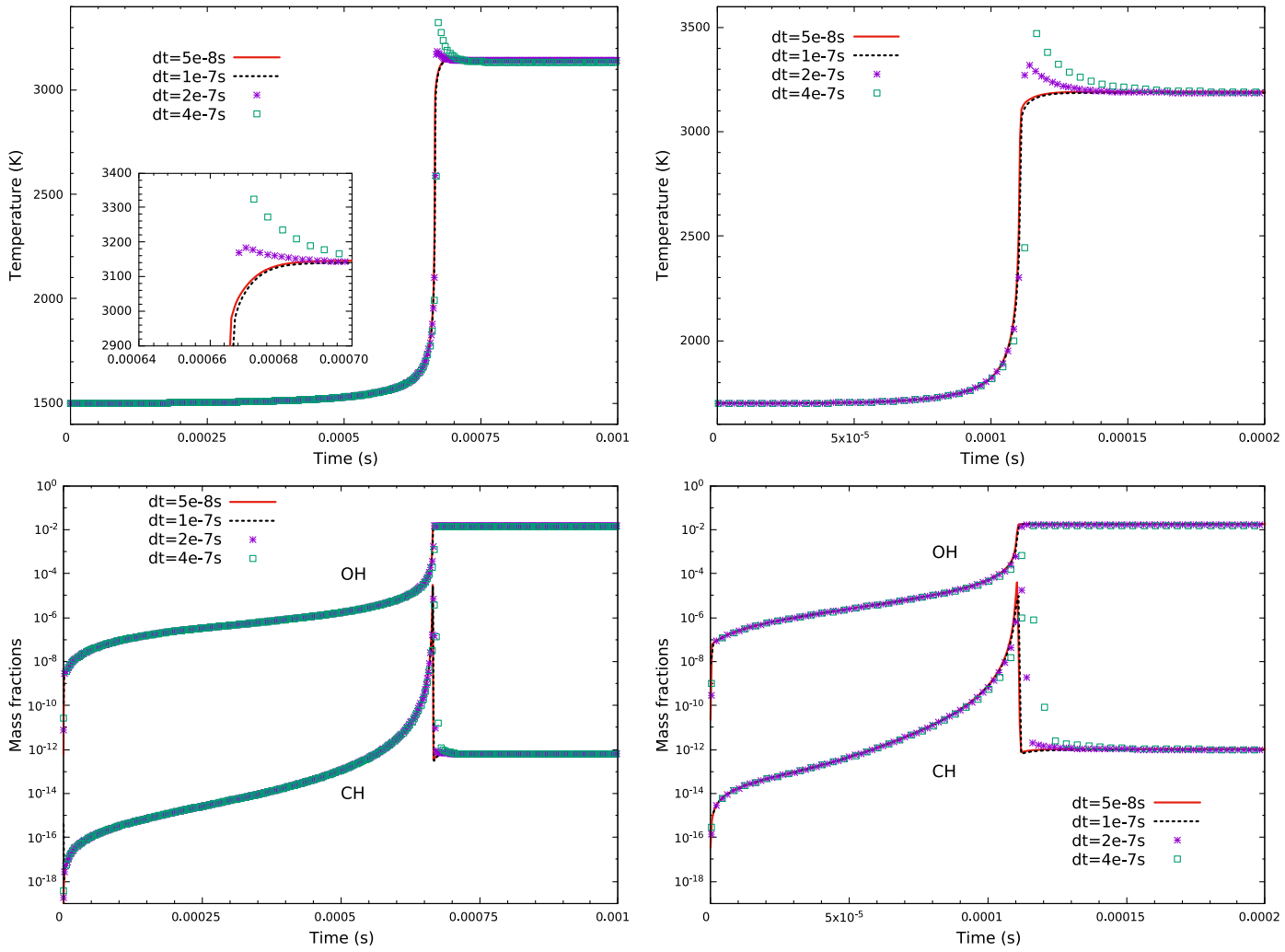

Fig. A.6. Calculated temperature and mass fraction histories for methane/air ignition delay problem by species clustering using varying timesteps in two initial conditions: left column (Case 1) and right column (Case 2).

Table 3
Initial conditions for n-heptane/air mixture.

	n-C_7H_{16}:O_2:N_2 (mole)	Temperature (K)	Pressure (atm)
Case 3	0.09091:1:3.76	1250	10
Case 4			50

spikes in the temperature profiles with large timesteps gradually disappear and the jumps of mass fraction, y_{CH}, tend to sharpen due to sudden consumption during the ignition process. The timestep size of $\Delta t = 1 \times 10^{-7}$ s is verified to be sufficient for integrating the chemical kinetics correctly.

3.2. n-Heptane/air auto-igniton case

The second example considers the n-heptane/air combustion mechanism. Two different initial conditions [38] are considered as in Table 3. For Case 3, the computation is carried out until $t = 4 \times 10^{-4}$ s and the timestep size is fixed at $\Delta t = 1 \times 10^{-7}$ s. The computation for Case 4 is until $t = 1.1 \times 10^{-4}$ s. Without a prior knowledge of the number of clusters which is most suitable and efficient for computing this large-scale mechanism, we choose to split the species by eight clusters using diffusion maps first.

In Fig. A.7, the species clustered VODE result using diffusion maps is compared with that of simple clustering using Eq. (14) by setting $N = 2, 4$ and 8, respectively, and also the results by CHEMEQ2 and non-split VODE. Calculated ignition delay times observed from the temperature histories of Case 3 and 4 by CHEMEQ2, VODE-1 as well as VODE-8dm agree well with each other and also with the numerical results in Ref. [38]. Using the simple clustering algorithm instead of diffusion maps, VODE-2, VODE-4 and VODE-8 obtain the correct ignition delay time for Case 3 while they all severely over-predict the delay of ignition for Case 4. Although the ignition delay time is not very sensitive to the species clustering in Case 3, the post-ignition equilibrium state appears to depend strongly on the quality of the clustering, as we can see that both VODE-2 and VODE-4 overestimate the equilibrium temperature incorrectly and VODE-8 induces an incorrect spike before the temperature reaches the equilibrium state, which is similar with the example of methane combustion. For Case 4, extremely high equilibrium temperatures nearly 4000 K and higher are predicted by VODE-2 and VODE-4, and temperature spike also can be seen for the VODE-8 solution. To explain the over/under-estimation of the equilibrium temperature as well as the delayed ignition times resulted from simple clusterings, we refer to the time-dependent total mass conservation errors in Fig. A.8. As previously stated in Fig. A.2 for the illustrative example, species-clustered splitting might violate total mass conservation because it will inevitably cut off some pathways/channels within coupled species. It is observed that mass conservation

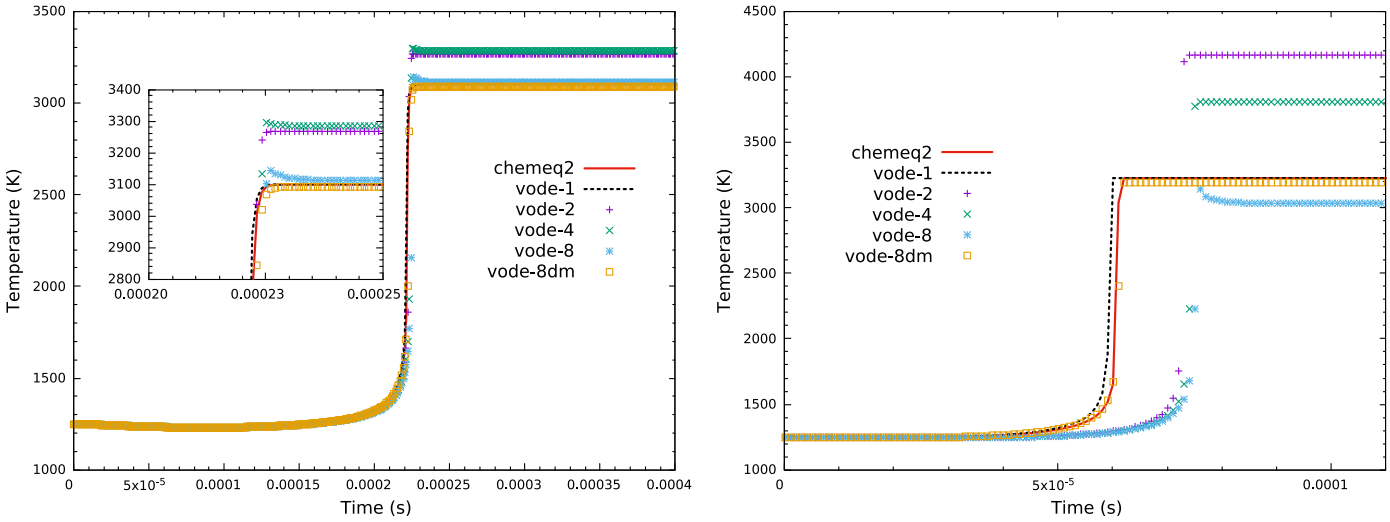

Fig. A.7. Calculated temperature histories for n-heptane/air ignition delay problem in two initial conditions: left column (Case 3) and right column (Case 4).

Table 4
CPU times (s) for clusters at different clustering number N for Case 4.

N	Total									Max.	Min.	Ave.
1	283.407527									283.407527	283.407527	283.407527
2	77.981967	24.689422	53.052336							53.052336	24.689422	38.870879
4	43.336673	11.065684	18.228123	6.475912	7.314687					18.228123	6.475912	10.7711015
8	62.65253	6.059054	5.854662	9.995675	5.960626	5.253225	7.319861	7.693178	14.218079	14.218079	5.253225	7.794295

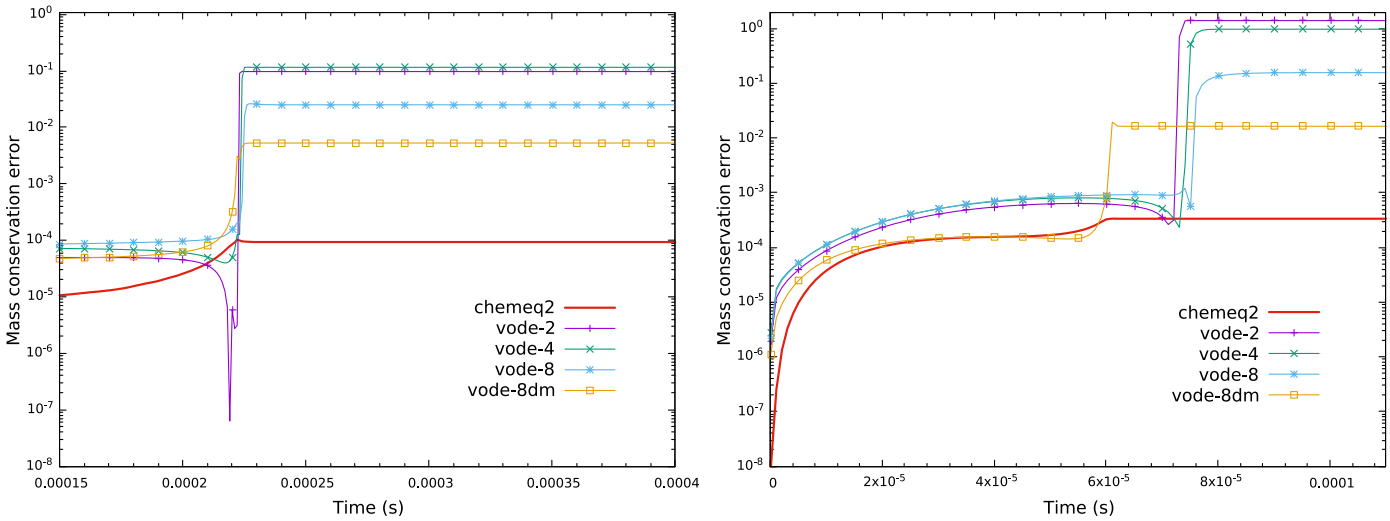

Fig. A.8. Total mass conservation error ($|\sum y_i - 1|$) histories for n-heptane/air ignition delay problem in two initial conditions: left column (Case 3) and right column (Case 4).

errors are very small before ignition, and as ignition triggers them to increase, mass conservation errors reach a relatively high plateau after ignition. We also observe that VODE-8dm yields obviously less conservation errors compared with other simple clusterings, corresponding to less splitting errors. In comparison, CHEMEQ2 produces orders of magnitude smaller errors than the present VODE-8dm and VODE-1 preserves the mass conservation up to roundoff errors (not shown in the figure). Therefore, although the proposed VODE-8dm outperforms other simple clusterings by largely reducing the splitting errors, there is room for further improvement.

In Fig. A.9, we present the species embedding with the first three coordinates, leading to eight clusters of species being scattered but compact in the diffusion space. In comparison, the simple clustering by indices produces disorder species in the diffusion space. The quality of such a simple clustering is therefore expected to be poor, as shown in Fig. A.7. Since the weight matrix is kept unchanged for the same mechanism, the diffusion space containing all the species is also the same and independent of the number of clusters one wants to partition. It is straightforward to further combine the close subsets (every two or four) into a larger cluster so that clustering by $N = 4$ and $N = 2$ can be obtained.

Next, we compare the results denoted by VODE-2dm and VODE-4dm in Fig. A.10. It can be seen that for both cases, the diffusion-map based results all capture the correct ignition delay time and the equilibrium temperature. In particular, the VODE-2dm result performs better than the CHEMEQ2 result, being closer to the non-split VODE-1 result. As the number of partition/splitting decreases, the split VODE results consistently approach the non-split solution, with reduced splitting errors.

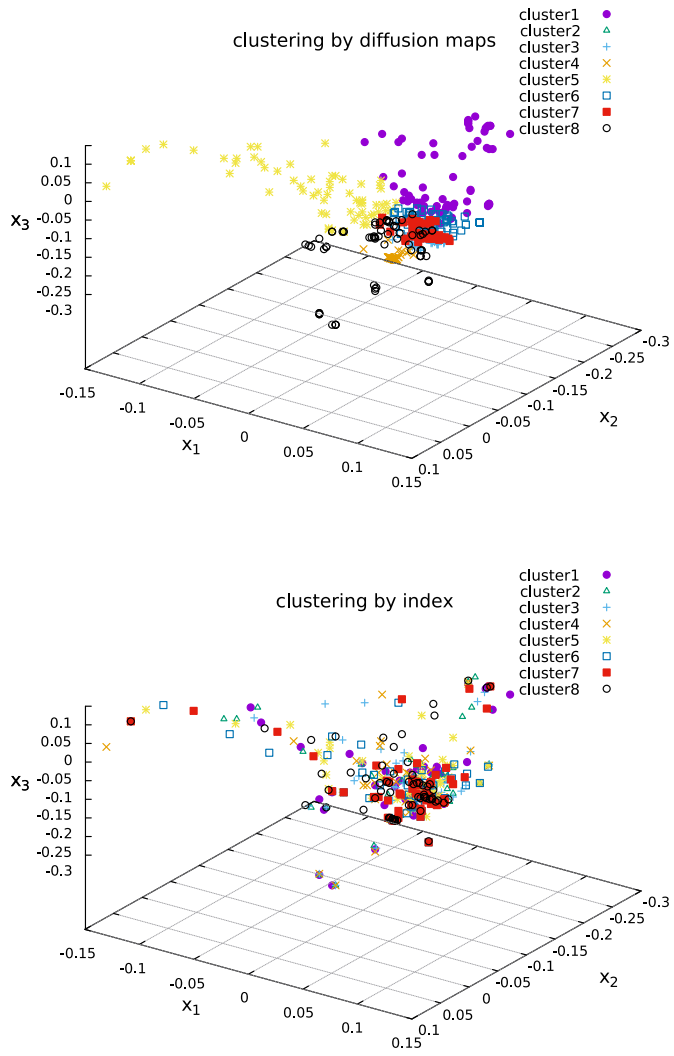

39

Fig. A.9. Species distribution in the diffusion space with first three diffusion coordinates of species for n-heptane mechanism.

In Fig. A.11 (left), we investigate the computational efficiency of different solvers. All the results are normalized based on the CPU time of VODE-1. It is to be noted that in these two cases, the non-split VODE solver is faster than CHEMEQ2. For the split VODE solver using diffusion maps, we can see the reduced CPU times with the increasing number of clusters up to $N = 4$ falls within the region bounded by two theoretical scalings according to Eq. (8). When the number of clusters increases to $N = 8$, the CPU time meets a turning point and the computational efficiency no longer monotonically decreases. Regarding the decay in computational efficiency, two facts should be noted:

- For the decoupled subsystems at a specific number of clusters N, although they share the equal number of species as in Eq. (6), species and their reactions/interactions within each subset are quite different such that Jacobian evaluation and LU factorization as well as the Newton iteration in the VODE solver for each subsystem consume different CPU times. As shown in Fig. A.11 (right) and Table 4, CPU times for subsystems at a given partition number exhibit very large diversity, leading to an imbalance of computational costs among clusters after species-splitting. The non-balanced computational costs contradict the 'ideal' balanced theoretical scaling in Eq. (8);
- When the number of clusters N is large and the dimension of each subsystem is small, CPU time of dense LU factorization ($\propto N_s^3$) no longer dominates the total CPU time. Instead, CPU times of Jacobian evaluation and Newton iteration (both $\propto N_s$) begin to exceed that of dense LU factorization; see in [12,19]. The 'ideal' theoretical scaling in Eq. (8) is no longer valid for large clustering numbers. Therefore, the averaged computational cost of a cluster in Fig. A.11 (right) exhibits high-order decrease rates ($\propto 1/N^2$ to $1/N^3$) for small N and then it linearly decreases with the decreasing number of species within each subsystem $\frac{N_s}{N}$ or the inverse of the clustering number N for larger N.

From Fig. A.11, $N = 4$ may be an optimal clustering number which weighs efficiency and accuracy for the n-heptane ignition problem. With VODE-4dm, we further investigate the ignition delay times of n-heptane oxidation based on a series of varying initial temperatures at 10 and 50 atm, respectively, in Fig. A.12. The negative temperature coefficient (NTC) behavior has been accurately reproduced, in excellent agreement with the results in Fig. 2 of [38].

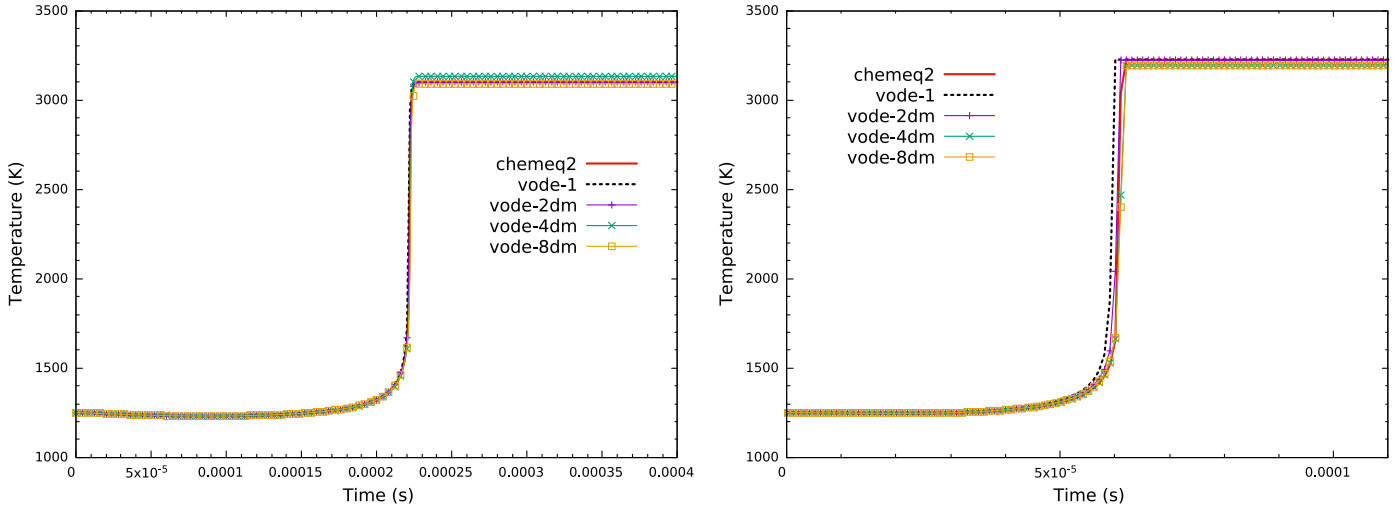

Fig. A.10. Calculated temperature histories for n-heptane/air ignition delay problem by species clustering setting $N = 2, 4, 8$ in two initial conditions: left column (Case 3) and right column (Case 4).

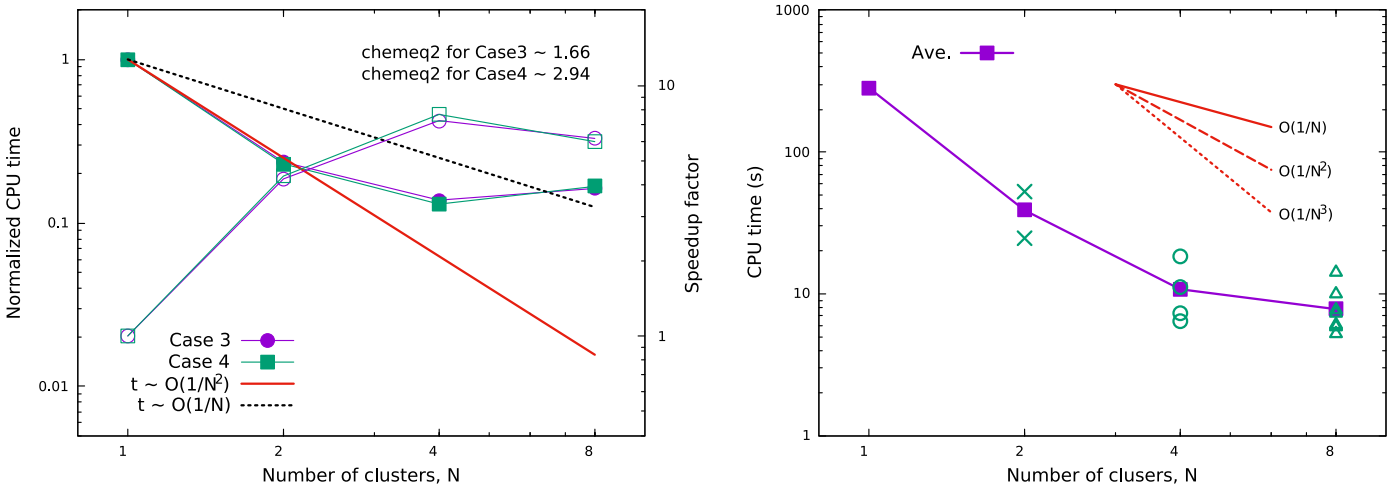

Fig. A.11. Left: normalized CPU time and speedup factor by species clustered VODE with $N = 1, 2, 4, 8$; CPU time is normalized by t/t_{vode1} and speedup factors use hollow symbols. Right: CPU time of each cluster by species clustered VODE with $N = 1, 2, 4, 8$ for Case 4.

Table 5
Initial conditions for n-hexadecane/air mixture.

	$n\text{-}C_{16}H_{34}:O_2:N_2$ (mole)	Temperature (K)	Pressure (bar)
Case 5	0.04082:1:3.76	1111.11	13.5
Case 6		1250	

3.3. *n-Hexadecane/air auto-igniton case*

The third example considers the n-hexadecane/air combustion mechanism with the largest dimension. Two initial conditions [39] are considered as in Table 5. For Case 5, the computation is carried out until $t = 1.1 \times 10^{-3}$ s while it is interrupted for Case 4 at $t = 2.2 \times 10^{-4}$ s with 2200 equal timesteps. We also choose to split the species by eight clusters using diffusion maps.

In Fig. A.13, the species clustered VODE result using diffusion maps is compared with that of simple clustering using Eq. (14) by setting $N = 2, 4$ and 8, respectively, and also with the results by CHEMEQ2 and non-split VODE. Calculated ignition delay times observed from the temperature histories of Case 5 and 6 by CHEMEQ2, VODE-1 as well as VODE-8dm agree well with each other and also numerical results of Ref. [39]. Using simple clustering algorithm instead of diffusion maps, VODE-2, VODE-4 and VODE-8 obtain three increasing ignition delay times for Case 3 and 4. VODE-8 computes the most delayed ignition time, and both

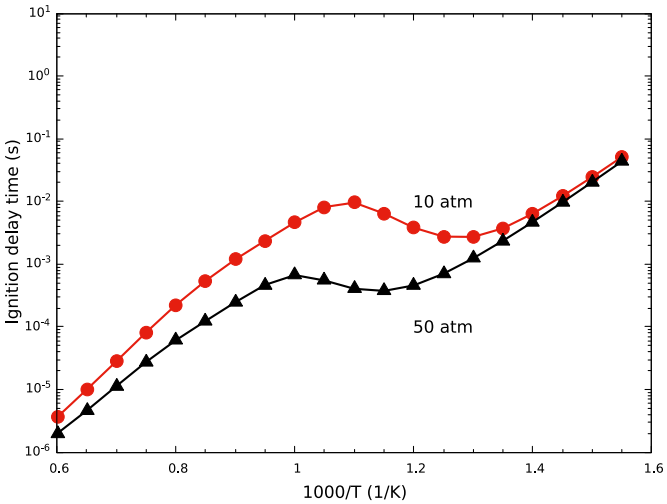

Fig. A.12. Ignition delay times based on different initial temperatures for the stoichiometric n-heptane/air mixture predicted by VODE-4dm.

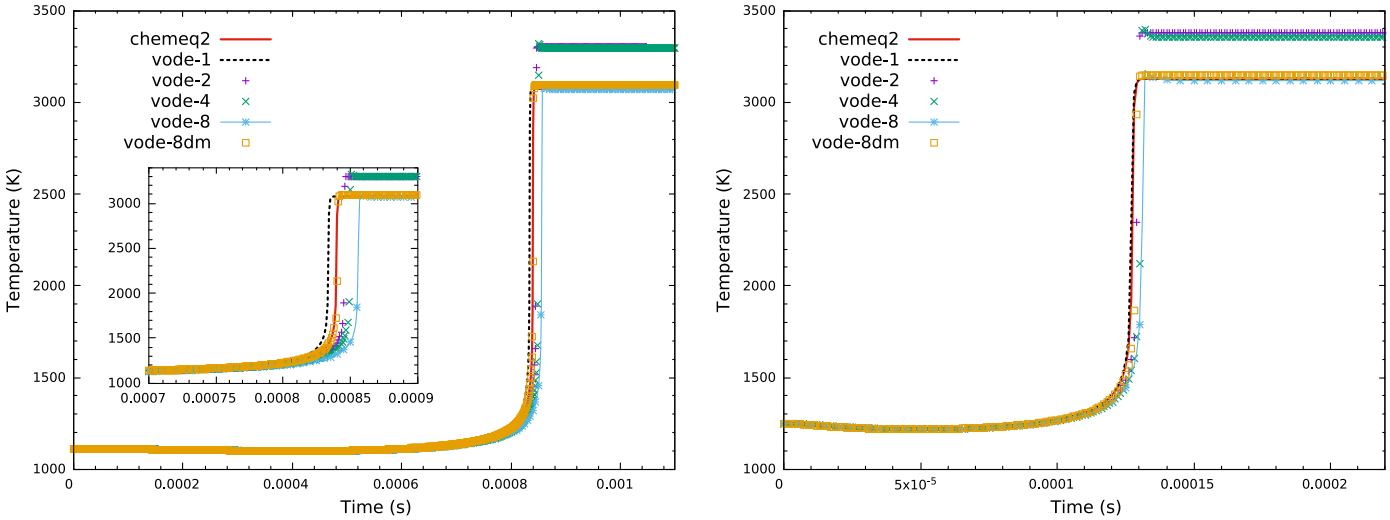

Fig. A.13. Calculated temperature histories for n-hexadecane/air ignition delay problem in two initial conditions: left column (Case 5) and right column (Case 6).

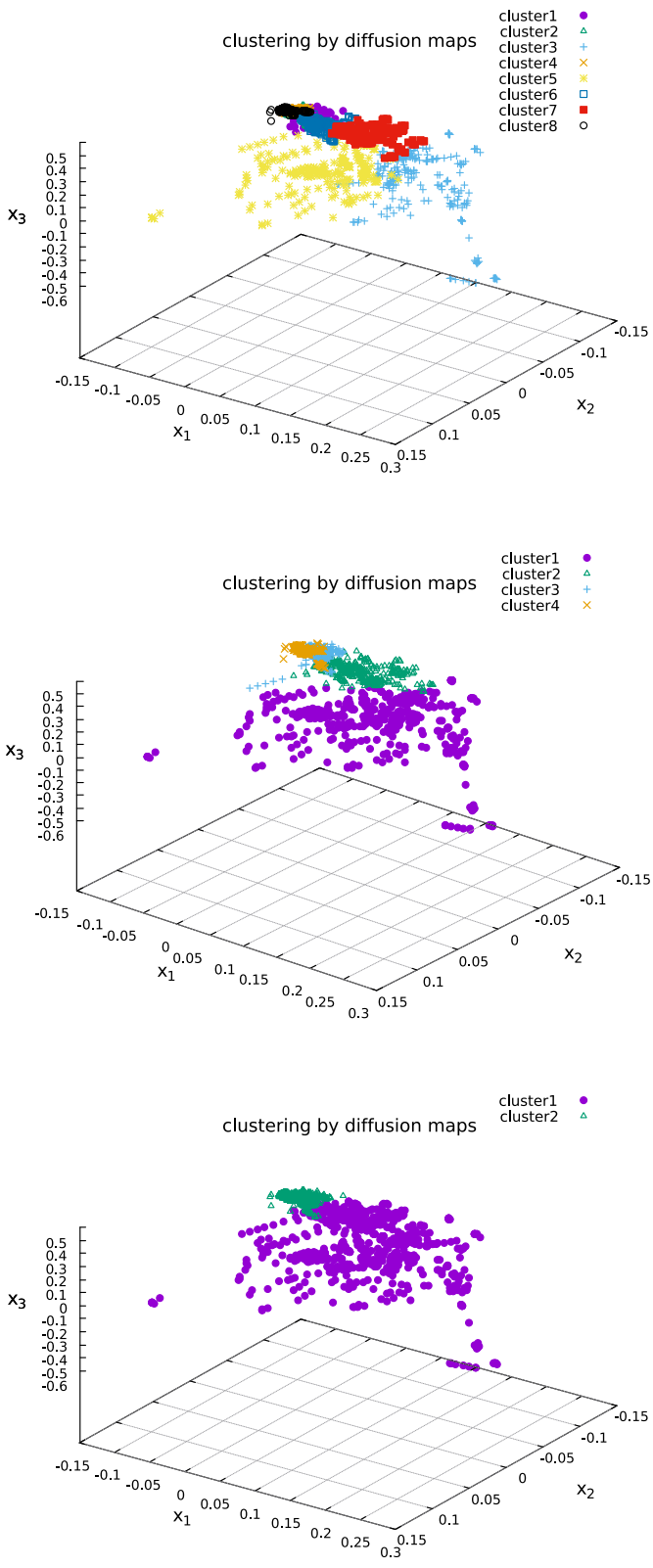

Fig. A.14. Species distribution in the diffusion space with first three diffusion coordinates of species for n-hexadecane mechanism.

VODE-2 and VODE-4 overestimate the equilibrium temperature after ignition incorrectly. In contrast, the VODE-8dm result is comparable with the CHEMEQ2 result in both the ignition and post-ignition process.

In Fig. A.14, we present the species embedding with the first three coordinates, leading to eight/four/two clusters of species being scattered in the diffusion space. It can be seen that the clustering with less number of clusters basically combines the close subsets of species into a larger cluster, as it is manually realized in the n-heptane example. By comparing the five results with different number of clusters up to $N = 16$ based on diffusion maps in Fig. A.15, it is demonstrated that for both cases, the diffusion maps based results all capture the relatively correct ignition delay time and the equilibrium temperature. In particular, the VODE-2dm result performs the best, even better than the CHEMEQ2 result, being closest to the non-split VODE-1 result. The VODE-16dm result slightly overestimates the equilibrium temperature and the ignition time predicted by VODE-8dm is later than that of VODE-4dm by 1×10^{-5} s roughly. Though, as the number of partition/splitting decreases, the split VODE results consistently approach the non-split solution, with reduced splitting errors.

In Fig. A.16 (left), we investigate again the computational efficiency of different solvers. CHEMEQ2 is more efficient than VODE in the first case while in the second case the non-split VODE solver is faster than CHEMEQ2, both solvers with the same order of magnitude of CPU time. Focused on the split VODE solver using diffusion maps, we can see the reduced CPU times as the number of clusters increases up to $N = 8$. The performance in terms of computation efficiency for the clustered VODE solvers when $N = 2$ or 4 even exceeds the theoretical expectation. It can be also explained by the large deviation of computational costs for single subsystems when $N = 2$ or 4. As shown in Fig. A.16 (right) and Table 6, at a given clustering number, the maximum CPU time for a cluster is larger than the minimum CPU time by nearly one order of magnitude in this n-hexadecane case. As a result, the total CPU time mainly depends on the maximum CPU time for a cluster: for the $N = 2$ clustering, its maximum CPU time for one cluster is approximately proportional to $\frac{1}{N^3}$, and it is between $\frac{1}{N^2}$ and $\frac{1}{N^3}$ if the maximum CPU time for one cluster in VODE-4dm is scaled in comparison to that of the non-split VODE-1. When $N = 8$ or 16, the deviation of CPU times for different clusters of equal size becomes smaller and thus its total CPU time, as a sum of CPU times for 8 or 16 clusters, falls into the theoretical zone, which also implies that $N = 8$ or 16 is a reasonable clustering number for the n-hexadecane mechanism.

When the number of clusters increases to $N = 16$, the CPU time no longer decreases, indicating $N = 8$ may be an optimal clustering number from the aspect of efficiency for the n-hexadecane ignition problem. A total speedup factor of around 40 is realized by VODE-8dm for Cases 5 and 6. It is about 50 times faster than CHEMEQ2 for the computation of Case 6.

4. Conclusions

For large-scale chemical kinetics involving many species and reactions, computational efforts needed for time integration usually exceeds linear scaling with the dimension of the kinetic mechanism, especially when implicit ODE solvers are used. To achieve a higher computational efficiency, we have proposed operator splitting to integrate the large system in separate yet consecutive subsystems of the same and smaller dimension. Each subsystem includes a cluster of species decoupled from the other species of the full mechanism and is solved separately, e.g., implicitly by VODE. In order to reduce the inevitable splitting error, diffusion maps are applied to analyze the species graph and to cluster strongly coupled species into the same subsystem, by defining an appropriate

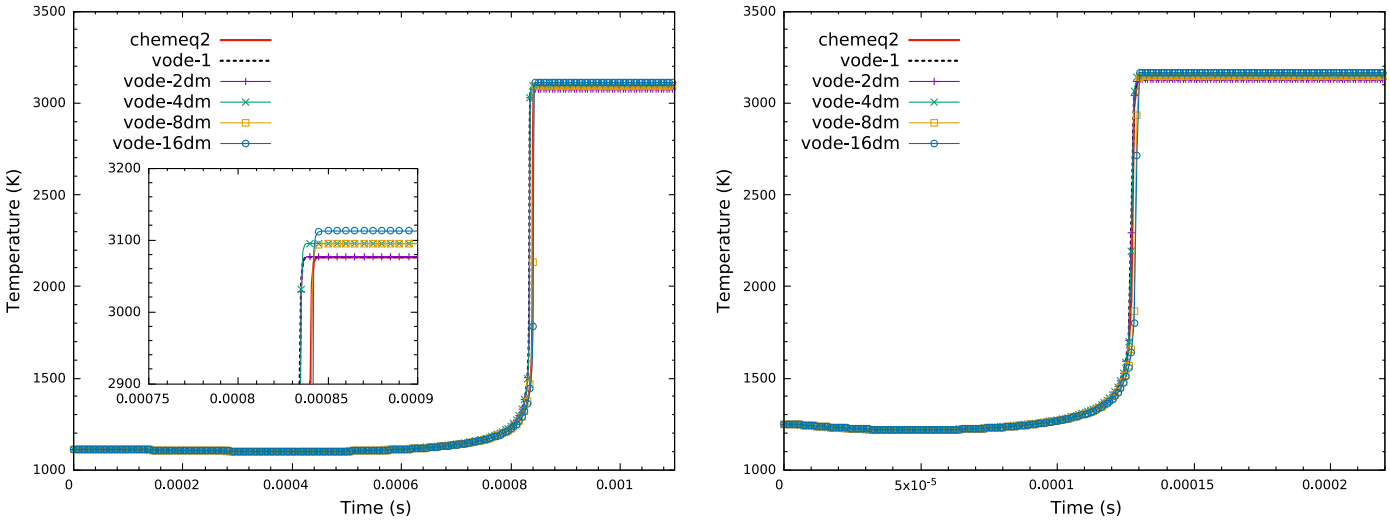

Fig. A.15. Calculated temperature histories for n-hexadecane/air ignition delay problem by species clustering setting $N = 2, 4, 8, 16$ in two initial conditions: left column (Case 5) and right column (Case 6).

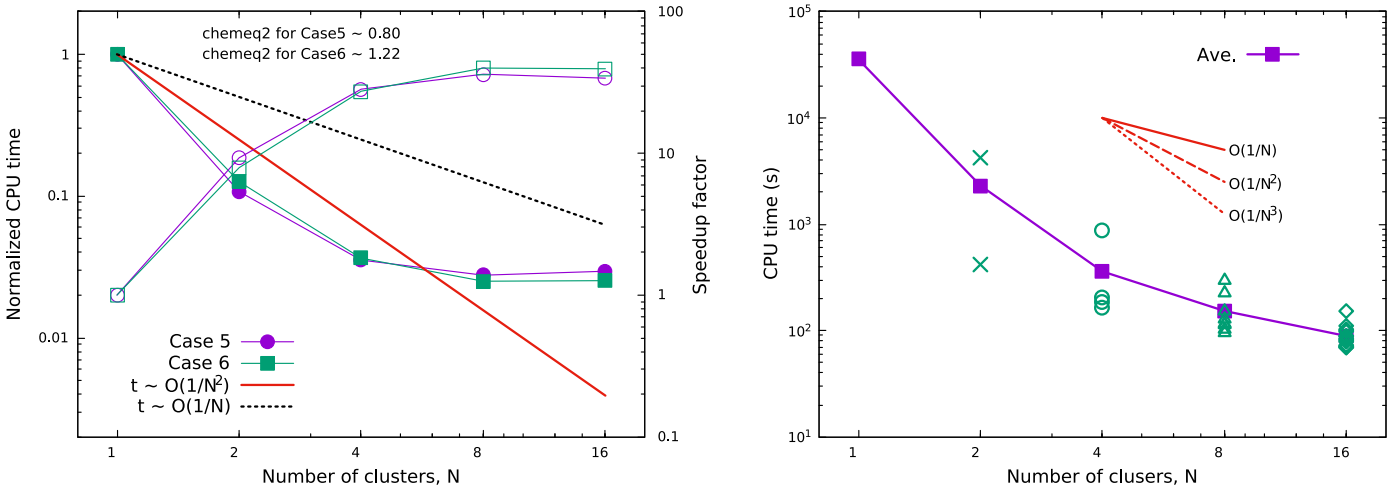

Fig. A.16. Left: normalized CPU time and speedup factor by species clustered VODE with $N = 1, 2, 4, 8, 16$; CPU time is normalized by t/t_{vode1} and speedup factors use hollow symbols. Right: CPU time of each cluster by species clustered VODE with $N = 1, 2, 4, 8, 16$ for Case 6.

Table 6
CPU times (s) for clusters at different clustering number N for Case 6.

N	Total									Max.	Min.	Ave.
1	35658.79841											
2	4627.708055	4199.952252	421.175725							4199.952252	421.175725	2310.563989
4	1444.509509	881.356017	205.015734	186.602952	165.190546					881.356017	165.190546	359.5413123
8	1229.048646	95.69621	152.021022	223.654529	112.994413	101.913815	127.773558	115.278783	293.349254	293.349254	95.69621	152.835198
16	1426.498538	68.988243	69.019327	82.548198	89.518775	100.960711	88.552028	110.131483	70.334471	110.131483	68.988243	85.0066545
		80.029979	72.147735	71.572883	151.654559	103.434949	84.679633	98.248576	78.258389			

Table 7
Optimal clustering number N for mechanisms of different sizes (numbers of species).

Mechanism size	$\mathcal{O}(10)$	$\mathcal{O}(10^2)$	$\mathcal{O}(10^3)$
Optimal clustering number, N	2	4–8	8–16

weight matrix for chemical kinetics. Three hydrocarbon fuel/air ignition problems with an increasing dimension of the mechanism, up to 2115 species and 8157 reactions, are taken into consideration under varying initial conditions.

Computational efficiency and accuracy can be improved by choosing a proper number of clusters to split the large system. For the n-heptane mechanism, partition by 4 clusters of species leads to about 8 times speedup compared to the non-split VODE solver and 10–20 times speedup versus the explicit solver CHEMEQ2. For the n-hexadecane mechanism, partition by 8 clusters of species results in a speedup factor of around 40. Clustering by diffusion maps based on a given weight matrix outperforms the simple clustering according to species' index in the mechanism, in terms of predicting the correct ignition delay time and post-ignition equilibrium state. It implies that an optimal clustering for a certain mechanism is preferable not only for computational acceleration but also for higher accuracy. An optimal choice of clustering number N is suggested in Table 7 in relation with the dimension of the mechanism to consider.

With a specific clustering number, there is still room to improve the present species-clustered splitting scheme to further reduce splitting errors, e.g., the total mass conservation error at the ignition instant. Either a new definition of weight matrix or other optimal partition techniques in addition to diffusion maps are worth of further investigation. Taking advantage of the fast convergence of operator-splitting methods, it is also possible to use adaptive sub-cycling or time-stepping to achieve better accuracy. The above splitting so far considers the first-order Lie–Trotter scheme or the second-order Strang scheme, and extension to higher-order splitting schemes is straightforward. Adaptive variable clustering number might be another option. Also, a combination of the species-clustered splitting scheme and sparse matrix techniques to obtain additional efficiency gain is possible.

Acknowledgments

The financial support from the EU Marie Skłodowska-Curie Innovative Training Networks (ITN-ETN) (Project ID: 675528-IPPAD-H2020-MSCA-ITN-2015) for the first author is gratefully acknowledged. Xiangyu Y. Hu is also thankful for the partial support by National Natural Science Foundation of China (NSFC) (Grant No.: 11628206).

Appendix A. Clustering of species for the three involved mechanisms based on diffusion maps

For the GRI-Mech 3.0 mechanism of methane (CH_4), by setting $N = 2$, we have the diffusion maps based clustering as

$$C^2 = \{c_1, c_2, \ldots, c_{52}, c_{53}\} = \{2, 2, 2, 2, 2, 2, 2, 2, 2, 2, 2, 2, 2, 2, 2, 1, 1, 1, 1, 1, 1, 2, 2, 2, 2, 1, 1, 2, 2, 2, 1, 1, 1, 1, 1, 1, 1, 1, 1, 1, 2, 1, 1, 2, 2, 2, 1, 1, 2, 1, 1, 1, 1, 1\}, \tag{A.1}$$

where $c_i = 1$ or 2 means the ith species is clustered into subset 1 or 2.

For the n-heptane (n-C_7H_{16}) mechanism, by setting $N = 8$, we have

$$C^8 = \{c_1, c_2, \ldots, c_{560}, c_{561}\} = \{5, 5, 5, 5, 5, 5, 5, 5, 5, 1, 5, 5, 5, 5, 5, 1, 1, 5, 1, 1, 1, 6, 6, 1, 1, 6, 5, 6, 1, 6, 6, 5, 5, 5, 1, 5, 5, 1, 1, 1, 1, 1, 1, 1, 1, 5, 1, 1, 1, 1, 1, 1, 5, 5, 5, 5, 5, 5, 6, 8, 8, 8, 8, 8, 8, 8, 8, 1, 5, 8, 8, 1, 1, 1, 5, 1, 5, 1, 6, 6, 6, 6, 4, 1, 6, 6, 1, 1, 4, 4, 4, 4, 4, 4, 1, 1, 1, 1, 1, 1, 6, 6, 5, 4, 1, 1, 7, 8, 7, 3, 2, 4, 2, 4, 4, 4, 2, 4, 4, 2, 4, 2, 4, 2, 4, 4, 4, 4, 6, 6, 6, 6, 6, 1, 1, 1, 1, 1, 1, 1, 1, 1, 1, 1, 1, 8, 8, 3, 3, 6, 8, 8, 8, 8, 8, 8, 8, 8, 8, 8, 8, 8, 4, 2, 4, 2, 4, 2, 4, 4, 2, 2, 2, 2, 2, 4, 2, 4, 2, 2, 2, 2, 4, 4, 2, 2, 4, 2, 2, 4, 2, 1, 6, 7, 7, 6, 6, 6, 5, 5, 5, 3, 3, 3, 5, 5, 5, 2, 4, 2, 2, 2, 2, 4, 2, 4, 2, 4, 2, 4, 2, 4, 2, 4, 4, 1, 7, 7, 6, 1, 7, 8, 3, 8, 8, 4, 6, 1, 5, 5, 6, 6, 6, 8, 5, 3, 1, 7, 7, 7, 7, 7, 7, 7, 7, 7, 7, 6, 8, 7, 7, 7, 7, 7, 7, 7, 7, 7, 3, 6, 7, 3, 3, 7, 3, 7, 7, 3, 6, 7, 4, 5, 5, 6, 5, 6, 5, 5, 1, 5, 6, 6, 6, 4, 6, 8, 3, 8, 3, 8, 4, 4, 6, 6, 5, 5, 5, 5, 6, 8, 5, 8, 8, 5, 5, 5, 6, 7, 1, 5, 6, 6, 3, 6, 5, 6, 6, 6, 5, 6, 5, 8, 5, 6, 3, 6, 6, 3, 5, 7, 7, 3, 3, 8, 3, 3, 6, 5, 3, 3, 3, 3, 3, 5, 3, 3, 3, 3, 8, 3, 3, 5, 3, 3, 3, 5, 6, 6, 6, 6, 3, 3, 3, 3, 6, 3, 6, 6, 6, 1, 8, 8, 8, 1, 6, 6, 6, 1, 7, 7, 7, 1, 7, 6, 6, 8, 8, 8, 5, 8, 8, 2, 4, 2, 2, 2, 2, 2, 4, 2, 2, 4, 2, 2, 4, 2, 2, 2, 4, 2, 2, 4, 4, 4, 2, 2, 4, 4, 4, 4, 2, 3, 7, 7, 7, 7, 7, 7, 7, 3, 7, 7, 7, 7, 7, 8, 8, 8, 8, 8, 8, 8, 8, 1, 1, 1, 8, 8, 8, 8, 8, 8, 8, 8, 8, 8, 8, 8, 8, 8, 2, 4, 2, 2, 2, 2, 2, 4, 4, 2, 4, 2, 2, 4, 2, 4, 2, 2, 2, 2, 4, 4, 2, 4, 4, 4, 4, 2, 2, 2, 4, 4, 1, 6, 7, 7, 1, 7, 7, 7, 1, 6, 3, 7, 7, 7, 3, 7, 7, 7, 7, 3, 7, 7, 7, 7, 3, 3, 7, 7, 5, 6, 3, 3, 3, 3, 3, 5, 3, 3, 3, 5, 3, 3, 3, 3, 3, 3, 3, 3, 3, 3, 3, 3, 3, 3, 3, 8, 7, 5\}. \tag{A.2}$$

For the n-hexadecane (n-$C_{16}H_{34}$) mechanism, by setting $N = 8$, we have

$$C^8 = \{c_1, c_2, \ldots, c_{2114}, c_{2115}\} = \{3773373111111111181111111111111111117115575 7533337311117771133555536563555775377767773535 3577777755777777557757577777775777555777777187 7735335337777777777555612266122166122888228 8822881414111111111555353335335355577775556 6266652166121162448224888224888427777777777 4411414111111415577777577755777711171117117 3333333333333333333333335555555555555555555 5355555355555355555333333333333333333333555575 5377775377753777537353333333333333333333333333 3555555555555555555555555555555555333333333333 3333333333355555555555555555555555555555533 3333333333333333333335555555555555555555777777 7777777766886668866668886666888866668888666688 8866668888666688662266622666622266662222666622 2266662222666622226666226662266662266662222266 6622226666222266662266886668866668886666888866 6688886666888866662266622666622216662222666622 2266662266226662266662226666222266662222666122 6612216612221661222216612261226612216612221661 2222166122661221661222166122888888888888888888 8888888888888888888888888888888888882222222222 2222222222222222242222222422222224222242222822 2282222882222488822224888842248888422888888888 8888888888888888888888888888888888822882228822 2488882248888422488884224882288224888224888224 8888422488884228882248882248884224888842288828 8224888224888422488884228882248882248884228887 7677677776776677667766776777677777776776677667 7667677776776777667766776677677776776677667766776677 6676777677667766776677677776776677667766776677 7667777677677777677777767677767776777671114111141 1114411114441114444411414444144444444444444114 4111141111441114444111144441144444414444444444 1144111441114441114444111144441144444414444444 1144111441114441114444111144441144444414444444 4441114441114444111444441444444144411444111444 1114444144444444444144411444111444141444444444 4414441144411144414144444444144411444111414141 4443355555553355555557555555561755555551115555 5333355377333333333}, \tag{A.3}$$

leaving out the delimiter.

References

[1] I.E. Mersin, E.S. Blurock, H.S. Soyhan, A.A. Konnov, Hexadecane mechanisms: comparison of hand-generated and automatically generated with pathways, Fuel 115 (2014) 132–144, doi:10.1016/j.fuel.2013.06.055.
[2] O. Herbinet, W.J. Pitz, C.K. Westbrook, Detailed chemical kinetic oxidation mechanism for a biodiesel surrogate, Combust. Flame 154 (3) (2008) 507–528.
[3] T. Lu, C.K. Law, Toward accommodating realistic fuel chemistry in large-scale computations, Progr. Energy Combust. Sci. 35 (2) (2009) 192–215, doi:10.1016/j.pecs.2008.10.002.

[4] C. Xu, Y. Gao, Z. Ren, T. Lu, A sparse stiff chemistry solver based on dynamic adaptive integration for efficient combustion simulations, Combust. Flame 172 (2016) 183–193.
[5] T. Lu, C.K. Law, A directed relation graph method for mechanism reduction, Proc. Combust. Inst. 30 (1) (2005) 1333–1341.
[6] P. Pepiot-Desjardins, H. Pitsch, An efficient error-propagation-based reduction method for large chemical kinetic mechanisms, Combust. Flame 154 (1) (2008) 67–81, doi:10.1016/j.combustflame.2007.10.020.
[7] W. Sun, Z. Chen, X. Gou, Y. Ju, A path flux analysis method for the reduction of detailed chemical kinetic mechanisms, Combust. Flame 157 (7) (2010) 1298–1307, doi:10.1016/j.combustflame.2010.03.006.
[8] K.E. Niemeyer, C.-J. Sung, M.P. Raju, Skeletal mechanism generation for surrogate fuels using directed relation graph with error propagation and sensitivity analysis, Combust. Flame 157 (9) (2010) 1760–1770, doi:10.1016/j.combustflame.2009.12.022.
[9] P.N. Brown, G.D. Byrne, A.C. Hindmarsh, VODE: a variable-coefficient ode solver, SIAM J. Sci. Stat. Comput. 10 (5) (1989) 1038–1051.
[10] M. Caracotsios, W.E. Stewart, Sensitivity analysis of initial value problems with mixed odes and algebraic equations, Comput. Chem. Eng. 9 (4) (1985) 359–365, doi:10.1016/0098-1354(85)85014-6.
[11] Y. Morii, H. Terashima, M. Koshi, T. Shimizu, E. Shima, ERENA: a fast and robust jacobian-free integration method for ordinary differential equations of chemical kinetics, J. Comput. Phys. 322 (2016) 547–558.
[12] F. Perini, E. Galligani, R.D. Reitz, A study of direct and Krylov iterative sparse solver techniques to approach linear scaling of the integration of chemical kinetics with detailed combustion mechanisms, Combust. Flame 161 (5) (2014) 1180–1195.
[13] V. Damian, A. Sandu, M. Damian, F. Potra, G.R. Carmichael, The kinetic preprocessor KPP – a software environment for solving chemical kinetics, Comput. Chem. Eng. 26 (11) (2002) 1567–1579.
[14] Z. Ren, C. Xu, T. Lu, M.A. Singer, Dynamic adaptive chemistry with operator splitting schemes for reactive flow simulations, J. Comput. Phys. 263 (2014) 19–36.
[15] M. Singer, S. Pope, Exploiting ISAT to solve the reaction–diffusion equation, Combust. Theory Model. 8 (2) (2004) 361–383.
[16] M. Singer, S. Pope, H. Najm, Operator-splitting with ISAT to model reacting flow with detailed chemistry, Combust. Theory Model. 10 (2) (2006) 199–217.
[17] O.M. Knio, H.N. Najm, P.S. Wyckoff, A semi-implicit numerical scheme for reacting flow: II. Stiff, operator-split formulation, J. Comput. Phys. 154 (2) (1999) 428–467.
[18] Z. Ren, S.B. Pope, Second-order splitting schemes for a class of reactive systems, J. Comput. Phys. 227 (17) (2008) 8165–8176.
[19] Y. Gao, Y. Liu, Z. Ren, T. Lu, A dynamic adaptive method for hybrid integration of stiff chemistry, Combust. Flame 162 (2) (2015) 287–295.
[20] K. Nguyen, A. Caboussat, D. Dabdub, Mass conservative, positive definite integrator for atmospheric chemical dynamics, Atmos. Environ. 43 (40) (2009) 6287–6295.
[21] S. Pan, J. Wang, X. Hu, N.A. Adams, A network partition method for solving large-scale complex nonlinear processes, 2018, arXiv preprint arXiv:1801.06207.
[22] R.R. Coifman, S. Lafon, Diffusion maps, Appl. Comput. Harmon. Anal. 21 (1) (2006) 5–30.
[23] S. Lafon, A.B. Lee, Diffusion maps and coarse-graining: a unified framework for dimensionality reduction, graph partitioning, and data set parameterization, IEEE Trans. Pattern Anal. Mach. Intell. 28 (9) (2006) 1393–1403.
[24] R.R. Coifman, S. Lafon, A.B. Lee, M. Maggioni, B. Nadler, F. Warner, S.W. Zucker, Geometric diffusions as a tool for harmonic analysis and structure definition of data: diffusion maps, Proc. Natl. Acad. Sci. U.S.A. 102 (21) (2005) 7426–7431.
[25] M.I. Malinen, P. Fränti, Balanced k-means for clustering, 2014 Joint IAPR International Workshops on Statistical Techniques in Pattern Recognition (SPR) and Structural and Syntactic Pattern Recognition (SSPR), Springer (2014), pp. 32–41.
[26] R.I. McLachlan, G.R.W. Quispel, Splitting methods, Acta Numer. 11 (2002) 341–434.
[27] G. Strang, On the construction and comparison of difference schemes, SIAM J. Numer. Anal. 5 (3) (1968) 506–517.
[28] D.A. Schwer, J.E. Tolsma, W.H. Green Jr., P.I. Barton, On upgrading the numerics in combustion chemistry codes, Combust. Flame 128 (3) (2002) 270–291.
[29] M. Domijan, What are... some graphs of chemical reaction networks?, Vol. 1, Mathematics Institute, University of Warwick, Coventry CV4 7AL, United Kingdom (2008), pp. 1–18.
[30] MATLAB, MATLAB Version 9.1.0.441655 (R2016b), The MathWorks Inc., Natick, Massachusetts, 2016.
[31] D.R. Mott, E.S. Oran, CHEMEQ2: a solver for the stiff ordinary differential equations of chemical kinetics, Technical Report, Naval Research Lab Washington DC, 2001.
[32] J.-H. Wang, S. Pan, X.Y. Hu, N.A. Adams, A split random time-stepping method for stiff and nonstiff detonation capturing, Combust. Flame (2018), doi:10.1016/j.combustflame.2019.03.0.
[33] G.P. Smith, D.M. Golden, M. Frenklach, N.W. Moriarty, B. Eiteneer, M. Goldenberg, C.T. Bowman, R.K. Hanson, S. Song, W.C. Gardiner Jr., et al., Gri 3.0 mechanism, 21, Gas Research Institute, Des Plaines, IL (1999), p. 2017. accessed Aug
[34] H.J. Curran, P. Gaffuri, W.J. Pitz, C.K. Westbrook, A comprehensive modeling study of n-heptane oxidation, Combust. Flame 114 (1–2) (1998) 149–177.
[35] H.J. Curran, P. Gaffuri, W.J. Pitz, C.K. Westbrook, A comprehensive modeling study of iso-octane oxidation, Combust. Flame 129 (3) (2002) 253–280.
[36] C. Westbrook, W. Pitz, O. Herbinet, E. Silke, H. Curran, A detailed chemical kinetic reaction mechanism for n-alkane hydrocarbons from n-octane to n-hexadecane, Technical Report, Lawrence Livermore National Laboratory (LLNL), Livermore, CA, 2007.
[37] D.J. Seery, C.T. Bowman, An experimental and analytical study of methane oxidation behind shock waves, Combust. Flame 14 (1) (1970) 37–47.
[38] C.S. Yoo, T. Lu, J.H. Chen, C.K. Law, Direct numerical simulations of ignition of a lean n-heptane/air mixture with temperature inhomogeneities at constant volume: parametric study, Combust. Flame 158 (9) (2011) 1727–1741.
[39] C.K. Westbrook, W.J. Pitz, O. Herbinet, H.J. Curran, E.J. Silke, A comprehensive detailed chemical kinetic reaction mechanism for combustion of n-alkane hydrocarbons from n-octane to n-hexadecane, Combust. Flame 156 (1) (2009) 181–199.

B.3 Paper III

Jianhang Wang, Shucheng Pan, Xiangyu Y. Hu, Nikolaus A. Adams

Partial characteristic decomposition for multi-species Euler equations

In *Computers and Fluids*, Volume 181, 2019, pp. 364-382, DOI: `https://doi.org/10.1016/j.compfluid.2019.01.023`.

Contribution: My contribution to this work was the development of the method and the corresponding computer code for its implementation. I performed simulations and analyzed the results, and wrote the manuscript for the publication.

Computers and Fluids 181 (2019) 364–382

Contents lists available at ScienceDirect

Computers and Fluids

journal homepage: www.elsevier.com/locate/compfluid

Partial characteristic decomposition for multi-species Euler equations

Jian-Hang Wang, Shucheng Pan*, Xiangyu Y. Hu*, Nikolaus A. Adams

Chair of Aerodynamics and Fluid Mechanics, Department of Mechanical Engineering, Technical University of Munich, Garching 85748, Germany

ARTICLE INFO

Article history:
Received 29 August 2018
Revised 20 December 2018
Accepted 30 January 2019
Available online 30 January 2019

Keywords:
Multi-species Euler equations
Characteristic decomposition
Finite difference schemes
Shock-capturing schemes
Roe averages

ABSTRACT

High-order finite difference schemes employing characteristic decomposition are widely used for the simulation of compressible gas flows with multiple species. A challenge for the computational efficiency of such schemes is the quadratically increasing dimensionality of the convective flux eigensystem as the number of species increases. Considering the sparsity of the multi-species eigensystem, a remedy is proposed to split the eigensystem into two parts. One is the gas mixture part, which is subjected to the established characteristic decomposition schemes for single-fluid Euler equations. The other part corresponds to the species partial mass equations, which can be solved directly in physical space as the decoupled sub-eigensystem for the species part is composed of two diagonal identity matrices. This property relies on the fact that species are advected with the same convective velocity. In this way, only the gas mixture part requires a characteristic decomposition, resulting in a much higher efficiency for the convective-flux calculation. To cure the inconsistency due to splitting, a consistent update of species mass fractions is proposed. Non-reactive and reactive test cases demonstrate that the proposed scheme reduces the computational cost without deteriorating high-order accuracy.

1. Introduction

Compressible reactive gas flows of multiple species arise in a variety of combustion problems, ranging from scramjet engines to the incineration of waste. Accurate numerical simulation of such flows relies on low-dissipation, high-order shock-capturing schemes designed for discretizing convection terms in the reactive Navier–Stokes or Euler equations. The shock-capturing scheme should be capable of preserving sharp discontinuities without introducing spurious oscillations. For this purpose, a variety of high-order interpolation schemes can be used in the characteristic decomposition based finite difference formulation, together with a flux-splitting scheme, to approximate the upwind convective flux. A classical example of such schemes is the WENO-LLF scheme [3,24]. Extension to multi-dimensional flows can be straightforwardly realized in a dimension-by-dimension manner [25].

However, as an essential ingredient of high-order finite difference schemes, characteristic decomposition may constrain computational efficiency when multiple species are involved. The multi-species Euler equations involve multiple partial mass equations of species to be solved in association with mass, momentum and energy equations of the total mixture. The eigensystem of the linearized convective flux matrix, established e.g. by Roe [22], Glaister [10] and Shuen [26], can have very large dimensionality as the number of species increases. As a result, the computational efforts for matrix operations obeying the characteristic decomposition scheme inevitably grow. High-order interpolation which applies such matrix operations several times for each cell-face convective flux calculation renders classical high-order finite difference schemes for multi-species Euler equations [2,8,9,32] computationally very expensive for large numbers of species.

In the current study of multi-species flows, we propose to reduce dimensionality of the eigensystem. Feasibility is based on the fact that the eigenmatrices composed of left and right eigenvectors, respectively, are sparse and non-zero entries in both matrices are mainly distributed along the diagonal. Moreover, the diagonal elements in the right-bottom part of both matrices, which accounts for the species mass convection, are unity.

In this paper, we take advantage of the structure of the eigenmatrices and propose a partial characteristic decomposition scheme for multi-species Euler equations. We split the eigensystem into two parts along the diagonal of eigenmatrix: one is the gas mixture part and the other part accounts for all the species. Correspondingly, the conserved vector of the total mixture mass, momenta and energy as well as species partial densities is divided

* Corresponding author.
E-mail addresses: jianhang.wang@tum.de (J.-H. Wang), shucheng.pan@tum.de (S. Pan), xiangyu.hu@tum.de, xiangyu.hu@aer.mw.tum.de (X.Y. Hu), nikolaus.adams@tum.de (N.A. Adams).

https://doi.org/10.1016/j.compfluid.2019.01.023
0045-7930/

into a gas mixture part and the remaining species partial density part. All the species follow a series of independent advection equations in a conservative form. Compared with classical characteristic decomposition schemes, the proposed split scheme utilizes characteristic decomposition for single-fluid Euler equations [22,24] to handle the first gas mixture part. It allows to avoid the characteristic decomposition of the species part. Therefore, computational effort can be reduced significantly as no species transformation from physical space to characteristic space and back is needed. To cope with the inconsistency issue after decoupling the partial densities of species from the mixture total density, a species mass fraction correction is proposed.

The paper is organized as follows. In Section 2, we introduce the 3D multi-species Euler equations and the classical characteristic decomposition scheme used to compute high-order convective fluxes in the finite difference formulation. The proposed partial characteristic decomposition scheme is then formulated, followed by a consistent update for mass fractions of species. Section 3 contains numerical experiments to make a comparison of our proposed decoupled scheme with the fully coupled scheme, including several 1D and 2D, non-reactive and reactive cases with different numbers of species. Conclusions are drawn in Section 4.

2. Methodology

Consider the 3D multi-species (or multi-component) Euler equations with chemical reaction source terms, i.e.

$$U_t + F(U)_x + G(U)_y + H(U)_z = S(U), \tag{1}$$

where

$$\begin{aligned} U &= (\rho, \rho u, \rho v, \rho w, \rho e_t, \rho y_1, \rho y_2, \cdots, \rho y_{N_s-1})^T, \\ F(U) &= \big(\rho u, \rho u^2 + p, \rho vu, \rho wu, (\rho e_t + p)u, \rho y_1 u, \rho y_2 u, \cdots, \\ &\quad \rho y_{N_s-1} u\big)^T, \\ G(U) &= \big(\rho v, \rho uv, \rho v^2 + p, \rho wv, (\rho e_t + p)v, \rho y_1 v, \rho y_2 v, \cdots, \\ &\quad \rho y_{N_s-1} v\big)^T, \\ H(U) &= \big(\rho w, \rho uw, \rho vw, \rho w^2 + p, (\rho e_t + p)w, \rho y_1 w, \rho y_2 w, \cdots, \\ &\quad \rho y_{N_s-1} w\big)^T, \\ S(U) &= (0, 0, 0, 0, 0, \dot{\omega}_1, \dot{\omega}_2, \cdots, \dot{\omega}_{N_s-1})^T \end{aligned} \tag{2}$$

are vectors of the conserved variables, convective flux in the x, y or z direction and source terms, respectively, with $\dot{\omega}_i$ representing rate of change of the ith species concentration in the reactive gas mixture due to chemical kinetics consisting of N_s species. When the flow is inert without activating chemical reactions, source terms are replaced by a zero vector. The specific total energy including the specific internal energy e is $e_t = e + \frac{1}{2}(u^2 + v^2 + w^2)$. To close the system, an equation of state (EoS) of the form

$$p = \rho \sum_{i=1}^{N_s} y_i \frac{R_u}{W_i} T \tag{3}$$

is used for the gas mixture, with y_i and W_i denoting the mass fraction and molecular weight of the ith species, respectively, and R_u being the universal gas constant and p being the pressure.

The above conservation laws of mass, momentums and energy with source terms are usually solved numerically using operator splitting. For the flow convection part,

$$U_t + F(U)_x + G(U)_y + H(U)_z = 0, \tag{4}$$

shock-capturing schemes are usually employed based on either finite volume (FV) or finite difference (FD) formulation for spatial discretization, in which high-order shock-capturing accuracy as well as high computational efficiency are desired. Low-order FV schemes approximate the cell-face flux function by upwind reconstruction using primitive or conserved variables, together with MUSCL interpolation schemes plus slope limiters and achieve generally second-order accuracy. High-order shock-capturing schemes are realized by characteristic-decomposition flux splitting (also referred as characteristic-wise flux splitting) to assemble the half-point convective flux using high-order interpolation schemes in FD approaches.

2.1. Fully coupled characteristic-wise flux splitting

In the characteristic-wise flux-splitting schemes, the Jacobian of convective flux in Eq. (4) is considered such as

$$A = \frac{\partial F}{\partial U} = L \Lambda R. \tag{5}$$

For a general formulation of the flux functions, F, G and H can be written as

$$\tilde{F}(U) = \begin{pmatrix} \rho M \\ \rho u M + p n_1 \\ \rho v M + p n_2 \\ \rho w M + p n_3 \\ (\rho e_t + p) M \\ \rho y_1 M \\ \rho y_2 M \\ \cdots \\ \rho y_{N_s-1} M \end{pmatrix}, \tag{6}$$

with the unit normal vector $\underline{n} = \{n_1, n_2, n_3\}$ and the velocity $M = n_1 u + n_2 v + n_3 w$. Thus, F is abbreviated for $\underline{n} = \{1, 0, 0\}$ and G is abbreviated for $\underline{n} = \{0, 1, 0\}$. H corresponds to $\underline{n} = \{0, 0, 1\}$. The eigensystem of left and right matrices is

$$\tilde{L} = \tilde{R}^{-1} = \begin{pmatrix} \tilde{l}_1 \\ \tilde{l}_2 \\ \tilde{l}_3 \\ \tilde{l}_4 \\ \tilde{l}_5 \\ \tilde{l}_6 \\ \vdots \\ \tilde{l}_{N_s+4} \end{pmatrix} = \begin{pmatrix} \frac{b_2 + M/c + b_3}{2} & \frac{-b_1 u - n_1/c}{2} & \frac{-b_1 v - n_2/c}{2} & \frac{-b_1 w - n_3/c}{2} & \frac{b_1}{2} & \frac{-b_1 z_1}{2} & \cdots & \frac{-b_1 z_{N_s-1}}{2} \\ 1 - b_2 - b_3 & b_1 u & b_1 v & b_1 w & -b_1 & b_1 z_1 & \cdots & b_1 z_{N_s-1} \\ \frac{M n_2 - v}{n_1} & -n_2 & \frac{1 - n_2^2}{n_1} & \frac{-n_2 n_3}{n_1} & 0 & 0 & \cdots & 0 \\ \frac{M n_3 - w}{n_1} & -n_3 & \frac{-n_2 n_3}{n_1} & \frac{1 - n_3^2}{n_1} & 0 & 0 & \cdots & 0 \\ \frac{b_2 - M/c + b_3}{2} & \frac{-b_1 u + n_1/c}{2} & \frac{-b_1 v + n_2/c}{2} & \frac{-b_1 w + n_3/c}{2} & \frac{b_1}{2} & \frac{-b_1 z_1}{2} & \cdots & \frac{-b_1 z_{N_s-1}}{2} \\ -y_1 & 0 & 0 & 0 & 0 & 1 & \cdots & 0 \\ \vdots & \vdots & \vdots & \vdots & \vdots & \vdots & \ddots & \vdots \\ -y_{N_s-1} & 0 & 0 & 0 & 0 & 0 & \cdots & 1 \end{pmatrix}, \tag{7}$$

and

$$\tilde{R} = \left(\tilde{r}_1, \tilde{r}_2, \tilde{r}_3, \tilde{r}_4, \tilde{r}_5, \tilde{r}_6, \cdots, \tilde{r}_{N_s+4}\right) = \begin{pmatrix} 1 & 1 & 0 & 0 & 1 & 0 & \cdots & 0 \\ u - cn_1 & u & -n_2 & -n_3 & u + cn_1 & 0 & \cdots & 0 \\ v - cn_2 & v & n_1 & 0 & v + cn_2 & 0 & \cdots & 0 \\ w - cn_3 & w & 0 & n_1 & w + cn_3 & 0 & \cdots & 0 \\ H - cM & H - \frac{1}{b_1} & vn_1 - un_2 & wn_1 - un_3 & H + cM & z_1 & \cdots & z_{N_s-1} \\ y_1 & y_1 & 0 & 0 & y_1 & 1 & \cdots & 0 \\ \vdots & \vdots & \vdots & \vdots & \vdots & \vdots & \ddots & \vdots \\ y_{N_s-1} & y_{N_s-1} & 0 & 0 & y_{N_s-1} & 0 & \cdots & 1 \end{pmatrix}, \tag{8}$$

where c represents the speed of sound and

$$\begin{aligned} H &= e + \frac{p}{\rho} + \frac{1}{2}Q, \\ z_i &= -\rho \frac{\partial p}{\partial \rho y_i} \Big/ \frac{\partial p}{\partial e}, \quad i = 1, 2, \cdots, N_s - 1, \\ b_1 &= \frac{1}{\rho c^2}\frac{\partial p}{\partial e}, \\ b_2 &= 1 + b_1 Q - b_1 H, \\ b_3 &= b_1 \sum_{i=1}^{N_s-1} y_i z_i, \end{aligned} \tag{9}$$

by defining $Q = u^2 + v^2 + w^2$. The pressure derivatives, $\frac{\partial p}{\partial e}$, $\frac{\partial p}{\partial \rho y_i}$ and $\frac{\partial p}{\partial \rho}$, are obtained by fixing other variables in the transformed EoS

$$p = p(\rho, e, \rho y_1, \cdots, \rho y_{N_s-1}).$$

If $n_1 = 0$, which is the case for calculation of flux function $G(U)$ or $H(U)$, l_3 and l_4 in Eq. (7) are invalid and can be replaced by

$$\begin{aligned} l_3^* &= \left(\tfrac{Mn_1 - u}{n_2} \quad \tfrac{1-n_1^2}{n_2} \quad -n_1 \quad \tfrac{-n_1 n_3}{n_2} \quad 0 \quad 0 \quad \cdots \quad 0\right), \\ l_4^* &= \left(\tfrac{Mn_3 - w}{n_2} \quad \tfrac{-n_1 n_3}{n_2} \quad -n_3 \quad \tfrac{1-n_3^2}{n_2} \quad 0 \quad 0 \quad \cdots \quad 0\right), \end{aligned} \tag{10}$$

if $n_2 \neq 0$. Correspondingly, r_3 and r_4 in Eq. (8) should be replaced by

$$\begin{aligned} r_3^* &= \begin{pmatrix} 0 & n_2 & -n_1 & 0 & un_2 - vn_1 & 0 & \cdots & 0 \end{pmatrix}^T, \\ r_4^* &= \begin{pmatrix} 0 & 0 & -n_3 & n_2 & wn_2 - vn_3 & 0 & \cdots & 0 \end{pmatrix}^T. \end{aligned} \tag{11}$$

If $n_2 = 0$ and $n_3 \neq 0$, $l_{3,4}$ and $r_{3,4}$ can be further replaced by

$$\begin{aligned} l_3^{**} &= \left(\tfrac{Mn_1 - u}{n_3} \quad \tfrac{1-n_1^2}{n_3} \quad \tfrac{-n_1 n_2}{n_3} \quad -n_1 \quad 0 \quad 0 \quad \cdots \quad 0\right), \\ l_4^{**} &= \left(\tfrac{Mn_2 - v}{n_3} \quad \tfrac{-n_1 n_2}{n_3} \quad \tfrac{1-n_2^2}{n_3} \quad -n_2 \quad 0 \quad 0 \quad \cdots \quad 0\right), \end{aligned} \tag{12}$$

and

$$\begin{aligned} r_3^{**} &= \begin{pmatrix} 0 & n_3 & 0 & -n_1 & un_3 - wn_1 & 0 & \cdots & 0 \end{pmatrix}^T, \\ r_4^{**} &= \begin{pmatrix} 0 & 0 & n_3 & -n_2 & vn_3 - wn_2 & 0 & \cdots & 0 \end{pmatrix}^T. \end{aligned} \tag{13}$$

Finally, eigenvalues in the diagonal characteristic matrix Λ in Eq. (5) are

$$M - c, M, M, M, M + c, M, \cdots, M. \tag{14}$$

Given the analytical expressions of left and right eigenvector as above, it is important to note that both eigenvectors and eigenvalues are locally defined at half points or cell faces such as $F_{i+\frac{1}{2},j,k}$ or $G_{i,j+\frac{1}{2},k}$. Therefore, it is required to obtain proper averaged state between two adjacent states U_L and U_R at grid points or neighboring cell centers. Following the Roe average [10,11,22] for ideal gas and its extension to multi-component non-equilibrium reactive flows [26], the U-property accounting for the jump conditions of two adjacent states can be satisfied by Roe-average the following variables

$$\begin{aligned} &\tilde{\rho} = \sqrt{\rho_L \rho_R}, \\ &\tilde{f} = \mu(f) = \frac{\sqrt{\rho_L} f_L + \sqrt{\rho_R} f_R}{\sqrt{\rho_L} + \sqrt{\rho_R}}, \quad f = u, v, w, H, e, y_1, \cdots, y_{N_s-1}. \end{aligned} \tag{15}$$

Left to be satisfied is the pressure jump condition

$$\Delta p = \widetilde{\left(\frac{\partial p}{\partial \rho}\right)} \Delta \rho + \widetilde{\left(\frac{\partial p}{\partial e}\right)} \Delta e + \sum_{i=1}^{N_s-1} \widetilde{\left(\frac{\partial p}{\partial \rho y_i}\right)} \Delta(\rho y_i), \tag{16}$$

where $\Delta(\cdot) = (\cdot)_R - (\cdot)_L$. Note that definitions for the averaged pressure derivatives are not unique, and Eq. (16) defines a hyperplane as

$$\alpha x + \beta y + \sum_{i=1}^{N_s-1} \gamma_i z_i = 1 \tag{17}$$

with

$$\begin{aligned} &\alpha \equiv \frac{\Delta \rho}{\Delta p}\phi, \quad \beta \equiv \frac{\Delta e}{\Delta p}\psi, \quad \gamma_i \equiv \frac{\Delta(\rho y_i)}{\Delta p}\eta_i, \\ &x \equiv \widetilde{\left(\frac{\partial p}{\partial \rho}\right)}/\phi, \quad y \equiv \widetilde{\left(\frac{\partial p}{\partial e}\right)}/\psi, \quad z_i \equiv \widetilde{\left(\frac{\partial p}{\partial \rho y_i}\right)}/\eta_i, \end{aligned} \tag{18}$$

where ϕ, ψ, η_i are the scaling factors [26].

Given all partial derivatives of pressure at the left and right states, we can first introduce Roe-averaged derivatives of pressure by imposing $\tilde{f} = \mu(f)$ in Eq. (15), i.e.

$$\begin{aligned} &\overline{\left(\frac{\partial p}{\partial \rho}\right)} = \mu\left(\frac{\partial p}{\partial \rho}\right), \\ &\overline{\left(\frac{\partial p}{\partial e}\right)} = \mu\left(\frac{\partial p}{\partial e}\right), \\ &\overline{\left(\frac{\partial p}{\partial \rho y_i}\right)} = \mu\left(\frac{\partial p}{\partial \rho y_i}\right), \quad i = 1, \cdots, N_s - 1. \end{aligned} \tag{19}$$

Then starting from point S

$$\begin{aligned} &\left(x_s, y_s, z_{1s}, \cdots, z_{N_s-1 s}\right) \\ &= \left(\overline{\left(\frac{\partial p}{\partial \rho}\right)}/\phi, \overline{\left(\frac{\partial p}{\partial e}\right)}/\psi, \overline{\left(\frac{\partial p}{\partial \rho y_1}\right)}/\eta_1, \cdots, \overline{\left(\frac{\partial p}{\partial \rho y_{N_s-1}}\right)}/\eta_{N_s-1}\right), \end{aligned}$$

its projection P

$$\begin{aligned} &\left(x_p, y_p, z_{1p}, \cdots, z_{N_s-1 p}\right) \\ &= \left(\widetilde{\left(\frac{\partial p}{\partial \rho}\right)}/\phi, \widetilde{\left(\frac{\partial p}{\partial e}\right)}/\psi, \widetilde{\left(\frac{\partial p}{\partial \rho y_1}\right)}/\eta_1, \cdots, \widetilde{\left(\frac{\partial p}{\partial \rho y_{N_s-1}}\right)}/\eta_{N_s-1}\right) \end{aligned}$$

onto the hyperplane defined by Eqs. (17), (18) can be determined by

$$\begin{aligned} x_p &= x_s + \alpha\Omega, \\ y_p &= y_s + \beta\Omega, \\ z_{ip} &= z_{is} + \gamma_i\Omega, \quad i = 1, \cdots, N_s - 1, \end{aligned} \tag{20}$$

where

$$\Omega = \frac{1 - \alpha x_s - \beta y_s - \sum_{i=1}^{N_s-1} \gamma_i z_{is}}{\alpha^2 + \beta^2 + \sum_{i=1}^{N_s-1} \gamma_i^2}. \tag{21}$$

State P on the plane naturally satisfies the pressure jump condition and might give a suitable set of derivatives which will be further employed in calculating averaged cell-face eigenvalues and eigenvectors in Eqs. (7), (8) and (14), together with simple Roe-averaged values in Eq. (15). The consistent averaged speed of sound should be a positive real number and can be obtained by

$$\tilde{c}^2 = \widetilde{\left(\frac{\partial p}{\partial \rho}\right)} + \frac{\tilde{p}}{\tilde{\rho}^2}\widetilde{\left(\frac{\partial p}{\partial e}\right)} + \sum_{i=1}^{N_s-1} \tilde{y}_i \widetilde{\left(\frac{\partial p}{\partial \rho y_i}\right)} \tag{22}$$

with

$$\tilde{p} = \tilde{\rho}\left(\tilde{H} - \tilde{e} - \frac{\tilde{u}^2 + \tilde{v}^2 + \tilde{w}^2}{2}\right), \tag{23}$$

as in [10].

We now have obtained the approximate eigensystem located at the cell face between two cell-centered adjacent states. Decomposition of the multi-species Euler equations in the physical space can be done by projecting them onto the characteristic space with the left matrix $\tilde{L}$, where high-order interpolation schemes, e.g. WENO5 [12], can be used in combination with local Lax–Friedrich splitting for example. Finally, physical flux vectors are obtained by inverse transform of the system onto physical space with matrix $\tilde{R}$. E.g. for a cell face at $\{i+\frac{1}{2}, j, k\}$, stencils of six points/states are needed next to the cell face, i.e. $\{i', j, k\}$ with $i' = i-2, \cdots, i+3$, such that we have

$$\begin{aligned} f_{i'} &= \tilde{L}_{i+\frac{1}{2}} F_{i'}, \\ q_{i'} &= \tilde{L}_{i+\frac{1}{2}} U_{i'}, \\ f^{\pm}_{i'} &= \frac{1}{2}(f \pm \lambda q)_{i'}, \\ \tilde{f}^{+}_{i+\frac{1}{2}} &= \mathrm{WENO5}\{f^{+}_{i'}, i' = i-2, \cdots, i+3\}, \\ \tilde{f}^{-}_{i+\frac{1}{2}} &= \mathrm{WENO5}\{f^{-}_{i''}, i'' = i+3, \cdots, i-2\}, \\ \tilde{F}_{i+\frac{1}{2}} &= \tilde{R}_{i+\frac{1}{2}}\left(\tilde{f}^{+}_{i+\frac{1}{2}} + \tilde{f}^{-}_{i+\frac{1}{2}}\right) \end{aligned} \tag{24}$$

and $\tilde{F}_{i+\frac{1}{2}}$ is the expected convective flux in the physical space. Note that each λ is the maximum eigenvalue in Eq. (14) over stencils, and left and right matrices with tilde are defined in Eqs. from (7)–(13).

Several matrix multiplications with vectors have to be performed in the above process of calculating a cell-face flux such as $\tilde{L}_{i+\frac{1}{2}} F_{i'}$, $\tilde{L}_{i+\frac{1}{2}} U_{i'}$ and $\tilde{R}_{i+\frac{1}{2}} \tilde{f}^{\pm}_{i+\frac{1}{2}}$. In addition to the element-by-element interpolation by WENO5, operations upon matrix products are computationally very expensive. As the number of species increases, dimensionality of the eigensystem, $N_s + 4$, increases quadratically, such that the computational cost for these operations will be dramatically raised.

2.2. Partial characteristic-wise flux splitting

From the structure of left and right matrices, it is easy to see that except for the first five eigenvectors, i.e. $\{l_1, \cdots, l_5\}$ as well as $\{r_1, \cdots, r_5\}$ corresponding to eigenvalues of $\{M-c, M, M, M, M+c\}$, respectively, species-related elements are mostly zero. Moreover, the diagonal identity sub-matrix in the right-bottom part of L and R, respectively, conforms to the fact that all species share the same convective velocity M.

As a result, it is convenient to split the eigenmatrices into two parts along the diagonal, by ignoring the coupling relations between the species and mixture total variables such as ρ, u and e, etc, which are represented by the non-zero off-diagonal entries. In this way, the conserved variable vector of multi-species Euler equations is decomposed into an 'ideal gas' part, $\{\rho, \rho u, \rho v, \rho u, \rho e_t\}^T$, and the other part consisting of species partial densities, $\{\rho y_1, \cdots, \rho y_{N_s-1}\}^T$. Accordingly, the fully coupled eigensystem in Eqs. (7) and (8) can be decomposed into

$$\tilde{L}_1 = \begin{pmatrix} \frac{b_2+M/c+b_3}{2} & \frac{-b_1u-n_1/c}{2} & \frac{-b_1v-n_2/c}{2} & \frac{-b_1w-n_3/c}{2} & \frac{b_1}{2} \\ 1-b_2-b_3 & b_1u & b_1v & b_1w & -b_1 \\ \frac{Mn_2-v}{n_1} & -n_2 & \frac{1-n_2^2}{n_1} & \frac{-n_2n_3}{n_1} & 0 \\ \frac{Mn_3-w}{n_1} & -n_3 & \frac{-n_2n_3}{n_1} & \frac{1-n_3^2}{n_1} & 0 \\ \frac{b_2-M/c+b_3}{2} & \frac{-b_1u+n_1/c}{2} & \frac{-b_1v+n_2/c}{2} & \frac{-b_1w+n_3/c}{2} & \frac{b_1}{2} \end{pmatrix},$$

$$\tilde{L}_2 = \begin{pmatrix} 1 & \cdots & 0 \\ \vdots & \ddots & \vdots \\ 0 & \cdots & 1 \end{pmatrix}_{N_s-1, N_s-1}, \tag{25}$$

and correspondingly

$$\tilde{R}_1 = \begin{pmatrix} 1 & 1 & 0 & 0 & 1 \\ u-cn_1 & u & -n_2 & -n_3 & u+cn_1 \\ v-cn_2 & v & n_1 & 0 & v+cn_2 \\ w-cn_3 & w & 0 & n_1 & w+cn_3 \\ H-cM & H-\frac{1}{b_1} & vn_1-un_2 & wn_1-un_3 & H+cM \end{pmatrix},$$

$$\tilde{R}_2 = \begin{pmatrix} 1 & \cdots & 0 \\ \vdots & \ddots & \vdots \\ 0 & \cdots & 1 \end{pmatrix}_{N_s-1, N_s-1}. \tag{26}$$

As mentioned previously, since $\tilde{L}_2$ and $\tilde{R}_2$ both are identity matrices, the advection equations of species partial densities are inherently independent of each other in physical space, with the same convective velocity. Transforming them onto the characteristic space is unnecessary and costly matrix multiplication operations can be avoided. The remaining sub-eigensystem, $\tilde{L}_1$ and $\tilde{R}_1$, which accounts for the gas mixture transport of total density, momenta and energy, recovers that of the ideal gas single-fluid Euler equations. It is still subject to characteristic-wise flux splitting and high-order interpolation to calculate the cell-face fluxes. However, the remaining matrix-multiplication operations have been largely reduced to a low dimensionality of 5 for 3D flows. It is to be noted that in order to meet the requirement of characteristic decomposition, i.e. $\tilde{L}_1 = \tilde{R}_1^{-1}$, we have to enforce

$$b_3 = 0$$

in Eqs. (25) and (26). All other elements including the interface speed of sound are obtained in the same way as the fully coupled flux-splitting scheme in last subsection.

2.2.1. Analysis of numerical convective fluxes

Similarly with [13,19], we first divide the WENO flux given by Eq. (24) into a central and numerical dissipation parts as

$$\begin{aligned} \tilde{F}_{i+\frac{1}{2}} &= \tilde{R}_{i+\frac{1}{2}}\left(\tilde{f}^{+}_{i+\frac{1}{2}} + \tilde{f}^{-}_{i+\frac{1}{2}}\right) = \sum_{s=1}^{N_s+4} \tilde{r}^{s}_{i+\frac{1}{2}} f^{+,s}_{i+\frac{1}{2}} + \sum_{s=1}^{N_s+4} \tilde{r}^{s}_{i+\frac{1}{2}} f^{-,s}_{i+\frac{1}{2}} \\ &= \underbrace{\frac{1}{60}(F_{i-2} - 8F_{i-1} + 37F_i + 37F_{i+1} - 8F_{i+2} + F_{i+3})}_{\text{central part}} \end{aligned}$$

$$
\begin{aligned}
&\underbrace{-\frac{1}{60}\sum_{s=1}^{N_s+4}\tilde{r}^s_{i+\frac{1}{2}}\left\{\left(20\omega_1^+-1\right)\tilde{f}^{+,s}_{i,1}-\left(10\left(\omega_1^++\omega_2^+\right)-5\right)\tilde{f}^{+,s}_{i,2}+\tilde{f}^{+,s}_{i,3}\right\}}_{\text{dissipation part by positive upwind flux}}\\
&\underbrace{+\frac{1}{60}\sum_{s=1}^{N_s+4}\tilde{r}^s_{i+\frac{1}{2}}\left\{\left(20\omega_1^--1\right)\tilde{f}^{-,s}_{i,1}-\left(10\left(\omega_1^-+\omega_2^-\right)-5\right)\tilde{f}^{-,s}_{i,2}+\tilde{f}^{-,s}_{i,3}\right\}}_{\text{dissipation part by positive upwind flux}},
\end{aligned}
\tag{27}
$$

where

$$
\begin{aligned}
\tilde{f}^{+,s}_{i,k+1} &= f^{s,+}_{i+k-2}-3f^{s,+}_{i+k-1}+3f^{s,+}_{i+k}-f^{s,+}_{i+k+1}, \quad k=0,1,2,\\
\tilde{f}^{-,s}_{i,3-k} &= f^{s,-}_{i+k-2}-3f^{s,-}_{i+k-1}+3f^{s,-}_{i+k}-f^{s,-}_{i+k+1}, \quad k=2,1,0,
\end{aligned}
\tag{28}
$$

and $\omega^{+/-}$ are nonlinear weights in the WENO5 scheme.

In smooth regions the WENO5 scheme reduces to the explicit 5th-order linear upwind scheme, and Eq. (27) can be simplified as

$$
\begin{aligned}
\tilde{F}_{i+\frac{1}{2}} &= \frac{1}{60}(F_{i-2}-8F_{i-1}+37F_i+37F_{i+1}-8F_{i+2}+F_{i+3})\\
&\quad+\frac{1}{60}\tilde{R}_{i+\frac{1}{2}}\Lambda\tilde{L}_{i+\frac{1}{2}}\underbrace{(U_{i-2}-5U_{i-1}+10U_i-10U_{i+1}+5U_{i+2}-U_{i+3})}_{\text{dissipation part}},
\end{aligned}
\tag{29}
$$

where $\tilde{L}$ and $\tilde{R}$ correspond to the eigensystem of Eqs. (7) and (8) for the fully coupled scheme, while the proposed decoupled scheme has the eigensystem

$$
\begin{aligned}
\tilde{L}_{\mathrm{d}} &= \begin{pmatrix}\tilde{L}_1 & \\ & \tilde{L}_2\end{pmatrix} = \begin{pmatrix}\tilde{L}_1 & \\ & \mathbb{I}\end{pmatrix} \quad \text{and}\\
\tilde{R}_{\mathrm{d}} &= \begin{pmatrix}\tilde{R}_1 & \\ & \tilde{R}_2\end{pmatrix} = \begin{pmatrix}\tilde{R}_1 & \\ & \mathbb{I}\end{pmatrix}
\end{aligned}
\tag{30}
$$

by combining Eqs. (25) and (26). Using a different eigensystem merely affects the dissipation part which is $\mathcal{O}(\Delta x^5)$.

To discuss the convergence of the proposed decoupled scheme, without loss of generality, we consider the flow in 1D with three species. Assuming that the flow is advected with constant velocity and pressure, the multi-species Euler equations in Eq. (1) can be linearized with

$$
U = \left(\rho, \rho u, \rho e_t, \rho y_1, \rho y_2\right)^T.
$$

By denoting the 5th-order dissipation term as

$$
\delta U = \left(\delta\rho, u\delta\rho, \delta\rho e_t, \delta\rho y_1, \delta\rho y_2\right)^T \sim \mathcal{O}(\Delta x^5)
$$

and using different eigensystems for the fully coupled scheme and the decoupled scheme, respectively, we can see that the difference between the two derived convective fluxes is bounded as

$$
\begin{aligned}
||\tilde{F}^{\mathrm{d}}_{i+\frac{1}{2}}-\tilde{F}_{i+\frac{1}{2}}||_2 &= ||\frac{1}{60}\left(\tilde{R}^{\mathrm{d}}_{i+\frac{1}{2}}\Lambda\tilde{L}^{\mathrm{d}}_{i+\frac{1}{2}}-\tilde{R}_{i+\frac{1}{2}}\Lambda\tilde{L}_{i+\frac{1}{2}}\right)\delta U||_2\\
&= ||\frac{1}{60}\begin{pmatrix}0 & 0 & 0 & 0 & 0\\ -b_1c^2y_1z_1 & 0 & 0 & b_1c^2z_1 & b_1c^2z_2\\ -b_1c^2uy_1z_1+uy_2z_2 & 0 & 0 & b_1c^2uz_1 & b_1c^2uz_2\\ uy_1 & -y_1 & 0 & 0 & 0\\ uy_2 & -y_2 & 0 & 0 & 0\end{pmatrix}\delta U||_2\\
&\le \frac{1}{60}||\begin{pmatrix}0 & 0 & 0 & 0 & 0\\ -b_1c^2y_1z_1 & 0 & 0 & b_1c^2z_1 & b_1c^2z_2\\ -b_1c^2uy_1z_1+uy_2z_2 & 0 & 0 & b_1c^2uz_1 & b_1c^2uz_2\\ uy_1 & -y_1 & 0 & 0 & 0\\ uy_2 & -y_2 & 0 & 0 & 0\end{pmatrix}||||\delta U||_2\\
&\sim \mathcal{O}(\Delta x^5).
\end{aligned}
\tag{31}
$$

Through the detailed flux difference

$$
\tilde{F}^{\mathrm{d}}_{i+\frac{1}{2}}-\tilde{F}_{i+\frac{1}{2}} = \frac{1}{60}\begin{pmatrix}0\\ b_1c^2(\delta\rho y_1z_1+\delta\rho y_2z_2)-b_1c^2y_1z_1\delta\rho\\ b_1c^2u(\delta\rho y_1z_1+\delta\rho y_2z_2)-b_1c^2uy_1z_1\delta\rho+uy_2z_2\delta\rho\\ 0\\ 0\end{pmatrix},
\tag{32}
$$

we can see that the decoupled scheme introduces the same numerical dissipation for total density and partial density terms as the fully coupled scheme. Relating these properties to the component-wise FD scheme [24] with eigensystem $L=R=\mathbb{I}$, in which WENO interpolation is performed directly for each component of U in the physical space, we obtain

$$
\tilde{F}^{\mathrm{c}}_{i+\frac{1}{2}}-\tilde{F}^{\mathrm{d}}_{i+\frac{1}{2}} = \frac{1}{60}\begin{pmatrix}-c\delta\rho\\ (Hb_1-1)c^2\delta\rho-b_1c^2\delta\rho e_t\\ u((Hb_1-1)c^2\delta\rho-b_1c^2\delta\rho e_t)+c\delta\rho e_t\\ 0\\ 0\end{pmatrix},
\tag{33}
$$

such that an additional dissipation error of $-c\delta\rho$ is introduced to the total density term as compared to the decoupled scheme and the fully coupled characteristic-wise scheme.

Therefore, for the proposed decoupled scheme, we observe:

- **Consistency.** The derived numerical flux not only approaches that of the fully coupled scheme but also the physical flux $F(U)$ as δU vanishes when $\Delta x\to 0$, according to Eq. (31).
- **Stability.** Stability is ensured based on the upwind reconstruction with the local lax-Friedrichs splitting in Eq. (27) under the CFL condition [24].
- **Convergence.** Since the order of the dissipation error $\mathcal{O}(\Delta x^5)$ does not change, the high-order accuracy of WENO5 scheme in the present context is preserved.

A numerical example of advection flow testing the convergence rate of the decoupled scheme will be given in the following section.

2.2.2. Consistent update of species mass fractions

Assuming that we have updated the total variables of gas mixture according to the above partial characteristic scheme from time level n to $n+1$, i.e.

$$
\{\rho, \rho u, \cdots, \rho e_t\}^n \to \{\rho, \rho u, \cdots, \rho e_t\}^{n+1},
\tag{34}
$$

we now advance $\{\rho y_1, \cdots, \rho y_{N_s-1}\}^n$ to $\{\rho y_1, \cdots, \rho y_{N_s-1}\}^{n+1}$. As the total density has already been computed separately from the partial densities of species, a consistency error arises due to operator splitting, such that ρ in $(\rho y_i)^{n+1}$ at the new time level is not necessarily equal to ρ^{n+1} of Eq. (34), i.e.

$$
y_i^{n+1} \neq \frac{(\rho y_i)^{n+1}}{(\rho)^{n+1}}, \quad i=1,\cdots,N_s-1.
\tag{35}
$$

This inconsistency may introduce errors in computing species mass fractions, leading to oscillations around discontinuities such as contacts or shock waves.

It is known that all species are synchronously advected at velocity M across the cell face and transported into the same gas mixture ρ. Thus species information can be updated to reproduce a nominal total density to avoid the inconsistent ρ^{n+1} by

$$
y_i^{n+1} = \frac{(\rho y_i)^{n+1}}{\sum_{i=1}^{N_s}(\rho y_i)^{n+1}}.
\tag{36}
$$

A total number of N_s species mass equations needs to be solved by adding a mass equation for the N_sth species. Another advantage

Table 1
Numbers of species in the kinetic mechanisms used.

Main species	No. of species	References
H_2[a]	9	[20]
CH_4	53	[27]
n-C_7H_{16}	561	[4,5]
n-$C_{16}H_{34}$	2115	[30]

[a] The inert species is either N_2 or Ar as the 9th species. For the rest three mechanisms, both N_2 and Ar have been included.

of this treatment is that total mass can be conserved by enforcing $\sum_{i=1}^{N_s} y_i^{n+1} = 1$ in the denominator.

In two situations often encountered in practice, no extra effort is needed to deal with the N_sth species' mass equation:

- Some inert species such as N_2 or Ar is involved in the gas mixture and the index number of one inert species is set as N_s. The mass fraction of the inert species y_{N_s} should be constant in the entire flowfield at any time. This is the case when we consider a free stream of premixed fuel/air mixture including N_2 flows over structures, e.g. wedges, cylinders and blunt bodies, etc. In such cases, Eq. (36) can be replaced by

$$\begin{aligned} y_i^{n+1} &= \frac{(\rho y_i)^{n+1}}{\sum_{i=1}^{N_s}(\rho y_i)^{n+1}}, \\ &= \frac{(\rho y_i)^{n+1}}{\sum_{i=1}^{N_s-1}(\rho y_i)^{n+1}/(1-y_{N_s})}. \end{aligned} \tag{37}$$

- Regarding some mechanisms that involve many species, inert species exist but not with index N_s and the mass fraction of the N_sth species can be assumed to be zero, i.e. $y_{N_s} \equiv 0$. For example, if we only consider hydrogen/air combustion using the GRI-Mech 3.0 mechanism [27], which is designed for detailed CH_4/air chemistry but also quite popular for hydrogen/air combustion simulations, all carbon-related species should be set to zero including the N_sth species CH_3CHO. Thus, Eq. (37) is also valid simply by setting $y_{N_s} = 0$.

Having updated the mass fractions of species involved, combination of ρ^{n+1} and $\{y_1, \cdots, y_{N_s-1}\}^{n+1}$ is performed to correct the inconsistent conserved variables by

$$(\rho y_i)^{n+1} = \rho^{n+1} y_i^{n+1}, \quad i = 1, \cdots, N_s - 1. \tag{38}$$

Both the above two special cases as well as a general situation which requires transporting all N_s species will be given illustrative examples in the following section.

3. Numerical results and discussion

In this section, we present numerical examples to illustrate the comparison of fully coupled characteristic-wise flux-splitting scheme (denoted as 'coupled' in the following figures and tables) and its partially decoupled counterpart (denoted as 'decoupled') in addition to a 2nd-order AUSMPW+ scheme [14] plus MUSCL interpolation (denoted as 'AUSM+MUSCL') based on the FV formulation, in which the Minmod limiter is used. In the characteristic decomposition based FD formulation, the fifth-order WENO-LLF scheme is implemented as previously described. Temporal integration utilizes the explicit second-order Runge–Kutta algorithm (RK2) with a fixed timestep given in each numerical experiment corresponding to the CFL number around 0.5–0.75. Both inert and reactive multi-species problems are taken into consideration, in 1D or 2D. Also, several kinetic mechanisms consisting of different numbers of species, listed in Table 1, are employed to describe species thermodynamics and transport properties if needed as well as chemical kinetics if reactions are switched on. It is to be noted that, for simplicity and without loss of generality, only hydrogen/air combustion is taken into consideration even though the detailed mechanisms are able to describe more than hydrogen-related reactions. The simple and efficient first-order Lie-Trotter operator-splitting scheme [17] is exploited for separating the source and convection terms. VODE [1] or CHEMEQ2 [18] has been implemented for integrating the ODE system of chemical source terms. All simulations are performed on a Intel Xeon E5-2620 v3 workstation using the MPI library for parallelization.

3.1. 1D and 2D vortex advection

The first test case aims to verify quantitatively the spatial accuracy of the partially characteristic-wise flux-splitting scheme for the convection term discretization. It is expected that our proposed scheme may lead to larger errors due to operator splitting than the fully characteristic decomposition scheme. The relative error norms should reproduce high-order convergence rate as each part of the decoupled scheme is discretized by high-order WENO schemes.

The present example comes from the similar isentropic vortex case [6,9,31]. In the first Case 1a, we simplify the 2D vortex into a 1D advection flow of gas mixture composed of H_2, O_2 and N_2, with Gaussian profiles on the initial temperature and species mass fractions, i.e.

$$\begin{aligned} T &= T_0 - \frac{(\gamma_0 - 1)\Gamma^2}{8\gamma_0\pi}\exp\left(\frac{1-r^2}{2}\right), \\ y_{H_2} &= y_{H_2,0} - \frac{2\pi a_1}{\gamma_0\Gamma}\exp\left(\frac{1-r^2}{2}\right), \\ y_{O_2} &= y_{O_2,0} - \frac{2\pi a_2}{\gamma_0\Gamma}\exp\left(\frac{1-r^2}{2}\right), \\ y_{N_2} &= 1 - y_{H_2} - y_{O_2}, \end{aligned} \tag{39}$$

where $T_0 = 300$ K, $\Gamma = 50$, $\gamma_0 = 1.4$, $y_{H_2,0} = 0.01277$, $y_{O_2,0} = 0.101$, $a_1 = 0.005$, $a_2 = 0.03$ and $r = \sqrt{(x-x_0)^2 + (y-y_0)^2}$ in 2D or $r = x - x_0$ in 1D. In the first 1D case, the domain length $L = 10$ m and $x_0 = 5$ m. The uniform initial pressure and velocity is 101325 Pa and 100 m/s, respectively. At the domain boundaries, we apply periodic boundary condition, so that each cycle of the steady advection flow takes 0.1 s to recover its initial position periodically.

At t=0.1 s (1 cycle) and at t=1 s (10 cycles), the relative errors (compared with the initial conditions used as the exact solution) and the order of accuracy are evaluated for different numbers of grid points $N = 20, 40, 80$ and 100, respectively, in Fig. 1. For this purpose, a very small timestep, $\Delta t = 1 \times 10^{-6}$ s, is used for all grids to minimize temporal errors so that the resulted relative errors can be ascribed to using different spatial convection schemes. It can be found in Fig. 1 that

- As expected, both the coupled and decoupled schemes possess high-order accuracy in the L_1 and L_∞ error norms (5th order in black solid line) compared with the AUSM+MUSCL scheme (2nd order in red dash line).
- Error norms, using the same grid, of cycle 10 are about one order of magnitude larger than those of cycle 1, and the decoupled scheme produces insignificantly larger errors than the fully coupled scheme. In contrast, errors of the 2nd-order AUSM+MUSCL scheme are much larger than for the two high-order schemes based on the same grid.
- Mass fraction errors of species are much smaller than those in density by about two orders of magnitude. It seems that the decoupled scheme has more side effects upon calculating density than species mass fractions. Thus, their consistent update as proposed in the second special item due to $y_{N_s} \equiv 0$ is proved effective, without introducing large errors in calculating the mass fractions of species.

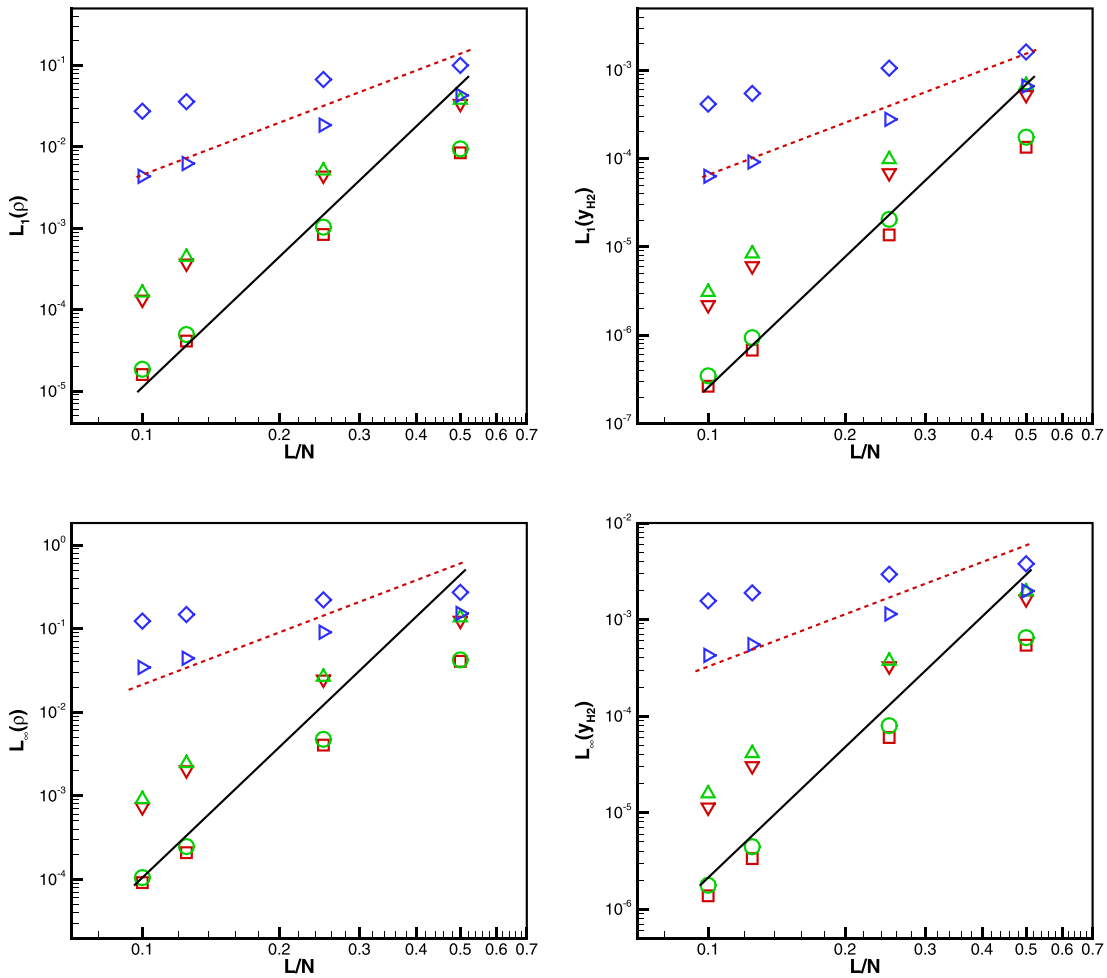

Fig. 1. Case 1a L_1 and L_∞ error norms of density and H_2 mass fraction. Gradient symbol: coupled scheme at $t = 0.1$; delta symbol: decoupled scheme at $t = 0.1$; diamond symbol: AUSM+MUSCL scheme at $t = 0.1$; cube: coupled scheme at $t = 1$; circle: decoupled scheme at $t = 1$; right triangle symbol: AUSM+MUSCL scheme at $t = 1$; black solid line indicates the 5th-order convergence rate and red dot line is 2nd-order. (For interpretation of the references to color in this figure legend, the reader is referred to the web version of this article.)

Table 2
Case 1a unit (step-averaged) CPU times for flux calculation (FC), primitive variable update (PU) and the total loop (TL) in one timestep with different number of species. Normalized CPU times are listed in every second line after the absolute CPU times based on the 9-species case.

	TL			FC			PU		
No. of species	Coupled	Decoupled	AUSM+MUSCL	Coupled	Decoupled	AUSM+MUSCL	Coupled	Decoupled	AUSM+MUSCL
9	0.001001428	0.000691545	0.000322301	0.000816926	0.000472868	0.000104714	0.000162475	0.000191890	0.000191411
	1	0.690558901	0.321841484	1	0.578838754	0.128180542	1	1.181042831	1.178089954
53	0.005822255	0.002325356	0.000923330	0.005230315	0.001698632	0.000320141	0.000521771	0.000555966	0.000531520
	5.813953891	2.322041139	0.922013207	6.402436594	2.079298214	0.391884692	3.211382682	3.421844301	3.271386220
561	0.393229030	0.021078206	0.007802374	0.387916709	0.016213795	0.002842758	0.004757007	0.004356738	0.004441574
	392.6683900	21.04815371	7.791249747	474.8494311	19.84733116	3.479824585	29.27832062	26.81474859	27.33689988
2115	19.84175359	0.084508152	0.032452066	19.81976696	0.062745469	0.011209302	0.019376990	0.019574005	0.018975126
	19813.46452	84.38766582	32.40579797	24261.40678	76.80682372	13.72132357	119.2610550	120.4736384	116.7876716

Having verified the high-order spatial accuracy of the proposed scheme, we also present the comparison of CPU time costs in terms of different numbers of species from 9 up to 2115 species, as listed in Table 2 and plotted in Fig. 2, from the aspect of computational efficiency. In the table, the total CPU time cost per one averaged timestep (TL) is listed firstly, followed by the time costs for flux calculation (FC) and primitive variable update (PU), respectively. In the figure, only TL and FC of three spatial schemes are shown in relation with the number of species, in logarithmic scales. For the current non-reactive case,

- As seen in the table, TL is basically the sum of FC and PU. PU costs almost the same CPU time between the three spatial schemes at a specific number of species. As the number of species increases, PU grows approximately linearly.
- High-order schemes require obviously more time in FC. More importantly, increasing the number of species increases the CPU time used for FC faster than PU. Thus, TL mainly depends on the contribution of FC for both high-order schemes and larger numbers of species.

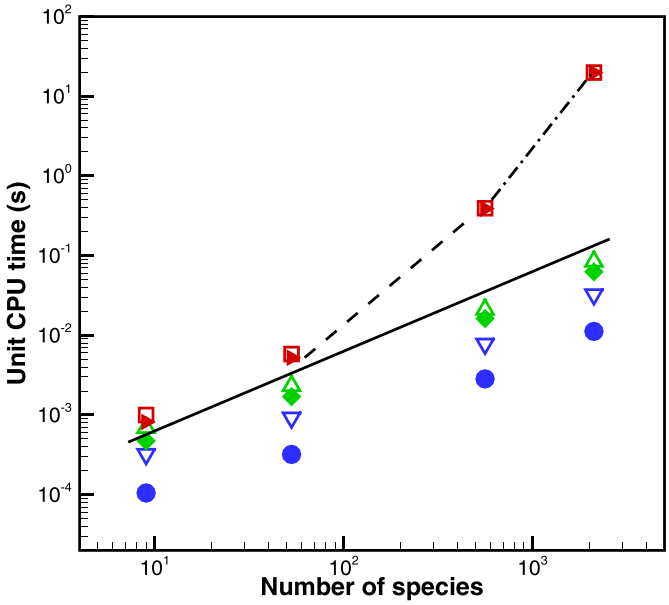

Fig. 2. Case 1a unit (step-averaged) CPU-times using 9, 53, 561 and up to 2115 species (N_s), respectively. All computations run until $t = 0.1$ for 100,000 uniform steps with 100 grid points. Red cube: TL by coupled scheme; red solid right triangle: FC by coupled scheme; green delta: TL by decoupled scheme; green solid diamond: FC by decoupled scheme; blue gradient symbol: TL by AUSM+MUSCL scheme; blue solid circle: FC by AUSM+MUSCL scheme. Solid black line: $O(N_s)$; dash black line: $O(N_s^2)$; dot dash black line: $O(N_s^3)$. (For interpretation of the references to color in this figure legend, the reader is referred to the web version of this article.)

- For both TL and FC the coupled scheme depends super-linearly on the number of species. The decoupled scheme is linearly related to the number of species as is the AUSM+MUSCL scheme. The linear scaling between the CPU time and the number of species renders the present decoupled scheme more efficient.

Next, Case 1b continues to consider the 2D isentropic vortex advection in a squared domain of 10 m-long sides. This 2D case is more difficult than Case 1a since the vortex flow is not at rest in the vertical direction. At $t = 0$ s, an inviscid vortex of radius $r = 5$ is placed at the domain center by

$$u = u_0 - \frac{\Gamma}{2\pi}\exp\left(\frac{1-r^2}{2}\right)(y - y_0),$$
$$v = v_0 + \frac{\Gamma}{2\pi}\exp\left(\frac{1-r^2}{2}\right)(x - x_0), \tag{40}$$

where $u_0 = 100, v_0 = 0$ and $x_0 = y_0 = 5$. Other parameters for the initial 2D flowfield is also provided by Eq. (39). Two sets of grids, 100×100 and 200×200, are employed. At $t = 0.1$ s (1 cycle), the isolines of density, vertical velocity and mass fraction of H_2 are plotted in Fig. 3. We can see that both the decoupled and coupled schemes can capture accurately isolines of all three variables. Due to its high numerical dissipation, results of the AUSM+MUSCL scheme are not shown in the figure.

3.2. Sod's shock tube

The popular Riemann (Sod) shock tube problem is one of the most standard numerical benchmarks designed for compressible flow solvers [9,28]. It is mostly studied by implementing the single-species ideal gas model with a fixed $\gamma = 1.4$. Herein we test the multi-species solver by considering air to be the gas mixture of 21% O_2 and 79% N_2. Setup of the 1D flowfield is well-known, initially divided by two dimensionless states at the middle point, i.e.

$$(\rho, u, p)_L = (1, 0, 1), \quad \text{if } x \le 0.5,$$
$$(\rho, u, p)_R = (0.125, 0, 0.1), \quad \text{otherwise.} \tag{41}$$

We design the following dimensional quantities to mimic the classical shock tube, that is

$$(T, p)_L = (375\ \text{K}, 101,325\ \text{Pa}), \quad \text{if } x \le 0.5\ \text{m},$$
$$(T, p)_R = (300\ \text{K}, 10132.5\ \text{Pa}), \quad \text{otherwise}, \tag{42}$$

giving $\rho_L = 0.937561\text{kg/m}^3$ and $u_0 = \sqrt{p_L/\rho_L}$ for the normalization of velocity. The domain is discretized by 400 grid points and timestep is fixed at $\Delta t = 1 \times 10^{-6}$ s, corresponding to the CFL number of about 0.5. Computation runs until $t = 6 \times 10^{-4}$ s, such that the result can be comparable with that at $t = 0.2$ in the dimensionless case of [9]. Two mechanisms of 9 and 53 species, respectively, are considered with all mass fractions except O_2 and N_2 are set to zero. For the 9-species mechanism, due to $y_{N_s} = y_{N_2} \equiv 0.767$, update of species mass fractions utilizes Eq. (37) in the first special item. For the 53-species mechanism, it follows the second special item due to $y_{N_s} = y_{CH_3CHO} \equiv 0$.

Fig. 4 shows the normalized variable profiles which agrees with [9]. With the same grid, both high-order low-dissipation schemes capture much sharper discontinuities than the AUSM+MUSCL scheme, where the decoupled scheme results match well with the coupled scheme. Both results of 9-species case and 53-species case exhibit identical profiles, which validates the proposed consistent update of species mass fractions.

3.3. Inert gas mixture shock tube

This modified version of the popular Sod's shock tube has been studied in [8] to verify the convection scheme together with the thermodynamics of a multi-species gas mixture. The 1D domain of length $L = 10$ cm is filled with $H_2/O_2/Ar$ mixture with a molar ratio of 2/1/7. The initial conditions correspond to the following Riemann problem:

$$(T, p)_L = (400\ \text{K}, 8000\ \text{Pa}),$$
$$(T, p)_R = (1200\ \text{K}, 80,000\ \text{Pa}). \tag{43}$$

400 grid points are used to discretize the domain and timestep here is fixed at $\Delta t = 1 \times 10^{-7}$ s, corresponding to the CFL number of about 0.75. The computation runs for 400 steps until $t = 40$ μs. We also adopt two mechanisms with corresponding update of species mass fraction as in the Sod's shock tube example. To make clear the necessity of the present consistent mass fraction update method for the decoupled scheme, we additionally test the traditional way of updating the species mass as in Eq. (35).

Fig. 5 shows excellently agreement with [9] between three convection schemes, where the decoupled scheme utilizes the consistent update of mass fractions according to the mechanism used. However, for the species-dependent specific heat ratio, γ, in Fig. 6, oscillations are visible around the shock as a result of the inconsistent mass-fraction update in the decoupled scheme. This is also observed in the profile of y_{H_2}, which is supposed to be constant throughout the tube. This property is also presented for the fully coupled scheme and AUSM+MUSCL scheme. Using the proposed consistent update, the decoupled scheme successfully avoids the occurrence of any spurious oscillations.

3.4. Reactive gas mixture shock tube

This case was investigated previously by Oran et al. [21] and serves to evaluate the performance of multi-species compressible chemically reacting flow solvers in [7–9]. A reactive gas mixture is placed in a closed tube, in which a shock hits the left-side

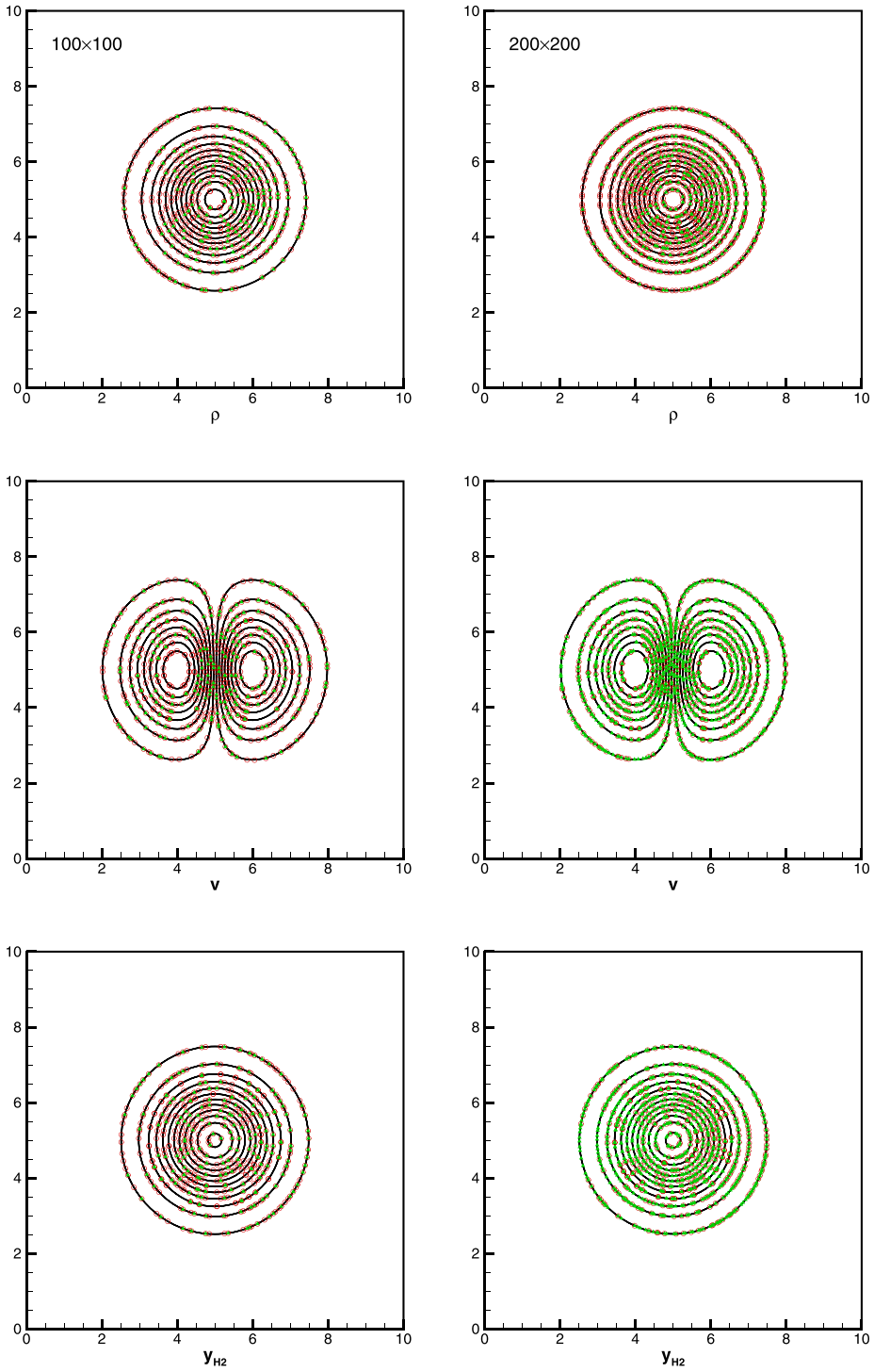

Fig. 3. Case 1b sampled contour lines of coupled and decoupled schemes regarding density, y-velocity and H_2 mass fraction. Left side: 100×100 cells; right side: 200×200 cells. Red circle: coupled scheme at $t = 0.1$; solid green delta symbol: decoupled scheme at $t = 0.1$. Black solid line: exact solution. (For interpretation of the references to color in this figure legend, the reader is referred to the web version of this article.)

solid wall boundary and reflects off. A reaction wave occurs at the boundary after a delay of induction, then catches up and merges with the right-moving shock wave to develop a detonation wave.

The reactive mixture is considered to be characterized by a 2/1/7 molar ratio of $H_2/O_2/Ar$. Initial conditions are

$$(\rho, u, p)_L = (0.072\ \text{kg/m}^3, 0\ \text{m/s}, 7173\ \text{Pa}),$$
$$(\rho, u, p)_R = (0.18075\ \text{kg/m}^3, -487.34\ \text{m/s}, 35,594\ \text{Pa}), \quad (44)$$

with the left and right states being separated in the middle of a 12 cm-long domain discretized with 400 grid points. Wall boundary condition is applied for the left end of tube while the right end uses outflow condition. In all runs, the timestep is fixed at $\Delta t = 1 \times 10^{-7}$ s, corresponding to a CFL number of about 0.75. Also, both 9-species and 53-species mechanisms are considered with reactions switched on. VODE as the integrator of ODE system of chemical reactions is used here without excessive computational

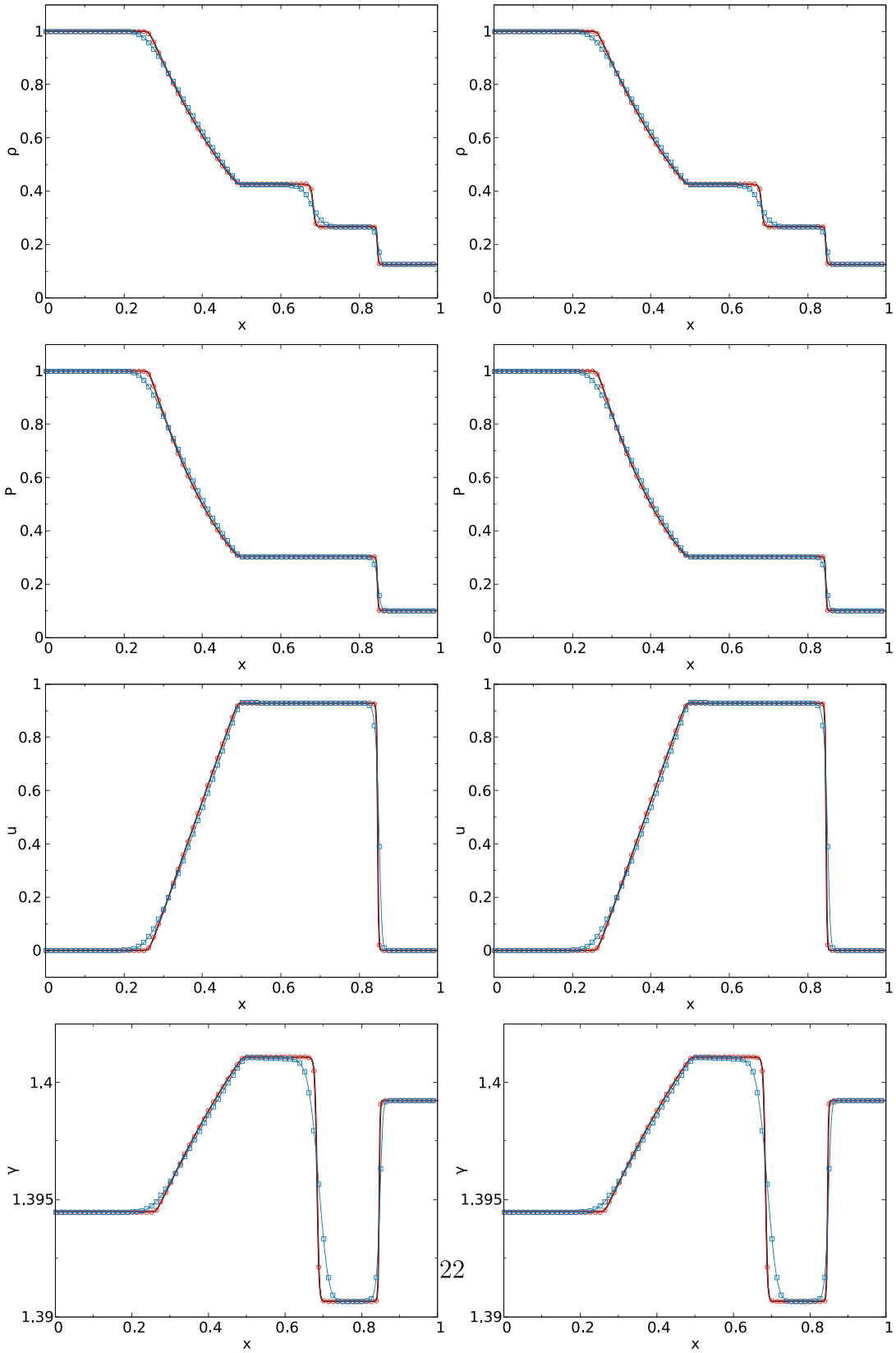

Fig. 4. Case 2 Sod's shock tube of $21\%H_2 + 79\%N_2$ gas mixture. Left: 9 species case; right: 53 species case. Black solid line: coupled scheme; red circle line: decoupled scheme; blue cube line: AUSM+MUSCL scheme. (For interpretation of the references to color in this figure legend, the reader is referred to the web version of this article.)

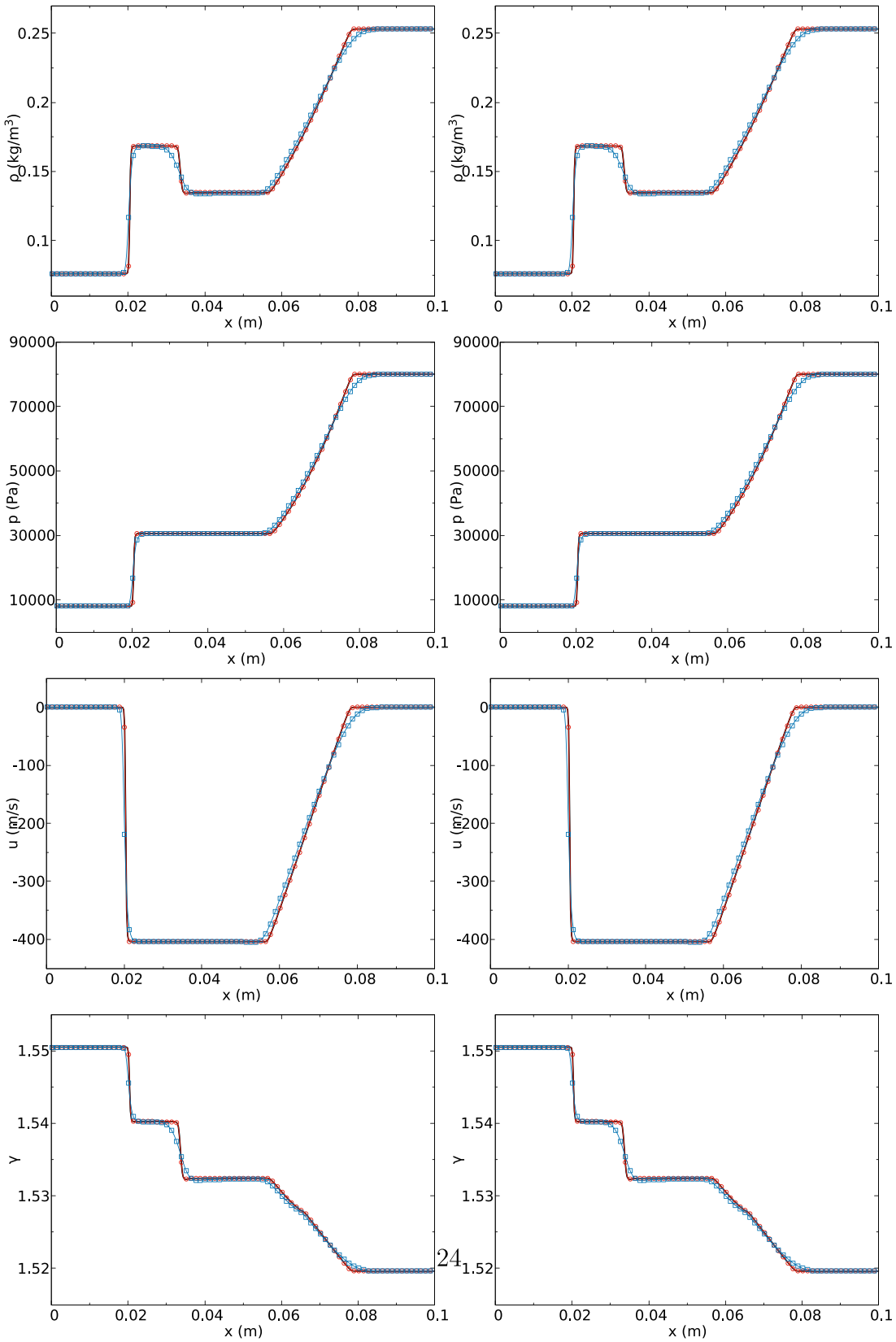

Fig. 5. Case 3 inert shock tube of $H_2/O_2/Ar$ gas mixture with initial ratio of 2: 1: 7 at $t = 40$ μs. Left: 9 species case; right: 53 species case. Black solid line: coupled scheme; red circle line: decoupled scheme; blue cube line: AUSM+MUSCL scheme. (For interpretation of the references to color in this figure legend, the reader is referred to the web version of this article.)

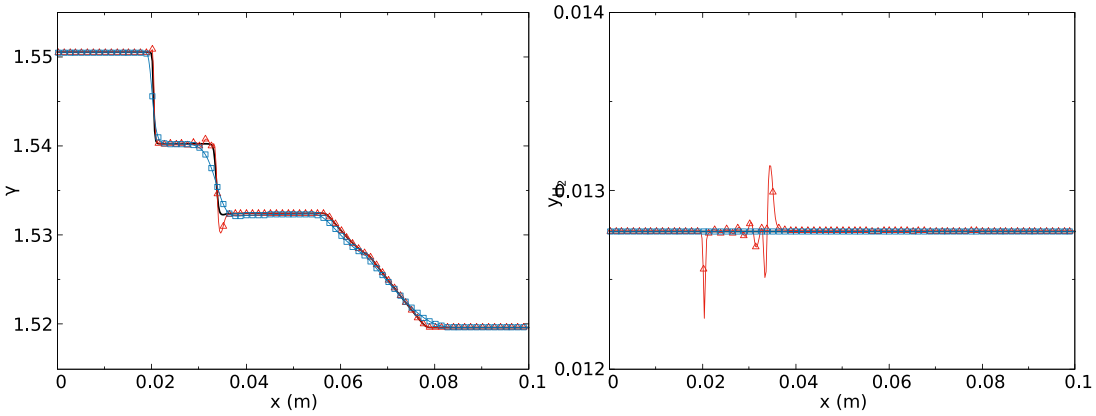

Fig. 6. Case 3 inert shock tube problem of $H_2/O_2/Ar$ gas mixture with initial ratio of 2: 1: 7 at $t = 40$ μs. Black solid line: coupled scheme; red triangle line: decoupled scheme; blue cube line: AUSM+MUSCL scheme. The decoupled scheme here employs the inconsistent mass-fraction update, leading to oscillations in y_{H_2} and γ. (For interpretation of the references to color in this figure legend, the reader is referred to the web version of this article.)

Table 3
Case 4 unit (step-averaged) CPU times for flux calculation (FC), ODE integration by VODE (vode) and the total loop (TL) in one timestep using two mechanisms

	TL			FC			vode		
No. of species	Coupled	Decoupled	AUSM+MUSCL	Coupled	Decoupled	AUSM+MUSCL	Coupled	Decoupled	AUSM+MUSCL
9	0.015763691	0.014487363	0.013004980	0.003222557	0.001953609	0.000460801	0.011083957	0.011044850	0.011098304
	1	0.919033694	0.824995851	1	0.606229377	0.142992312	1	0.996471712	1.001294389
53	0.193266271	0.176292764	0.173204538	0.021329382	0.007134122	0.001529770	0.167723207	0.165103592	0.167614087
	1	0.912175535	0.896196409	1	0.334473932	0.071721254	1	0.984381324	0.999349407

efforts in the 1D problem. Results are analyzed at $t = 170, 190$ and 230 μs, respectively.

In Fig. 7, we observe that for the reactive flow, different mechanisms show different results in predicting the time-dependent flow variables. It is obvious that using the 9-species mechanism gives a faster reacting front than the 53-species case, and the latter case matches very well with simulations in [8,9]. Especially at $t = 170$ μs, the reaction front in the 53-species case has not yet caught up with the moving shock wave while the reaction front in the 9-species case has almost merged with the shock wave and soon evolves into a detonation wave. For the same mechanism both high-order schemes are in good agreement with each other, although the AUSM+MUSCL scheme yields a slightly slower detonation wave than high-order schemes in the 9-species case. The slight oscillation in γ of the 53-species case at $t = 230$ μs is not due to inconsistency discussed in this study, which also can be observed in the Fig. 11 [9].

In Table 3, the consumed CPU times per timestep by different spatial schemes and mechanisms are listed in parts and illustrated in Fig. 8. It is readily to see that

- TL is the sum of FC and vode, but the latter obviously takes a great part of TL.
- Integrating the ODE system of chemical source terms with VODE takes almost the same CPU time between three schemes. The 53-species mechanism needs much more computational efforts than the 9-species mechanism.
- The decoupled scheme can still reduce the CPU time in FC compared with the coupled scheme, agreeing with the observations in Case 1a.

Since the chemical ODE part dominates the CPU time cost in a total loop (TL), the decoupled scheme exhibits the advantage of better accuracy at little sacrifice of computational efficiency, compared with the popular 2nd-order AUSM+MUSCL scheme. Therefore, for reactive flows, high-order convection schemes are a better choice weighing spatial accuracy and computational efficiency on a balanced scale. With the same high-order accuracy, the decoupled scheme requires less CPU time than the coupled scheme by approximately 10% in both 9-species and 53-species cases from Table 3.

3.5. 2D steady oblique detonation wave

This 2D case concerns the scenario that an oblique detonation wave (ODW) is induced by hypersonic reactive free-stream past a wedge. Regarded as a promising combustion mechanism for hypersonic vehicles, ODW has received considerable attention and extensive numerical work [15,16,29] has been conducted. Our goal with this example here is not to analyze the specific mechanism behind, but to compare the high-order shock-capturing schemes, with full or partial characteristic decomposition. As the computational efficiency has been greatly improved for discretizing convection terms as proved in previous 1D examples (nonreactive or reactive), it is expected for the partial characteristic decomposition scheme to preserve accuracy in predicting the details of a reactive flowfield with complex structures including shock waves, detonation waves, reflected shock waves, expansion waves and slip lines, etc., with a certain kinetic mechanism. Fig. 9 displays a schematic of the corresponding ODW flowfield.

The computational setup considers Mach 8 reactive inflow consisting of H_2/air gas mixture of a stoichiometric molar ratio, and the acute angle between the inflow velocity direction and wedge is $\beta = 23^\circ$ [16]. The inflow temperature and pressure are 293 K and 101325 Pa, respectively. In the present simulations, the wedge is placed horizontally and the inflow hits it with a negative y-direction velocity v. Not applying a very fine grid as in [16], we find that uniformly distributed 360×180 grid points with $\Delta x = \Delta y = 0.2$ mm (10 times the resolution of the moderate grid used in [16]) are sufficient to reproduce most details of the flow structures and illustrate the advantage in accuracy of both high-order schemes over the 2nd-order AUSM+MUSCL scheme. For this steady flow, the CFL number is set to be 0.75 and each computation runs

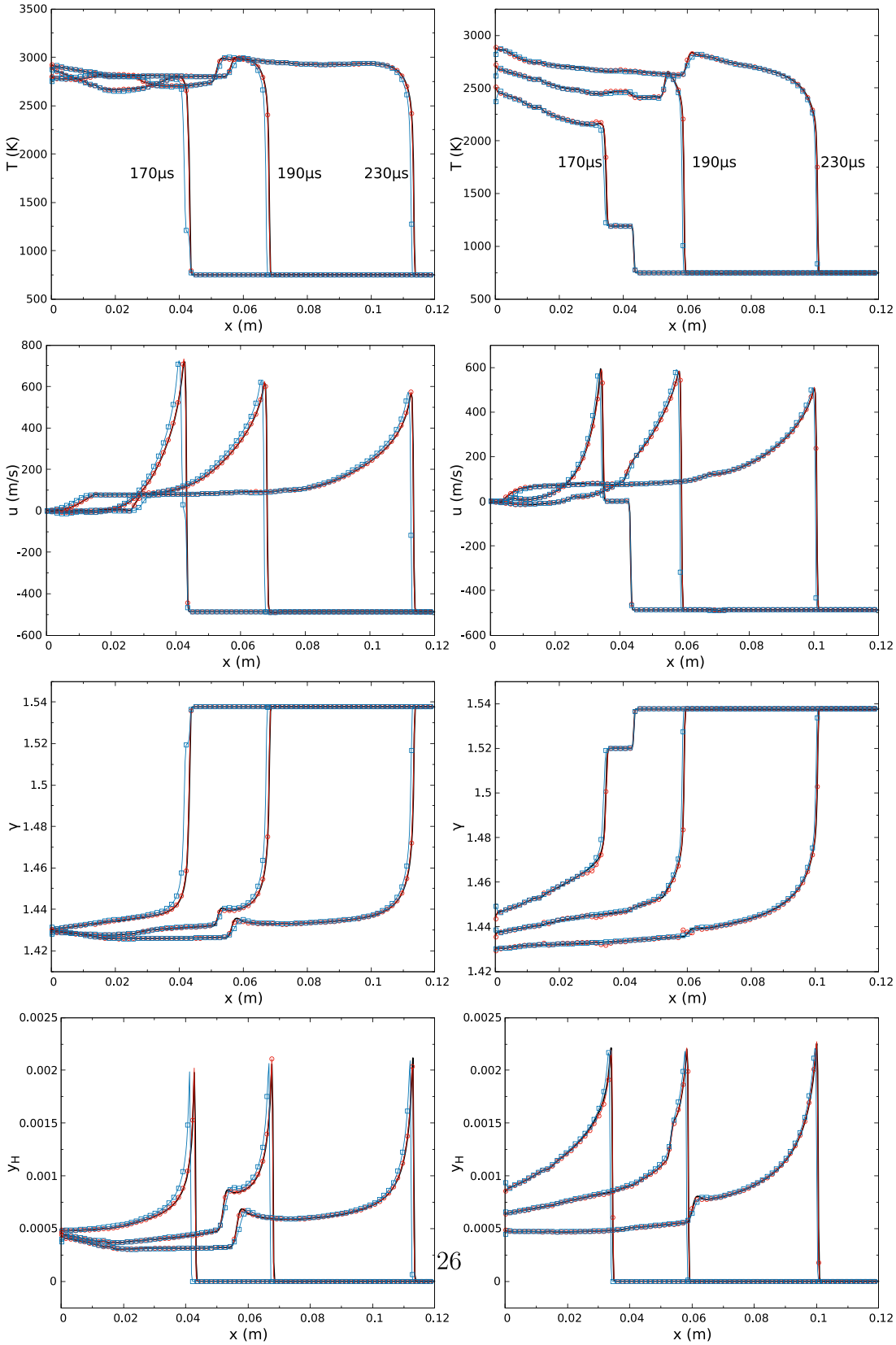

Fig. 7. Case 4 reactive shock tube of $H_2/O_2/Ar$ gas mixture with initial ratio of 2: 1: 7. Left: 9 species case; right: 53 species case. Black solid line: coupled scheme; red circle line: decoupled scheme; blue cube line: AUSM+MUSCL scheme. (For interpretation of the references to color in this figure legend, the reader is referred to the web version of this article.)

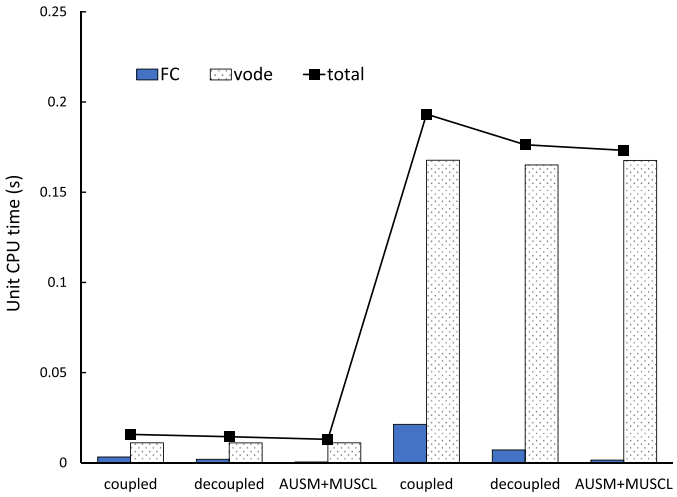

Fig. 8. Case 4 unit (step-averaged) CPU times using 9 and 53 species, respectively.

with variable timesteps until it develops a steady state. In this case we found that the 9-species mechanism fails to induce the oblique detonation wave behind the leading-edge oblique shock wave. Consequently, we use another reduced kinetic mechanism of Evans et al. [23], with 7 species and 8 reactions, which leaves out H_2O_2 and HO_2.

Fig. 10 shows the steady ODW flowfields with three different convection schemes. Despite the similarity of three steady flowfields, it can be seen that the upper two high-order schemes exhibit much sharper shock wave as well as the oblique detonation wave. In the meantime, expansion waves from the triple point and its reflection from the bottom boundary are captured by high-order schemes, being smeared by the 2nd-order AUSM+MUSCL scheme. In the temperature contours of high-order schemes, slip lines are also apparent and separate the temperature field into a upper post-detonation high-temperature zone and a post-expansion low-temperature zone free of combustion. It is reasonable that different induction length and angle of ODW are computed in the present simulations from the results of a similar case in [16], which employs a simple two-step chemistry.

Fig. 11 shows two cross-sectional profiles of variables attached to and 6 mm away from the bottom boundary, respectively. From the pressure and temperature profiles, we can see that the AUSM+MUSCL scheme yields longer induction of combustion starting from the leading edge. Both high-order schemes give much higher pressure and temperature peaks than the 2nd-order scheme. Between the two high-order schemes, the proposed decoupled scheme matches well with the fully coupled scheme, except for peaks of pressure and mass fraction of OH, due to the inherent splitting error. Nevertheless, the splitting error is acceptable as it is smaller than the difference between AUSM+MUSCL scheme and the high-order schemes in general.

Table 4
Parameters of mixing layer/shock interaction in Case 6.

Parameter	Upper fuel	Lower oxidizer	Bottom boundary inflow[a]
Pressure (Pa)	94232.25	94232.25	129951.0
Temperature (K)	545.0	1475.0	1582.6
U (m/s)	973.0	1634.0	1526.3
V (m/s)	0.0	0.0	165.7
Mass fraction	–	–	–
H_2	0.05	0.0	0.0
O_2	0.0	0.278	0.278
H_2O	0.0	0.17	0.17
H	0.0	5.60×10^{-7}	5.60×10^{-7}
O	0.0	1.55×10^{-4}	1.55×10^{-4}
OH	0.0	1.83×10^{-3}	1.83×10^{-3}
HO_2	0.0	5.10×10^{-6}	5.10×10^{-6}
H_2O_2	0.0	2.50×10^{-7}	2.50×10^{-7}

[a] The bottom boundary inflow is injected to produce the incident oblique shock wave.

3.6. 2D unsteady mixing layer/shock interaction

Unlike the steady case in the former example, this 2D test case considers the time-dependent development of the mixing layer constrained between two incoming supersonic free-streams with different gas components and velocities. An additional difficulty for numerical simulation is introduced by creating an incident oblique shock from the bottom boundary, which interacts with the mixing layer, reflects at the upper boundary, and thus produces a series of discontinuities across the flowdfield. High-order FD WENO schemes, which have been implemented in [2,9], facilitate numerical investigations of such a flow problem. We are interested in comparing the results of two high-order schemes and the AUSMPW+ plus MUSCL interpolation scheme with the same setup. The configuration of this example has an upper inlet stream associated with fuel injection and a lower inlet stream associated with oxidizer. Fig. 12 provides the sketch of 2D flowfield as well as boundary conditions, and Table 4 details the values of parameters for the flowfield setup. The upper and lower inflows are initialized with a hyperbolic tangent profile for the streamwise velocity component u, while the transverse velocity v is fixed at zero:

$$u(x,y) = 0.5\left[(U_F + U_O) + (U_F - U_O)\tanh\left(\tfrac{2y}{\delta_0}\right)\right], v(x,y) = 0, \quad (45)$$

using the parameters for U_F and U_O in Table 4 and the velocity thickness $\delta_0 = 1.44 \times 10^{-4}$ m. Based on the velocity thickness, the size of the 2D domain is $275\delta_0 \times 120\delta_0$. Also, the inflow tempera-

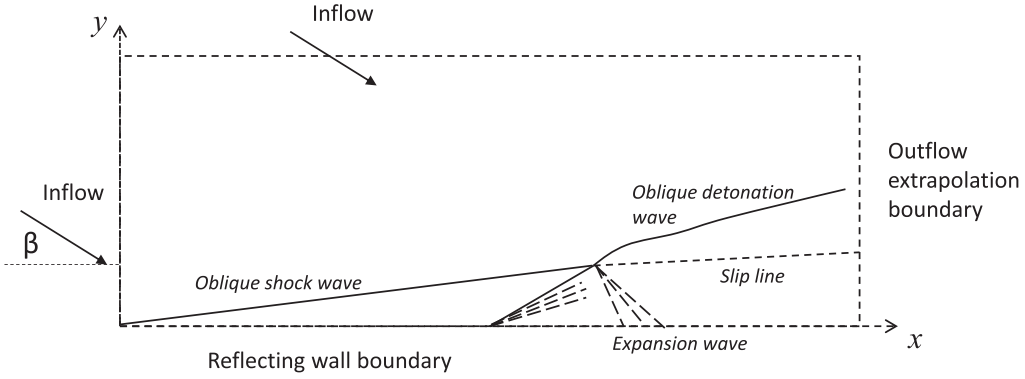

Fig. 9. Sketch of oblique detonation wave flowfield in Case 5.

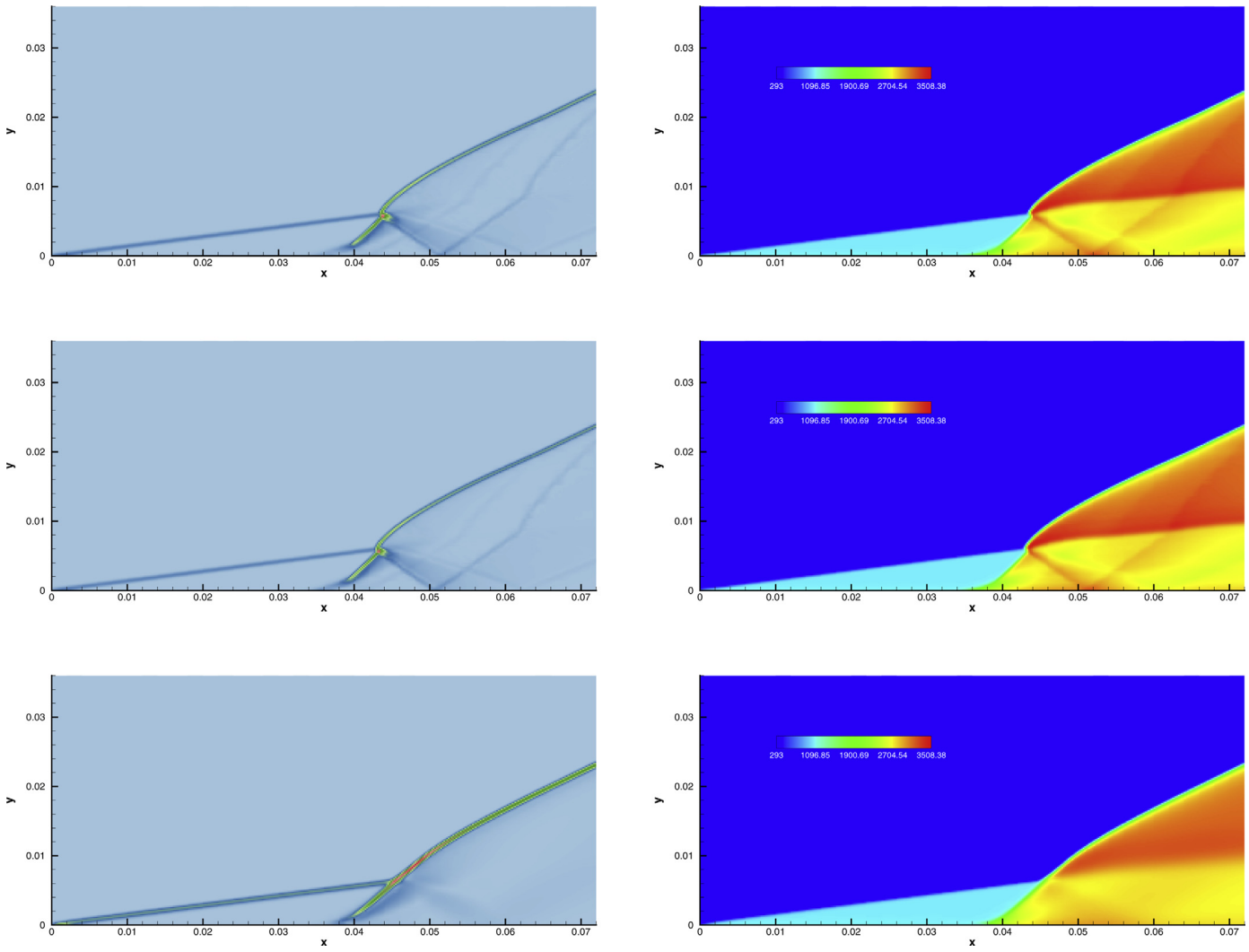

Fig. 10. Case 5 oblique detonation wave (ODW) problem: steady fields of pressure gradient magnitude (left) and temperature (right). From top to bottom is the coupled, decoupled and AUSM+MUSCL solution, respectively.

Table 5
Case 6 unit CPU times for flux calculation (FC), ODE integration by CHEMEQ2 and the total loop (TL) in one timestep.

	TL			FC			chemeq2		
	Coupled	Decoupled	AUSM+MUSCL	Coupled	Decoupled	AUSM+MUSCL	Coupled	Decoupled	AUSM+MUSCL
Non-reactive	0.795574554	0.640063596	0.400028087	0.496905570	0.335797850	0.085914843	–	–	–
	1	0.804529999	0.502816593	1	0.675777995	0.172899739	–	–	–
Reactive	0.98550638	0.824708525	0.535306252	0.51252713	0.339152340	0.086027376	0.13886178	0.133302706	0.134831354
	1	0.836837327	0.543178880	1	0.661725635	0.167849409	1	0.959966851	0.970975264

ture and mass fractions of species are set in a similar fashion, i.e.

$$T(x,y) = 0.5\left[(T_F + T_O) + (T_F - T_O)\tanh\left(\frac{2y}{\delta_0}\right)\right],$$
$$y_i(x,y) = 0.5\left[(y_{F,i} + y_{O,i}) + (y_{F,i} - y_{O,i})\tanh\left(\frac{2y}{\delta_0}\right)\right],$$
$$i = 1, \cdots, N_s - 1, \tag{46}$$

with $y_{N_2} = 1 - \sum_{i=1}^{N_s-1} y_i$ for mass conservation. A total number of 9 species are advected by the 9-species 21-reaction kinetic mechanism. Inflow pressure is uniformly distributed alone the inlet. A perturbation is additionally imposed on the transverse velocity v as in [2] by

$$v' = \sum_{k=1}^{2} a_k \cos\left(\frac{2\pi kt}{t_0} + \phi_k\right)\exp\left(\frac{-y^2}{b}\right), \tag{47}$$

where the period $t_0 = L_x/u_c$ and other parameters are given by $b = 10$, $a_1 = a_2 = 0.05$, $\phi_1 = 0$ and $\phi_2 = \pi/2$. For all computations, a uniform grid of 800×350 points is used together with a fixed timestep of $\Delta t = 1 \times 10^{-8}$ s for accurate and stable integration of the chemical ODE system.

First, we consider the non-reactive case: after 60,000 uniform timesteps using the full characteristic flux-splitting scheme, the flowfield including mixing layer and shock waves is fully established as shown in the top-middle figure of Fig. 13, based on which we now continue three computations with different convection schemes for another 10,000 steps. At $t = 50$ and 100 μs, we obtain the corresponding flowfields in the rest figures of Fig. 13. From the pressure gradient magnitude field, we can see obvious shock waves and pressure perturbations in the high-order scheme results.

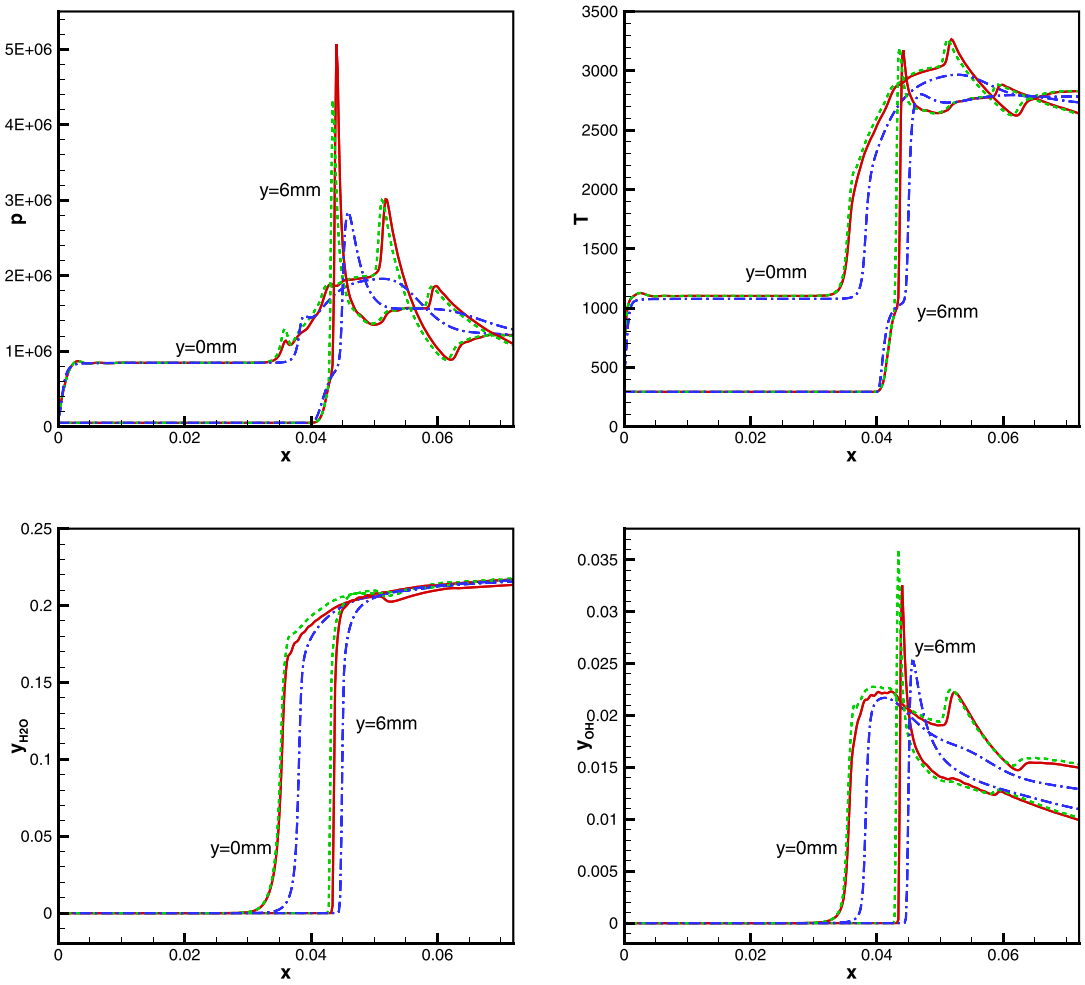

Fig. 11. Case 5 oblique detonation wave (ODW) problem: cross sectional profiles at two y-direction locations. Red solid line: coupled solution; green dash line: decoupled solution; blue dash dot line: AUSM+MUSCL solution. (For interpretation of the references to color in this figure legend, the reader is referred to the web version of this article.)

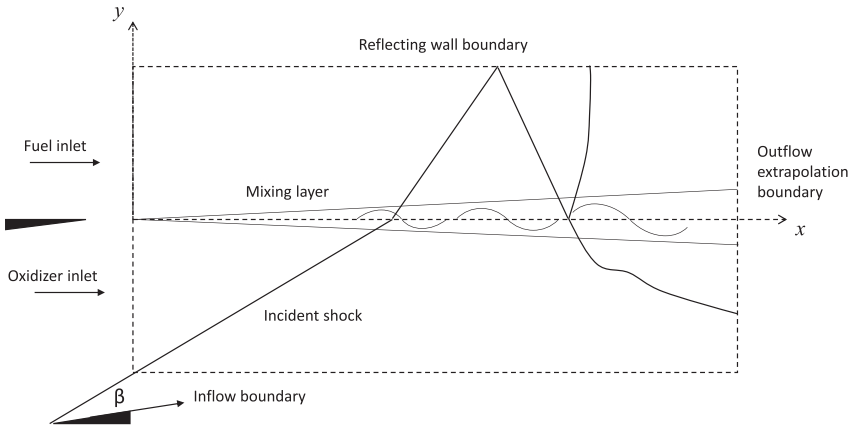

Fig. 12. Sketch of mixing layer/shock interaction in Case 6.

Vortex roll-up in the mixing layer is captured more precisely than in the AUSM+MUSCL results. In the bottom figures, the mixing layer is nearly smeared out by the 2nd-order scheme. Between the decoupled and coupled schemes, except some temperature spots inside the mixing layer, both unsteady flowfields are very similar.

Next, also based on the same initial flowfield at $t = 0$ s, we continue running three simulations by activating the chemical reactions for additional 10,000 steps. In order to diminish the computational efforts for solving the ODE system of chemical reactions, an explicit integrator, CHEMEQ2, instead of VODE, is employed here for the 2D reactive case. Different from the non-reactive case, in Fig. 14, the mass fraction of H_2O_2 isocontours instead of temperature is super-imposed on the field of pressure gradient magnitude. Except for the shaper shock-wave series, both two high-order schemes can give more details of the unsteady flow including the reaction intermediates such as H_2O_2 existing in the

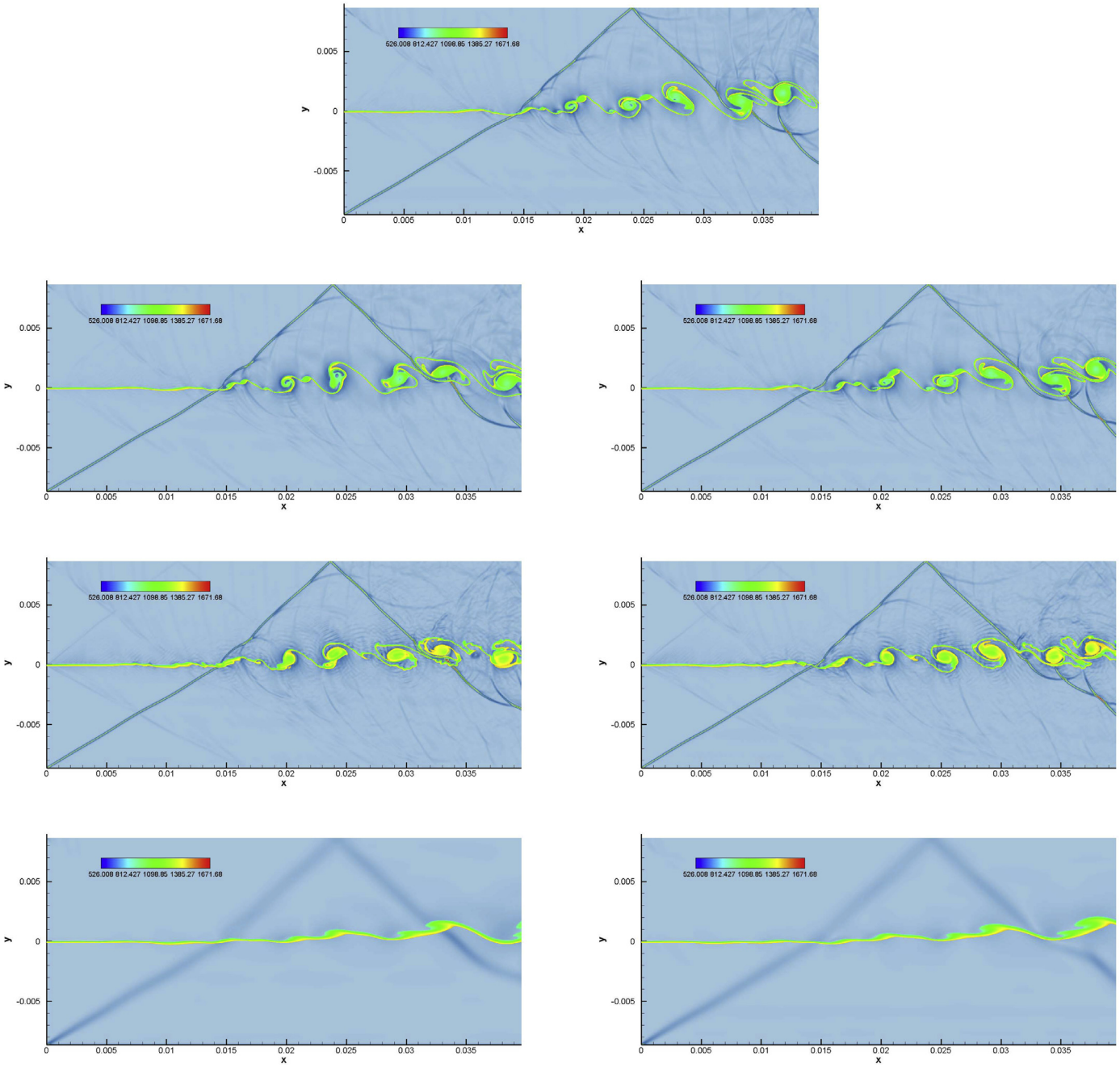

Fig. 13. Case 6 non-reactive mixing layer/shock interaction problem: fields of the pressure gradient magnitude superimposed with isocontours of temperature at two different times. Left: t=50 μs; right: 100 μs. The top-middle figure is a common established flowfield as the initial state at $t = 0$ s. From top to bottom is the coupled, decoupled and AUSM+MUSCL solution, respectively.

mixing layer where vortex-enhanced combustion occurs. However, the 2nd-order AUSM+MUSCL scheme underestimates the distribution of H_2O_2 in a much narrower reacting area. Regarding the present unsteady time-dependent reactive flow, the proposed decoupled scheme results yield slight differences from the coupled scheme for two possible reasons: one is due to errors of partial decomposition and the other lies in the 1st-order Lie-Trotter splitting errors together with the 2nd-order RK scheme for the convection part.

In Table 5, we list the averaged CPU time cost per timestep in each part for both non-reactive and reactive cases. The proposed decoupled scheme improves the time efficiency for FC by over 30%, compared with the fully coupled scheme, and for TL by nearly 20%. Since only 9 species are included, the efficiency gain of the decoupled scheme is limited. Time consumption of the AUSM+MUSCL scheme is low, which is accomplished at a considerably lower spatial accuracy.

4. Conclusions

We have presented a partial characteristic decomposition scheme for the solution of multi-species Euler equations with high-order finite difference schemes. Since the eigensystem of the multi-species convective flux Jacobian is sparse and non-zero entries in its matrices are mainly distributed along the diagonal, it is feasible to split the eigensystem into two parts: one is the gas mixture part, which is subject to traditional characteristic decomposition schemes for single-fluid Euler equations, and the other part

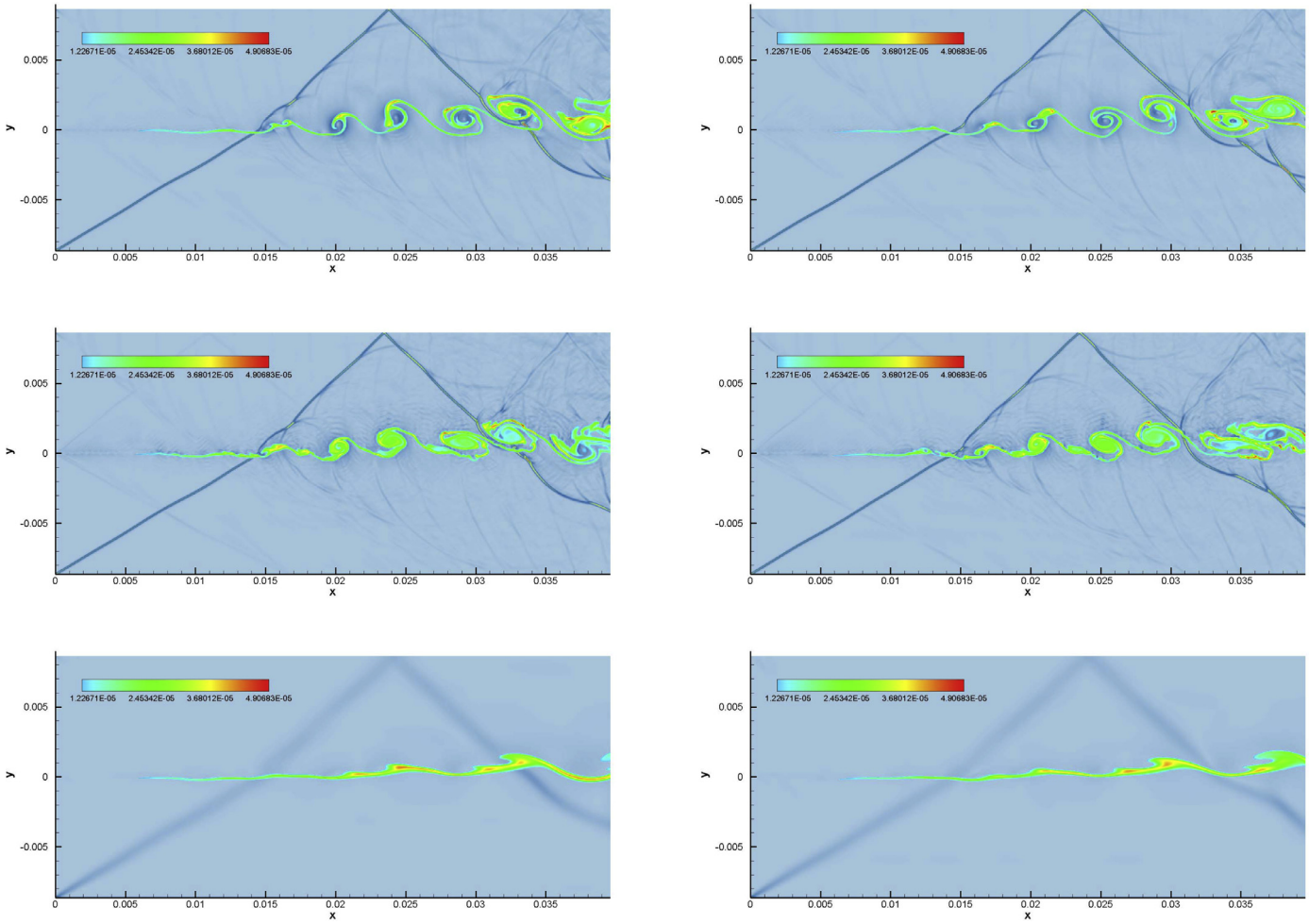

Fig. 14. Case 6 reactive mixing layer/shock interaction problem: fields of the pressure gradient magnitude superimposed with isocontours of mass fraction, $y_{H_2O_2}$,at two different times. Left: t=50 μs; right: 100 μs. From top to bottom is the coupled, decoupled and AUSM+MUSCL solution, respectively.

corresponds to a series of species partial mass equations. Since the species part has a sub-eigensystem of which the left and right sub-eigenmatrices are diagonal identity matrices, transforming the species variables from physical space onto characteristic space and back is no longer necessary, so that massive operations on matrix multiplication that is computationally very expensive can be avoided.

With extensive numerical examples, the proposed scheme manages to significantly reduce the computational cost for calculating the multi-species convective flux in the following two aspects:

- Computational cost of the full characteristic decomposition schemes depends super-linearly (quadratically even cubically) on the number of species involved.
- Similarly with the 2nd-order AUSM plus MUSCL scheme in the finite volume formulation, the linear scaling of the computational cost with different numbers of species is realized by the proposed decoupled scheme.

Despite the splitting error, since each decoupled part is still discretized by high-order schemes, the proposed scheme is verified to preserve the high-order accuracy of the underlying discretization scheme. The inconsistency issue in the update of species mass fractions has been resolved by summing up all the newly computed partial densities to reproduce a consistent nominal total density to be the base of renormalization. In contrast, using the straightforward update of mass fractions as the fully coupled scheme leads to spurious oscillations around discontinuities with large species gradients.

Acknowledgements

The financial support from the EU Marie Skłodowska-Curie Innovative Training Networks (ITN-ETN) (Project ID: 675528-IPPAD-H2020-MSCA-ITN-2015) for the first author is gratefully acknowledged. Xiangyu Y. Hu is also thankful for the partial support by National Natural Science Foundation of China(NSFC) (Grant No:11628206).

References

[1] Brown PN, Byrne GD, Hindmarsh AC. Vode: a variable-coefficient ode solver. SIAM J Scient Stat Comput 1989;10(5):1038–51.
[2] Chaudhuri A, Hadjadj A, Chinnayya A, Palerm S. Numerical study of compressible mixing layers using high-order weno schemes. J Sci Comput 2011;47(2):170–97.
[3] Črnjarić-Žic N, Vuković S, Sopta L. On different flux splittings and flux functions in weno schemes for balance laws. Comput Fluids 2006;35(10):1074–92.
[4] Curran HJ, Gaffuri P, Pitz WJ, Westbrook CK. A comprehensive modeling study of n-heptane oxidation. Combust Flame 1998;114(1–2):149–77.
[5] Curran HJ, Gaffuri P, Pitz WJ, Westbrook CK. A comprehensive modeling study of isooctane oxidation. Combust Flame 2002;129(3):253–80.
[6] Davoudzadeh F, McDonald H, Thompson B. Accuracy evaluation of unsteady cfd numerical schemes by vortex preservation. Comput Fluids 1995;24(8):883–95.
[7] Deiterding R. A parallel adaptive method for simulating shock-induced combustion with detailed chemical kinetics in complex domains. Comput Struct 2009;87(11–12):769–83.

[8] Fedkiw RP, Merriman B, Osher S. High accuracy numerical methods for thermally perfect gas flows with chemistry. J Comput Phys 1997;132(2):175–90.
[9] Ferrer PJM, Buttay R, Lehnasch G, Mura A. A detailed verification procedure for compressible reactive multicomponent Navier–Stokes solvers. Comput Fluids 2014;89:88–110.
[10] Glaister P. An approximate linearised Riemann solver for the euler equations for real gases. J Comput Phys 1988;74(2):382–408.
[11] Hu X, Adams N, Iaccarino G. On the hllc Riemann solver for interface interaction in compressible multi-fluid flow. J Comput Phys 2009;228(17):6572–89.
[12] Jiang G-S, Shu C-W. Efficient implementation of weighted eno schemes. J Comput Phys 1996;126(1):202–28.
[13] Jiang G-S, Wu C-c. A high-order weno finite difference scheme for the equations of ideal magnetohydrodynamics. J Comput Phys 1999;150(2):561–94.
[14] Kim KH, Kim C, Rho O-H. Methods for the accurate computations of hypersonic flows: I. Ausmpw+ scheme. J Comput Phys 2001;174(1):38–80.
[15] Li C, Kailasanath K, Oran ES. Detonation structures behind oblique shocks. Phys Fluids 1994;6(4):1600–11.
[16] Liu Y, Liu Y-S, Wu D, Wang J-P. Structure of an oblique detonation wave induced by a wedge. Shock Waves 2016;26(2):161–8.
[17] McLachlan RI, Quispel GRW. Splitting methods. Acta Numerica 2002;11:341–434.
[18] Mott DR, Oran ES. Chemeq2: a solver for the stiff ordinary differential equations of chemical kinetics. Tech. Rep. Naval Research Lab Washington DC; 2001.
[19] Nonomura T, Terakado D, Abe Y, Fujii K. A new technique for freestream preservation of finite-difference weno on curvilinear grid. Comput Fluids 2015;107:242–55.
[20] Ó Conaire M, Curran HJ, Simmie JM, Pitz WJ, Westbrook CK. A comprehensive modeling study of hydrogen oxidation. Int J Chem Kinet 2004;36(11):603–22.
[21] Oran E, Young T, Boris J, Cohen A. Weak and strong ignition. i. numerical simulations of shock tube experiments. Combust Flame 1982;48:135–48.
[22] Roe PL. Approximate riemann solvers, parameter vectors, and difference schemes. J Comput Phys 1981;43(2):357–72.
[23] S Evans J, Charles J S Jr. Influence of chemical kinetics and unmixedness on burning in supersonic hydrogen flames 1980;18:188–93.
[24] Shu C-W. Essentially non-oscillatory and weighted essentially non-oscillatory schemes for hyperbolic conservation laws. In: Advanced numerical approximation of nonlinear hyperbolic equations. Springer; 1998. p. 325–432.
[25] Shu C-W. High order eno and weno schemes for computational fluid dynamics. In: High-order methods for computational physics. Springer; 1999. p. 439–582.
[26] Shuen J-S, Liou M-S, Van Leer B. Inviscid flux-splitting algorithms for real gases with non-equilibrium chemistry. J Comput Phys 1990;90(2):371–95.
[27] Smith GP, Golden DM, Frenklach M, Moriarty NW, Eiteneer B, Goldenberg M, et al. Gri 3.0 mechanism. Gas Research Institute, Des Plaines, IL, accessed Aug 1999;21:2017.
[28] Sod GA. A survey of several finite difference methods for systems of nonlinear hyperbolic conservation laws. J Comput Phys 1978;27(1):1–31.
[29] Teng H, Ng HD, Jiang Z. Initiation characteristics of wedge-induced oblique detonation waves in a stoichiometric hydrogen-air mixture. Proc Combust Inst 2017;36(2):2735–42.
[30] Westbrook C, Pitz W, Herbinet O, Silke E, Curran H. A Detailed Chemical Kinetic Reaction Mechanism for n-Alkane Hydrocarbons From n-Octane to n-Hexadecane. Tech. Rep. Lawrence Livermore National Laboratory (LLNL), Livermore, CA; 2007.
[31] Yee HC, Vinokur M, Djomehri MJ. Entropy splitting and numerical dissipation. J Comput Phys 2000;162(1):33–81.
[32] Ziegler JL, Deiterding R, Shepherd JE, Pullin DI. An adaptive high-order hybrid scheme for compressive, viscous flows with detailed chemistry. J Comput Phys 2011;230(20):7598–630.